

# River-width determination by the use of optical remote sensing missions

A research based on the determination of sub-pixel accurate river-widths using optical remote sensing

By

N. van der Vliet

Delft University of Technology



# River-width determination by the use of optical remote sensing missions

A research based on the determination of sub-pixel accurate river-widths using optical remote sensing

By

**N. van der Vliet**

in partial fulfillment of the requirements for the degree of

**Master of Science**

in Civil Engineering

at the Delft University of Technology,  
to be defended publicly on Tuesday July 9, 2019 at 4.00 PM.

Supervisor:	Dr. Ir. F. Boogaard	TAUW BV
	Ir. J. de Jager	TAUW BV
Thesis committee:	Dr. Ir. H.C. Winsemius (chair)	Delft University of technology
	Ir. W.M.J. Luxemburg	Delft University of technology
	Prof. Dr. Ir. M. Kok	Delft University of technology

A digital version of this thesis is available at <http://repository.tudelft.nl/>.

This project has received funding from the European Union's Horizon 2020 Research and Innovation Programme under grant agreement No 776866



## Preface

The report in front of you is the master thesis report “River-width determination by the use of optical remote sensing missions” of Nils van der Vliet. This thesis is written as part of the master program of the TU Delft. The research introduced me in the challenges that are paired with remote sensing techniques focussed on hydrological applications. I learned a lot about performing research in general and developed myself in the field of water classification via remote sensing during the time span of this thesis.

I would like to thank Floris Boogaard for giving me the opportunity to conduct my master thesis on the RECONNECT project in collaboration with TAUW BV. I would also like to thank Jan-Willem Knegt and Judith de Jager for including me within the RECONNECT project.

From the University of Technology Delft, I would like to thank my thesis committee, Willem Luxemburg, Hessel Winsemius and Matthijs Kok for their time and effort in providing me guidance and the meetings and discussions about my research. I learned a lot from the guidance of this committee.

Finally, I am thankful to the university and especially to the Watermanagement department, for providing a working space and the materials I needed to perform this research with success.

*N. van der Vliet  
Delft, July 2019*



River data on discharge and characteristics is essential for water management and water supply, as well as for flood prediction and flood control (Pan, Wang, and Xi 2016). In practice, many watersheds are ungauged due to high costs, inaccessibility and even due to political instability (Pan, Wang, and Xi 2016). For this reason, measuring remotely without the need of being physically present, for instance by remote sensing satellites, can be interesting for many applications. The large amount of satellite data can result in the ability to extend short observation series into larger series with satellite missions.

Discharge is one of the conditions in a river, which is relevant to have data on during regular periods but in particular during or after extreme events. This thesis focussed on an approach, by using remote sensing, to obtain data that can be used for further research to determine discharge. River-width is one of the current variables researched to be used as a substitute for river stage data. River stage is currently used to obtain estimations for river discharge via earlier obtained river stage-discharge relations, which can be transformed into river width-discharge relations.

The objective of this thesis was to develop a method to obtain sub-pixel accurate river-width estimations by remote sensing. The objective to estimate river-widths on sub-pixel base originates from the need of river-width estimations with higher accuracy than the freely available optical satellite resolutions of 10 to 20 metres. The study contains the improvement of the current water classification methods by including analyses for discriminating band combinations, to construct site-specific indices. This was noticed to be needed, due to the conventional indices, like the NDWI, performing differently with the presence of certain land types.

By having multiple indices based on uncorrelated satellite bands transformed into probability bands, it is possible to combine indices, via Bayes theorem. Based on the site-specific indices and index combinations, the aim is to develop relations between spectral information and water fractions of pixels that could lead to a more detailed river-width estimation by including sub-pixel information.

The resulting method was able to show discriminating abilities in satellite bands and band combinations, specifically for an area of interest, other than the conventional NDWI and MNDWI. With the use of river edge information, the spectral bands could be transformed into spatial water probability bands, indicating a probability for the present pixels to be water. The probability indices and index combinations showed to reduce a large part of the occurring misclassifications. With the use of ROC curves, to assess the classification performance of the indices and combination of indices, variation in misclassification of certain land types between days were observed for certain indices.

The probability bands, which are based on the river's edge value distribution, also seemed to be useful, especially for the pan-sharpened MNDWI and the Bayes 0-3 indices, to obtain the needed water fraction relations for sub-pixel base estimations. A comparison in river-width estimation of a conventional automated water classification method; Otsu's thresholding method and a Supervised training map classification method were made against the use of probability indices with sub-pixel water fraction relationships. It was found that the use of sub-pixel information resulted in a significant improvement of the accuracy for river-width estimations. For the first and second fieldwork day, the average river-width deviations of the pan-sharpened MNDWI and Bayes0-3 decreased, respectively, from 16 and 9 metres, to under 5 and 7 metre deviation by including the found water fraction relationships.



Preface .....	v
Abstract.....	vii
Contents .....	ix
List of abbreviations.....	xi
1.....	1
Introduction.....	1
1.1. Problem motivation.....	2
1.2. Problem statement .....	3
1.3. Research objective .....	4
1.4. Scope definition .....	4
1.5. Research question.....	5
1.6. Report outline .....	6
2.....	7
Theoretical background.....	7
2.1. Measuring techniques .....	7
2.1.1. GNSS.....	7
2.1.2. Aerial Drone equipped with a camera .....	7
2.1.3. ADCP.....	8
2.2. Remote sensing.....	8
2.2.1. Remote sensing satellite missions .....	8
2.2.2. Remote sensing pixels and Indices .....	11
2.2.3. Water classification by optical remote sensing.....	13
2.2.4. Errors introduced in spectral data from satellites .....	15
2.2.5. Google Earth Engine as a remote sensing analysis platform .....	16
3.....	17
Methodology .....	17
3.1. Study location .....	19
3.1.1. IJssel river basin.....	19
3.1.2. Study location southwest of Herxen, Netherlands.....	20
3.1.3. Ground truth data collection .....	22
3.1.3.1. Waterline contour.....	23
3.1.3.2. Bathymetry and discharge.....	23
3.1.3.3. Photogrammetry of the floodplains.....	24
3.2. Current cutting-edge method for water classification .....	25
3.3. Finding discriminating bands between water and land.....	25
3.4. Finding discriminating band combinations for custom normalized difference water indices .....	27
3.5. Image enhancements to improve water classification abilities.....	28
3.6. Combining normalized difference indices to improve classification .....	30
3.6.1. Obtaining index probabilities .....	30
3.6.2. Bayes theorem for combining index probabilities.....	31
3.7. Quality assessment of methods with in-situ measurements .....	32
3.7.1. ROC analysis.....	32
3.7.2. Water fraction pixel analysis.....	33
3.7.3. River width analysis.....	34
4.....	35
Results and discussion.....	35
4.1. Ground truth data collection .....	35
4.2. Current cutting-edge method for water classification .....	39
4.2.1. Otsu thresholding results.....	39
4.2.2. Supervised classification with the use of a training map.....	42
4.3. Discriminating bands between water and land.....	44
4.4. Discriminating band combinations for custom normalized difference water indices .....	47
4.5. Image enhancements to improve water classification abilities.....	51
4.6. Combined normalized difference indices to improve classification .....	54
4.6.1. Obtaining index probabilities .....	54
4.6.2. Bayes theorem for combining index probabilities.....	56

4.7.	Quality assessment of methods with in-situ measurements .....	57
4.7.1.	ROC analysis .....	57
4.7.1.1.	ROC analysis of the site-specific index values .....	57
4.7.1.2.	ROC analysis on the probability bands of the site-specific indices .....	59
4.7.1.3.	ROC analysis on the combined probability bands with Bayes theorem .....	60
4.7.2.	Water fraction pixel analysis .....	61
4.7.3.	River width analysis results .....	65
5.	.....	71
Conclusion	.....	71
6.	.....	73
Recommendations	.....	73
References	.....	74
Appendix	.....	77
	Water slope .....	77
	Probability bands visualized .....	79
	Water fraction relation images .....	86
	Probability-width curve .....	91
	Workability of the used scripts .....	92

## List of abbreviations

MSI	Multispectral Instrument	GPS	Global Positioning System	RMSE	Root Mean Squared Error
ADCP	Acoustic Doppler Current Profiler	IQR	Interquartile Range	ROC	Receiver Operating Characteristics
AOI	Area Of Interest	KDE	Kernel Density Estimation	RTK	Real-Time Kinematic
API	Application Programming Interface	L7	Landsat-7 satellite mission	S2	Sentinel-2 satellite mission
AUC	Area Under the Curve	L8	Landsat-8 satellite mission	S2A	Sentinel-2 satellite A
BOA	Bottom of the Atmosphere	MNDWI	Modified Normalized Difference Water Index	S2B	Sentinel-2 satellite B
BSS	Between Sum of Squares	NBS	Nature-Based-Solution	SNAP	Sentinel Application Platform
DGPS	Differential Global Position Satellite	$NDSI_{gr-sw}$	Normalized Difference Snow Index, from green and SWIR1	SWIR	Short Wave Infrared
ESA	European Space Agency	$NDSI_{rd-sw}$	Normalized Difference Snow Index, from red and SWIR1	TIRS	Thermal Infrared Sensor
ETM+	Enhanced Thematic Mapper	NDVI	Normalized Difference Vegetation Index	TNR	True Negative Rate
FNR	False Negative Rate	NDWI	Normalized Difference Water Index	TOA	Top of the Atmosphere
FPR	False Positive Rate	NIR	Near Infrared	TPR	True Positive Rate
GEE	Google Earth Engine	OLI	Operational Land Imager	UAV	Unmanned Aerial Vehicle
GIS	Geographical Information System	PDF	Probability Density Function		
GNSS	Global Navigation Satellite System	QGIS	Quantum Geographic Information System		



# 1.

## Introduction

Water is a necessity everywhere in the world. Some parts deal with droughts, some parts with floods and some even with both. Therefore, river data on discharge and characteristics is essential for water management and water supply as well as for flood prediction and flood control (Pan, Wang, and Xi 2016). River discharge can be measured directly with the use of gauging stations. But in practice, many watersheds are ungauged due to high costs, inaccessibility and even due to political instability (Pan, Wang, and Xi 2016). For this reason, measuring remotely, for instance by remote sensing satellites, can be interesting for many applications. The field of remote sensing is growing as the available technology is evolving rapidly. The growth in technology is causing the advantages, that remote sensing brings, to expand. One of the biggest advantages these days, is the possibility to access historical data. Most available satellites are providing data for at least several years. The large amount of satellite data can result in the ability to extend short observation series into larger series with satellite missions. Especially applicable if one wants to research a certain ungauged area. The second advantage is the ability to measure without being physically present. In cases of using historical data, this is of the essence, but also a useful aspect for remote project locations, which are difficult to reach. Discharge is one of the conditions in a river, which is relevant to have data on during regular periods but in particular important during or after extreme events whereby the discharge is significantly higher or even significantly lower than during normal periods.

The Department of Water management at the University of technology Delft is researching different methods of working towards river discharge determinations. Measuring remotely is one of the aspects of raising interest. Therefore, this thesis will focus on an approach, by using remote sensing, to obtain data that can be used in other researches for discharge determinations or at least preliminary discharge determinations. Formulas such as the Manning equation, to calculate uniform steady state flow in channels, need river dimensions like the area, wetted perimeter but also characteristics regarding roughness and channel slope. Normally, when the relation between river stage (water level) and discharge is known, the only parameter needed to obtain the discharge is the river stage. River stage is difficult to measure by satellites with a high overpass frequency. Hence, river widths instead of river stages will be determined with the use of optical-satellites. There are some difficulties regarding information from satellites, such as the pixel size also known as the resolution. The pixel size of the freely available optical satellite data is relatively large, resulting in less detailed results, which cause less accurate water classification results. This brought up the idea for this research. The proposed approach for this thesis on obtaining river width data will be achieved by assessing sub-pixel accurate river widths from optical remote sensing. The use of satellite missions to determine the river width will serve as a basis for further research to widen possibilities for the determination of river discharges with the help of remote sensing. When the cross-section of the river is known, a relation between the river stage and the river width can be made. This relation can be used together with a rating curve of a project location to obtain semi-historical data of the rivers discharges.

The paragraphs below describe the problem and the objectives that will be addressed in this research. Section 1.1 shows the problem motivation followed by the problem statement in section 1.2. The research objectives can be found in section 1.3. The scope definition in section 1.4 shows the boundaries of the project where the research questions follow in section 1.5. In the last section, section 1.6, is the report outline defined for this master thesis.

## 1.1. Problem motivation

This thesis is conducted in co-operation with TAUW BV (Tauw). Tauw is part of the European project RECONNECT, which focusses on Nature-Based-Solutions (NBS). The RECONNECT project aims to provide a European framework on NBS for hydro-meteorological risk reduction (RECONNECT Consortium 2018). The framework in the form of a platform will consist of data concerning project realizations but also on monitoring data of the involved projects. This data on already completed projects can be used as “best management practices”, for the planned NBS projects that will be realized within the five years’ time span of the RECONNECT project. Project “Stroomlijn IJssel”, which is part of the project “Room for the river” in the IJssel basin, is part of RECONNECT as demonstrating case in the Netherlands. Room for the river in the IJssel basin is an example of an NBS project focused on flood risk reduction.

The Room for the river project entails giving the river more space during high water periods. Instead of introducing more structures and/or building higher river banks and dikes, the goal is to give the river more capacity and to remove obstructions in the rivers flow path. This is done by enlarging and or deepen the flood plains, lowering of groynes, lowering of summer bed level, lowering of summer dikes and building bypasses. These examples are visualized in Figure 1. Implementing these measures will mean more room for the river, capacity, to flow during higher discharge periods, resulting in lower flood risks. The aim of the “Room for the river” project is to implement measures that are effective for reducing flood risk by giving more space to the river instead of constructing more and higher dikes.

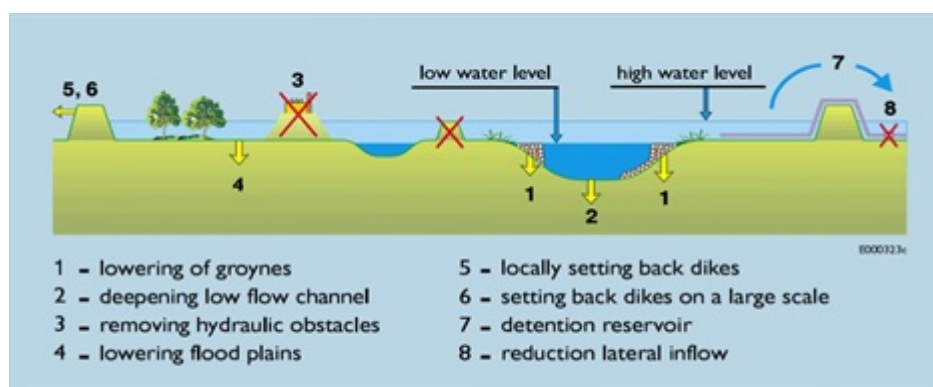


Figure 1 Measures Room for the River, (Silva, Klijn, and Dijkman 2001)

The focus of project “Stroomlijn IJssel”, which is part of Room for the River, is on less friction and obstructions on the floodplain during high water levels. This is done by identifying and removing these obstructions in the flow paths of the river. Obstructions in the rivers flow path can cause a rise in water level during high discharge periods in the river and thereby causing a higher level of risk for flooding (Makaske et al. 2011). Tauw is working on innovative methods on maintaining the flood plains by working with a platform to analyse remote sensing data and translates this into a list with potential obstructing vegetation. An example of the possible results is a georeferenced overview of trees and bushes, that need to be removed in order to meet the demands for flood risk reduction.

The river IJssel being a demonstrating project case for the RECONNECT project means that data of the river, like the river’s characteristics, need to be obtained and delivered to the RECONNECT demonstrating platform. The monitoring data will be visualized and made accessible in this platform for the new NBS projects connected to RECONNECT. The data on the NBS project vary from quantitative river data to ecological information about the flora and fauna. This kind of data can come from continuous measurements, fieldwork missions but also from remote sensing data. Therefore, already measured data need to be retrieved, but also new ways of measuring can be considered to explore the possible options for obtaining data from the river.

## 1.2. Problem statement

The larger Dutch rivers contain many manmade interventions like groins and sheet piles to maintain the shape of the river, in other words, to prevent the river from meandering. Now that the river IJssel has given more “room” to flow, in the “room for the river” project, it means that the base situation of the river has been changed. The aim is to monitor the river after intervention so, that one can understand the effectiveness of the interventions. To monitor the changed situation, continuous measuring probes can be installed, fieldwork mission can be conducted, or use of alternative innovative methods like the use of remote sensing satellites can be applied. As the “Stroomlijn IJssel” is a demonstrating case it is required to provide data on water quality, quantity, and characteristics of the river. In the larger rivers of the Netherlands, Rijkswaterstaat is the Dutch organization, which is responsible for maintaining and managing the major rivers in the Netherlands. Rijkswaterstaat is already monitoring river parameters in the IJssel, like water level (with respect to NAP), wave heights and a number of water quality parameters. Besides conventional measuring methods, they are now also working on remote sensing tools to visualize land classifications, NDVI maps, and to map flow paths by using algorithms within their “Vegetatiemonitor” tool. This already is a useful tool to compare a land classification side by side with the land register. Rijkswaterstaat has continuous water stage monitoring in the IJssel near Olst, which is used to obtain discharge data by using a constructed rating curve.

There are several methods which can be chosen to do discharge measurements. A velocity sensor can be used manually at several widths and depths of a cross section to construct a profile of velocities together with an estimation of the underwater profile at a rough scale. This type of measurements uses the velocity-area method, which can be a time and labour consuming task, especially when the river of interest is large. A velocity sensor is relatively cheap, which makes it for small streams useful and quick to use but becomes labour intensive when the stream is becoming wider and deeper.

An ADCP (Acoustic Doppler Current Profiler) is an easier and more automated method than a velocity sensor. This device creates a cross-section profile divided in bins of certain sizes, of which all have a velocity measurement. With the combination of the small subsections (bins), the velocities in each bin, a discharge can be computed. This is an example of the velocity-area method made automated (Pan, Wang, and Xi 2016). The price of discharge sensors like ADCP's is, on the other hand, high, varying around 20.000 euros up to almost 90.000 euros (Combe 2014; H. C. Lee et al. 2011). The downside of velocity sensors and ADCP applications in the field is that these measurements are single measurements in time and it is not possible/feasible in terms of labour to use them as continuous measurements.

Gauging stations, which consists of either continuous river stage measurements or of flow measurements, are methods to obtain continuous measurements through time. Most of the time, gauging stations measure river stage and convert this with stage-discharge rating curves into discharge data. Constructing a stage-discharge rating curve is time-consuming. With varying levels of maintenance and changing river morphology over time, the rating curves will change, and particularly, the inundation pattern of the flood plain will change. Therefore, a periodic check and an update of the rating curve is needed. The periodic check is one of the reasons why the maintenance of a gauging station is about 18.000 euro a year, which is almost equal to the investment costs (Fekete and Vörösmarty 2007; Pan, Wang, and Xi 2016).

Remote sensing could step in at the need for cheaper continuous measurements. Continuous measurements in terms of remote sensing mean by the limits of the overpass time of the used satellite missions. Compromised images with clouds, for example, results in another constraining factor for the temporal resolution of measurements. Remote sensing satellites also face restrictions in the resolution of pixels. Each satellite has its own resolution, which can vary for different wavelength domains. The coarse resolution of satellites can cause a large error in land use classification. This error in land use classification can occur when water and land are located in the same pixel, which makes this pixel hard to classify as either one of them. During classification, it is not known what the percentage of water and the percentage of land is on the edge of a transition between water and land. This means that pixels on

the river banks will be classified as either land or water and can result in a possible large error when this is used for river width estimation. If the classification of water by remote sensing would be used to determine river-widths, the error in this river-width will then depend on the quality of water classification and on the pixel resolution. When using river-width data as input for river discharge estimation, the error in river-width will introduce an error in the discharge as well.

### **1.3. Research objective**

Remotely being able to measure data of a river is a powerful ability. Measuring remotely in combination with open-source satellite data makes it cheap and accessible to many people. The objective of this thesis is to find and define a method to optimally assess sub-pixel accurate river-widths from open-source optical remote sensing. To research the possibilities of the objective, analysing the current state of the art techniques for water classifications is needed. This is followed by investigating and searching for a method on how to find the presence of discriminating satellite bands and combinations of satellite bands. The search for a method to find discriminating bands and combinations need to be conducted to obtain bands that are site-specific discriminating and therefore increasing the classification performance for that area. The ability to provide a sub-pixel based river-width estimation is preferred over the conventional method based on the current pixel resolution of the open-source Sentinel-2 and Landsat 7/8 satellite missions. A method is researched in this thesis to use probabilities of a pixel being water by river-edge sampling to use as distributions functions for different normalized difference indices. The advantage of using probabilities for pixel classification is the ability to combine multiple water indices. Accurate fieldwork on the river outline is needed for quality comparison and will, therefore, be performed during this thesis. The idea behind river-width determination from outer space is derived from the desire to remotely obtain river-widths detailed enough to be used as input for discharge determination methods.

### **1.4. Scope definition**

To limit the scope of the study, this research will be focused on measuring river-widths with the use of optical remote sensing. Techniques on improving this process will be researched by finding methods to show relationships in spectral bands and band combinations (indices) to improve water classification. Besides improving classification, researching land and water sub-pixel classification will also be part of this thesis. The target of the methodologies of this thesis is to obtain a workflow for site-specific river-width estimations that uses local information. This means that it is not a general method that can be used uniformly to map water classification of the entire world in the same way with the same combinations. The study location where the method will be tested is on the river IJssel. The research is mainly focused on what can be done to make the river-width estimation more accurate compared to the current state of the art classification methods. Actual ground truth is an important aspect of this study as it will be used to compare and to identify the error in the found method of this research. To obtain ground truth data, fieldwork needed to be conducted during this thesis.

## 1.5. *Research question*

The research question and sub-questions below have been formulated based on the research objective and scope definition. This thesis is performed by answering the following research question:

How to optimally assess sub-pixel accurate river widths from optical remote sensing?

To answer the main research question the following sub research questions will be investigated.

- a) What is the current cutting-edge water classification method for land and water?
- b) How can bands be found that discriminate land from water?
- c) How can combinations of bands be found that discriminate land from water?
- d) What image enhancements can be done to improve the classification to obtain a more precise river-width?
- e) Do combinations of locally chosen normalized indices improve the water classification compared to the conventional classification indices like MNDWI and NDWI?

## 1.6. Report outline

The report outline will be described below. The main topic of this thesis will be focused on the relationship between land and water characteristics in remotely sensed pixels and how pixels containing both can be distinguished by using fieldwork as ground truth data. The introduction to this topic is discussed in chapter 1, as well as the motivation, objective, scope and research questions.

Chapter 2 provides theoretical background information to understand the used methods in this thesis. This chapter is divided into a [Measuring techniques](#) part and a [Remote sensing](#) part. The measuring techniques section explains the different fieldwork equipment that is used. The Remote sensing section focusses on the different satellite missions used in this thesis, as well as more in-depth in the different information satellites provide and some examples of the applications.

Chapter 3 focusses on the methods of this thesis to fulfil the objectives and to answer the research questions. This chapter is written by following a workflow for the new water classification method. Therefore, the used methods are presented in a logical order to work through the steps to obtain the results of this new method. The first two and the last step of the workflow were added for verification of the results. This chapter starts with ground truth data collection at the study location for verification purposes. This is followed by collecting classification results of a conventional method for classification for comparison purposes. Site-specific discriminating bands will be searched by analysing historical data for the area of interest as preparation for the next research section, which focusses on discriminating band combinations. The output of the discriminating combinations is turned into normalized difference indices. These indices will be used to obtain probabilities of pixels for being water for each index. This is followed by obtaining probabilities for pixels being water for combinations of indices. Finally, the ground truth, two conventional classification methods, and the new method are compared.

Chapter 4 shows the results and the discussion of this thesis, which is discussed in the same order as the methods chapter. Results will be visually viewed, compared and discussed in this chapter.

Chapter 5 shows the conclusion of this thesis regarding the newly developed method for classification.

Chapter 6 provides recommendations for further research on the new method to obtain river-widths.

# 2.

## Theoretical background

In this chapter, the needed background information is given to provide a general understanding of the conducted research. This chapter is divided into several sections. The first section is [Measuring techniques](#), where the different measuring equipment, that is used during fieldwork, is described. The second section is [Remote sensing](#) and gives background information about the use and the information provided by spectral satellites. The used satellites are explained as well as background information on the used analysis software of the remotely sensed data.

### 2.1. *Measuring techniques*

There are multiple ways to measure the river width. A few possible options for this thesis are discussed below, like the use of drones, High-end RTK GPS systems, and ADCP devices. These measuring techniques can be used to validate the results of the research on the mixed pixel problem obtained by remote sensing satellites. The final objective is to obtain a more precise river width determination with the use of remote sensing, without having to conduct fieldwork. Therefore, ground truth data collection to validate this new method is needed.

#### 2.1.1. GNSS

A modern and easy to use device is a GNSS device, which stands for “Global Navigation Satellite System”. This is a high-end GPS device that uses DGPS (Differential Global Position Satellite) with RTK stations (Real Time Kinematic) connected to each other via the internet. The DGPS can measure up to 20-centimetre accuracy, but in combination with RTK stations via an internet connection, the accuracy is brought down to millimetres. The Leica GS14 GNSS, which is used in this research, can measure with an accuracy of 8-millimetres in horizontal direction and 15 millimetres in vertical direction (Leica n.d.). With the use of this device, the waterline can be mapped by taking point measurements in the longitudinal direction of the river for a certain stretch. The GNSS receiver can be attached to a rod for easy and stable measurements. Besides the waterline, ground control points can also be mapped to calibrate and improve photogrammetry maps (explained in section 2.1.2).

#### 2.1.2. Aerial Drone equipped with a camera

Drones can be deployed to measure geometries of areas with the use of photogrammetry software. For making this measuring technique accurate, reference or ground control points need to be surveyed with a precise location in the x, y, and z-direction. After this, photogrammetry software can be applied to measure the geometry of the non-flooded floodplains and the width of the current river. A high-end GNSS, precise GPS, can help to obtain the needed data for the ground control points. When study areas need to be measured more often it is possible to leave the reference points in place, which means these points need to be measured only once. Once the reference points are known and marked by chessboard-like plates, a drone can fly a certain path while taking photos of the ground with a certain overlap in each photo. These photos, together with the reference points can be used within the photogrammetry software to create a digital surface model (DSM). The downside of this method is the difficulty of mapping water correctly, especially due to the fact that the water is flowing, which means the software has trouble to find similar areas or connection points on the water without land reference

in the picture. The banks including a portion of the water will be detected properly, especially in the orthophoto made from the drone images. The surface areas can be mapped with high accuracy, approximately 1-3 times the accuracy of the reference points (Pix4D n.d.).

### 2.1.3. ADCP

An ADCP, what stands for Acoustic Doppler Current Profiler, measures, with the use of acoustics, a velocity profile over the width and the depth of the river. The rivers profile and velocities at different depths and widths can be used with the area-velocity method to calculate the discharge (Pan, Wang, and Xi 2016). Unfortunately, an ADCP cannot measure the flow velocity over the entire profile. Near the banks, the top and bottom layer cannot be measured. At these locations, interpolation is performed to obtain estimated values in these areas as well.

## 2.2. Remote sensing

Remote sensing via satellites can be used for various applications. A few examples of applications are tracking deforestation, mapping land uses and obtaining information on irrigation fields. Radar and optical remote sensing are two different types of measuring techniques. Radar remote sensing has the advantage that it can penetrate clouds and is thereby not affected by weather conditions as optical remote sensing is. The biggest difference between the two remote sensing types lays in the electromagnetic spectrum. Radar measures with a wavelength in the order of 10-centimetres, also known as microwaves (Richards 2015). Optical satellites measure with a wavelength in the order of 400 to 2200 nanometres, known as the field of the visible and infrared domain of light. Optical remote sensing is used for this research because of the different properties of land and water in the visible-near infrared domain. The two considered satellite missions are explained first, followed by a section about what optical satellites actually measure. Then conventional water classification methods are. Thereafter, errors that can be present in the optical satellite data are described, followed by information about the used platform to process and analyse the data.

### 2.2.1. Remote sensing satellite missions

In this thesis, the use of Landsat-7/8 and Sentinel-2 are investigated for sub-pixel accurate river-width estimations. Satellites capture images of the earth containing various types of information. Landsat 8 and Sentinel-2 are two satellite missions, which provide their sensed images free of charge. This is what makes these satellites interesting for many applications. Especially, considering the small pixel size (resolution) of most bands is around 30 meters for Landsat 8 and varying from 10 to 20 meters for Sentinel-2 depending on the band. The different bands resemble the reflection of light in a certain domain (bandwidth). These bandwidths are measured in nanometres and are called wavelengths. Section [Sentinel-2](#) below is the adapted version of the original text that can be found in my internship report (Vliet van der 2018).

#### 2.2.1.1. Sentinel-2

The Sentinel-2 mission contains two polar orbital satellites. Both satellites S2A and S2B are following the same path but with a phase shift of 180° to increase the revisit time. The two satellites have a multispectral instrument (MSI) using a push-broom sensor. This sensor type measures rows in a sweeping motion, perpendicular to its movement, and uses the movement of the satellites to get in position for the next sweep. The MSI measures ten bands in the visible-near infrared domain and three in the short wave infrared domain. There are three different spatial resolution bands given by the Sentinel-2 mission. The different resolution bands are at 10-meter, 20-meter and at 60-meter resolution (ESA n.d.). Details of the Sentinel-2 bands for S2A and S2B are given in Table 1. It can be seen that

there are some minor differences in central wavelength and bandwidth between S2A and S2B. The bandwidth indicates what the range of wavelength domain is, in which reflected light is captured and given for this band. For example band 3 of S2A is measuring reflected light from 537.5 nm to 582.5 nm (bandwidth of 45 nm, with a central wavelength of 560 nm). This domain of wavelengths is also called the green colour domain.

Table 1 Sentinel-2 spatial and spectral details (ESA n.d.)

Band number	Sentinel-2A		Sentinel-2B		Resolution (m)
	Central wavelength (nm)	Bandwidth (nm)	Central wavelength (nm)	Bandwidth (nm)	
Band 1 – Coastal aerosol	442.7	21	442.2	21	60
Band 2 – Blue	492.4	66	492.1	66	10
Band 3 – Green	559.8	36	559.0	36	10
Band 4 – Red	664.6	31	664.9	31	10
Band 5 – Vegetation red edge	704.1	15	703.8	16	20
Band 6 – Vegetation red edge	740.5	15	739.1	15	20
Band 7 – Vegetation red edge	782.8	20	779.7	20	20
Band 8 – NIR	832.8	106	832.9	106	10
Band 8A – Narrow NIR	864.7	21	864.0	22	20
Band 9 – Water vapour	945.1	20	943.2	21	60
Band 10 – SWIR – Cirrus	1373.5	31	1376.9	30	60
Band 11 – SWIR	1613.7	91	1610.4	94	20
Band 12 – SWIR	2202.4	175	2185.7	185	20

### 2.2.1.2. Landsat-7/8

Landsat 7 satellite mission was launched in 1999 and is equipped with the Enhanced Thematic Mapper (ETM+) sensor. With this satellite mission, the entire earth is covered every 16 days. The images of Landsat 7 and 8 are as well as Sentinel-2 available free-of-charge. The ETM+ sensor measures eight spectral bands, of which six bands at 30-meter resolution, one panchromatic band at 15-meter resolution and one thermal band at 60-meter resolution.

Landsat 8 satellite mission is currently the newest mission of the Sentinel range and is launched in 2013. Landsat 8 carries two sensors “The Operational Land Imager” (OLI) and “The Thermal Infrared Sensor” (TIRS) (United States Geological Survey (USGS) 2018). Landsat 8 covers, like Landsat 7, the entire earth with these two push-broom sensors in 16 days. The OLI measures nine bands and the TIRS measures two bands. The spatial resolution of the OLI measured bands are 30 meters, except for the panchromatic band, which is at 15 meters resolution. The TIRS measures its two bands at 100-meter resolution, which resampled to 30 m resolution. The spectral and spatial details can be found in Table 2.

Table 2 Landsat 7 and 8 spatial and spectral details (United States Geological Survey (USGS) n.d.)

Band number	Landsat 7			Band number	Landsat 8		
	Central wavelength (nm)	Bandwidth (nm)	Resolution (m)		Central wavelength (nm)	Bandwidth (nm)	Resolution (m)
n/a	n/a	n/a	n/a	Band 1 – Coastal aerosol	443	16	30
Band 1 – Blue	485	70	30	Band 2 – Blue	482	60	30
Band 2 – Green	560	80	30	Band 3 – Green	561.5	57	30
Band 3 – Red	660	60	30	Band 4 – Red	654.5	37	30
Band 4 – Near Infrared	835	130	30	Band 5 – Near Infrared	865	28	30
Band 5 – Shortwave Infrared (SWIR) 1	1650	200	30	Band 6 – Shortwave Infrared (SWIR) 1	1608.5	85	30
Band 7 – Shortwave Infrared (SWIR) 2	2212.5	245	30	Band 7 – Shortwave Infrared (SWIR) 2	2200.5	187	30
Band 8 – Panchromatic	710	380	15	Band 8 – Panchromatic	589.5	173	15
n/a	n/a	n/a	n/a	Band 9 – Cirrus	1373.5	21	30
Band 6 – Thermal Infrared	11450	2100	60 (resampled to 30 m)	Band 10 – Thermal Infrared (TIRS) 1	10895	590	100 (resampled to 30 m)
n/a	n/a	n/a	n/a	Band 11 – Thermal Infrared (TIRS) 2	12005	1010	100 (resampled to 30 m)

## 2.2.2. Remote sensing pixels and Indices

A regular photo camera captures the combination of the Red, Green and Blue colour domain together in one image, also known as an RGB image. The RGB domain is in the visible domain and represents the way humans see light. Most multispectral satellites capture also beyond the visible spectrum in more different wavelength bands and thereby creating different possibilities with this data. Spectral satellites measure the reflected radiance of the earth via different bands and giving this information in terms of wavelength. Each wavelength, or better said, each interval of wavelengths stands for a colour domain. This is why for example band 2 of Sentinel-2, as seen in Table 1, stands for the blue domain.

Images taken by spectral satellites have the same principle as regular photo camera's. They consist of a collection of pixels forming the image, whereby these pixels have a certain size, or in other words, a certain spatial resolution. The spatial resolution determines the size of the pixel and therefore the size of detail. The size of detail can be determined spatially, thus in pixel size but also spectral in domain size. Domain size, which is the bandwidth of each band. The smaller the bandwidth, the more detailed information each band gives. With spectral satellites, there is a trade-off between high spatial resolution and high spectral resolution. A higher resolution means settling for a lower spectral resolution (Brodu 2017). The sensors need to capture enough light to give an accurate representation. This is the same as for photo cameras at night where there are two options available; 1) long exposure time, but movement makes the images blurry and 2) shorter exposure time, which means capture the image with not enough light resulting in a lot of noise in the image (Brodu 2017). Therefore, the trade-off between spatial and spectral resolution is based on the fact that high-resolution bands are taken over a wider range of wavelengths to be able to capture more light. The other option, which is the opposite of this trade-off, is by using a bigger pixel size, e.g. 20 m instead of 10 m, to capture four times as much light.

The pixel values measured by satellites contain average reflection values of that pixel measured in different groups of wavelengths, as explained above. An example of how this works can be explained with a red object. This red object will be sensed by the satellite by capturing a higher reflection in the red domain and low reflection of the green and blue domain due to the high absorption of the domains green and blue.

The different bands with each its own wavelength and bandwidth can be used in various ways for visualizing but as well as for calculations and classifications. A way to make classifications is to use the distinctive reflectance pattern of certain land uses to discriminate it from other land uses.

This can be done for example by combining different bands in a normalized difference index, like NDVI, the normalized difference vegetation index. This index is used to detect or measure vegetation by the property chlorophyll, where green and near infrared is reflected and blue and red is absorbed (Gis geography 2018). When vegetation needs to be monitored, the NDVI can be used to get an indication index of the amount of reflectiveness of NIR versus the absorption of red. The NDVI varies from -1 to 1, where 1 shows high chances of dense green leaves and -1 shows a high chance of water.

The NDVI is calculated by the following formula (Gis geography 2018):

$$NDVI = \frac{\rho_{NIR} - \rho_{red}}{\rho_{NIR} + \rho_{red}}, \quad (1)$$

Where  $\rho$  stands for the satellite band used.

The example above regarding NDVI shows how the reflectance pattern of vegetation (chlorophyll) is differentiated from other land uses by the formula. This pattern can be visually seen in Figure 2, where vegetation, indicated by the green line, has a drop at the red domain and a peak at near-infrared (on the right of the red spectrum). Water and dry bare soil have a different pattern, which means vegetation can be discriminated from the other two land uses via NDVI.

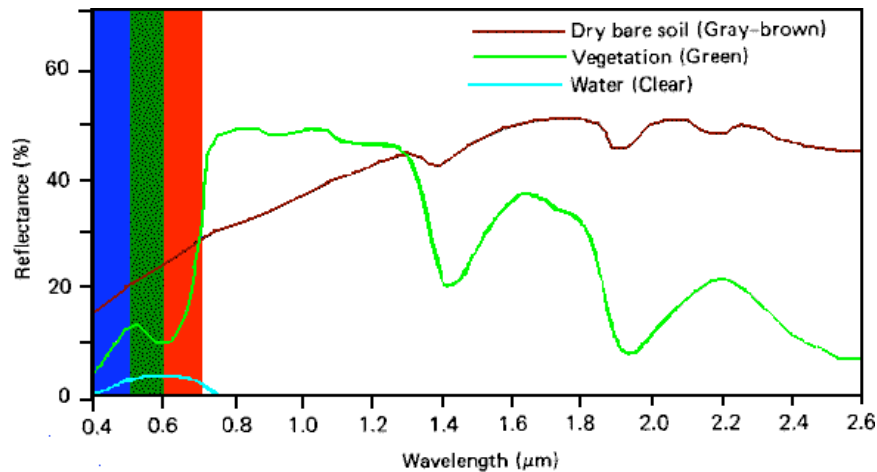


Figure 2 Hyperspectral signal of water, soil and green vegetation (Geomatica 2013)

The patterns shown in Figure 2 are depicted by a hyperspectral sensor where, in practice, spectral satellites use multi-spectral sensors. Meaning that the level of detail from satellites will be more in the range of patterns seen in Figure 3. With less detailed information, it is still possible to discriminate land uses. For NDVI, band 2 and band 4 are used in Figure 3. This can be motivated by the difference in patterns where the reflectance of vegetation increases from band 2 to band 4 and the other land uses decrease from band 2 to band 4.

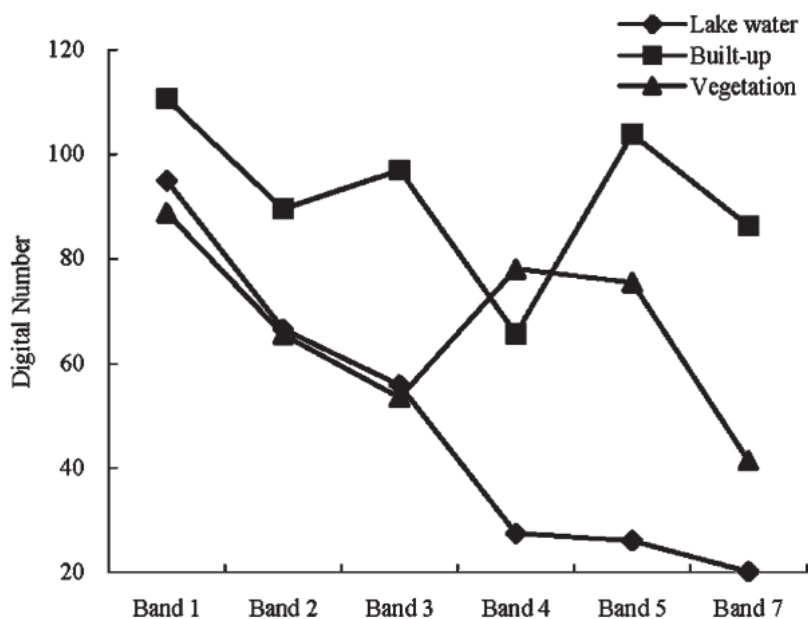


Figure 3 Reflectance pattern Landsat 5 for Lake water, Built-up, and vegetation (H. Xu 2006a)

More water-related indices are the normalized difference water index (NDWI) and the modified NDWI also known as MNDWI. These two indices make use of the same concept as for NDVI, but here, specifically for water discrimination.

The NDWI is calculated with the TOA (top of the atmosphere) green and NIR bands (McFeeters 1996). By using the NDWI, water typically shows a positive number, where vegetation or soil show zero or negative values for NDWI.

The formula for NDWI can be written as:

$$NDWI = \frac{\rho_{green} - \rho_{NIR}}{\rho_{green} + \rho_{NIR}} \quad (2)$$

The modified NDWI is designed because NDWI of water has a similar pattern as Built-up land classes. The green and NIR bands are band 2 and 4 respectively in Figure 3. In this figure, it can be seen that water and the built-up land both decrease from the green band to the NIR band in reflectance value. This results in a similar pattern and therefore confusion of water classification over areas with water and built-up land. The MNDWI is also using the green band but instead of the NIR band, it makes use of short wave infrared (SWIR1) (H. Xu 2006a). Water bodies generally absorb more in the SWIR1 domain than in the NIR domain, therefore resulting in higher MNDWI values than NDWI for water bodies. SWIR1 is band 5 for Landsat 5 and this difference between water and built-up land can clearly be seen in Figure 3, where the SWIR1 band is higher, instead of lower like the NIR band, than the green band for built-up land resulting in a discrimination capacity between the two types. The formula for MNDWI can be written as:

$$MNDWI = \frac{\rho_{green} - \rho_{SWIR1}}{\rho_{green} + \rho_{SWIR1}} \quad (3)$$

Literature shows that snow and water look like each other in the green and SWIR1 bands. When looked at the NDSI it can be seen that it is identical to the MNDWI, therefore some caution is needed when snow is occurring. The in literature used index for snow mapping is the NDSI (Huang et al. 2018):

$$NDSI = \frac{\rho_{green} - \rho_{SWIR1}}{\rho_{green} + \rho_{SWIR1}} \quad (4)$$

It can be noted that different land uses contain different reflectance patterns due to their properties. Sometimes some land uses look like each other in certain combinations for indices. Besides land uses with a similar reflectance pattern, it can also happen that two land uses are located in one pixel. This happens if a pixel is partly land and partly water, it will contain a combined value describing them both in one pixel. Therefore, water pixels containing partly land will give a different value for the reflectance than a complete water pixel. These water/land mixed pixels occur near the banks of a channel but can also be found on partly flooded floodplains.

### 2.2.3. Water classification by optical remote sensing

Water can be classified via different methods. The classification types can be divided into two main types, supervised classification, and unsupervised classification. Supervised classification is applied when learning patterns or spectral patterns are used to identify pixels into certain classes. One of the methods for this is using a training map, where one locates polygons of, for example, water bodies and vegetation separately to create a database of spectral patterns of each class. The combination of spectral patterns belonging to the two classes is used to assign a certain class to the pixels based on the spectral pattern of each individual pixel. Overlap of patterns between classes can create certain confusion in classification and thereby possible misclassifications. Pixels containing different classes can also create confusion for the classification algorithm. When one knows that, for example, water always has a high MDNWI and land has a low MNDWI value, a threshold value can be set to classify pixels into the classes. This is also a form of supervised classification (Richards and Jia 2013).

An example of unsupervised classification is by using the Otsu method. The algorithm of the Otsu method makes use of the assumption that the data has a bimodal distribution. The Otsu algorithm segments the data into two classes by finding a single threshold. Otsu makes use of maximizing the inter-class variance, which means maximizing the variance between two classes (Otsu 1979). The inter-class variance is given as:

$$Var_{inter-class} = \frac{BSS}{p}, \quad (5)$$

where BSS is the Between Sum of Squares. There is a bimodal assumption, so p is set to 2. The Otsu algorithm finds a threshold where the BSS is maximal. This means the highest inter-class variance and is given by:

$$BSS = \sum_{k=1}^p (\bar{\mu}_k - \bar{\mu})^2, \quad (6)$$

where  $\bar{\mu}_k$  is the mean value of the data in class k for a certain threshold, whereas  $\bar{\mu}$  is the mean value of all data.

With this method, an automated threshold can be set, specified separately for each satellite image by maximizing the inter-class variance. Therefore, it is best to select an area where both classes are roughly equal in size to avoid under-classification of one of the two classes (X. Xu et al. 2011). To improve the calculation time this is done in Google Earth Engine by putting all pixel values of the selected area in a histogram where the bins are represented as the thresholds. By using the histogram bins as thresholds, the calculation can be done by passing the data once. The mean is calculated from the data slice of the 0<sup>th</sup> bin till the i<sup>th</sup> bin. This is repeated from i ranging from 0 to the last bin. The mean times the threshold represents the area under the histogram. The area under the histogram stays equal during this process, therefore, the next formula can be used to simultaneously calculate the mean of the second class:

$$A = (\mu_{0,i} * th_i + \mu_{1,i} * (th_n - th_i)), \quad (7)$$

Where A represents the AUC,  $\mu_{0,i}$  represent the mean value of one class at the i<sup>th</sup> location and  $\mu_{1,i}$  the second class.  $th_i$  represents the threshold at the i<sup>th</sup> location and  $th_n$  the last threshold in the range of the histogram.

All mean values of both classes for every i<sup>th</sup> location will be put in an array and used in the formula for BSS. The threshold corresponding to the highest BSS is according to the Otsu algorithm the optimal threshold.

This type of thresholding can be applied to a single band but also to water indices and works best when a discriminating ability is found in the used band or index. After obtaining the automated threshold by Otsu, it can be used to transform the data into, for example, a water class and a land class.

## 2.2.4. Errors introduced in spectral data from satellites

Along with satellites, in this case specifically spectral satellites, a few errors are introduced in the measured values. One of those errors can be caused by the adjacency effect. Pixels can be effected by the influence of reflectance of adjacent pixels. From research, it seems that target pixels, which are darker than the background, become brighter (Ma Jianwen et al. 2006) but it also seems to be the case the other way around. Target pixels, which are brighter than the background, become darker. This effect plays a role within high spectral resolutions and starts playing a role with resolutions higher than a 1000 meter (Ma Jianwen et al. 2006). The phenomena of the adjacent effect are visualized in Figure 4.

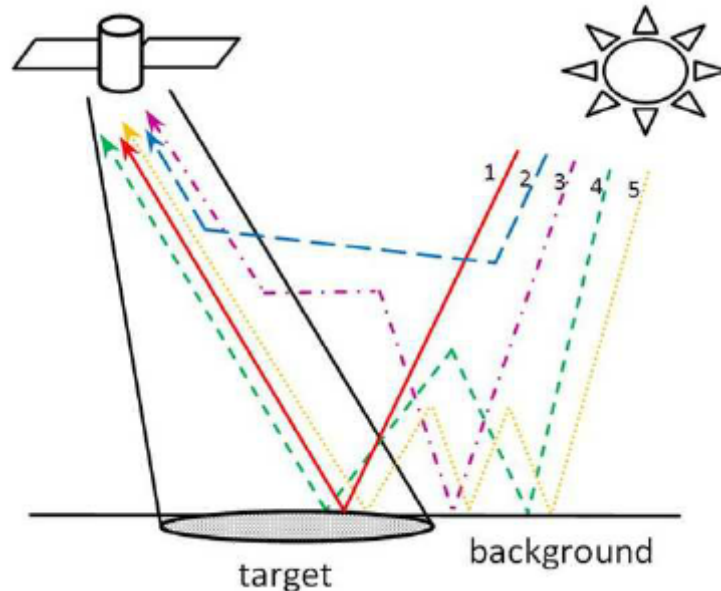


Figure 4 Adjacency effect, (Burazerović et al. 2013)

The introduction of hazy clouds or shadows of clouds on a measuring day can also introduce variations in sensing reflections from the ground. Clouds are a medium between the sensor and the ground and reflect already a part of the light, resulting in non-representative data of the area (Wang et al. 1999). Thick clouds even block the ground completely, resulting in an image that cannot be used as input data for water detection.

Images taken by the satellites are processed into accurate georeferenced images, which are available in 100km tiles for Sentinel-2 (esa, 2018) and approximately 170km tiles for Landsat 8 (United States Geological Survey (USGS) n.d.).

In the period this graduation was conducted, satellite 2a and 2b pass the research area in the IJssel near Zwolle every 2 to 3 days. This is due to the two orbital satellites following each other.

The performed atmospheric corrections on the images from ESA (organization of the Sentinel missions) on Sentinel-2 are focused on land (ESA n.d.) and are not originally designed like Sentinel-3 (300m resolution pixels) for water quality monitoring. Also, USGS (organization of the Landsat missions) claims that their Atmospheric Correction (AC) algorithms are not ideal for water bodies. Radiance levels leaving water bodies are fundamentally low compared to non-water bodies, which make the algorithm to obtain surface reflectance not suitable for water analysis (United States Geological Survey (USGS) n.d.). Therefore, TOA (Top of the Atmosphere) is used instead of BOA/SR (Bottom of the Atmosphere/Surface reflectance) images. TOA is preferred over raw digital data, one of the reasons for this is the correction for the varying distance between the earth and the sun during different acquisition data (Li et al. 2013).

### 2.2.5. Google Earth Engine as a remote sensing analysis platform

The images taken by satellite missions need to be processed. To work with the sensed data from satellite missions there is a need for process and analysis platforms/software. There are various well-known programs available like the GIS platforms (geographical information systems). Examples of GIS platforms are free of charge QGIS or the extended but paid version ArcGIS. The ESA (European Space Agency), who own the Sentinel satellite missions, also has its own GIS software called SNAP, which can specifically be used for sentinel data (ESA n.d.). These platforms are easy to use when processing small amounts of data.

Most of the GIS platforms work locally on your computer, whereby images need to be downloaded and processed on your computer. This process can be storage-space and time-consuming. The processing speed is then connected to the performance of your computer. A solution to overcome this problem is to use GIS-like platforms that are web-based. Google Earth Engine (GEE) is one of these web-based platforms.

GEE contains big servers with several petabytes of satellite imagery available with high-performance computation services (Gorelick et al. 2017). Users can import these imageries to make calculations on for example planetary scale or on time series to visualize deforestation in a region. The GEE service and computational power can be used in two ways. This can be either via an API for JavaScript or via an API for Python. The API (Application Programming Interface) can be seen as a toolset for interaction and communication between software programs. GEE implemented an online development environment that makes use of the JavaScript API environment. The online tool is where you send JavaScript-based code with commands and tasks to the GEE server, the server calculates the task on their server and then returns the output.

All free to access satellite data is already on the GEE servers and data that is not there can be uploaded and be used in your project in the same way. The processing time is a lot lower due to the access of high-performance parallel resources at the side of Google, the speed does depend on the number of available servers, which varies by the number of users (Gorelick et al. 2017). Using a web-based platform like GEE allows you to quickly check small tasks to explore usability. Due to the high-performance services from Google, the GEE platform is also highly useable for larger computations. GEE makes it possible for everyone with access to the internet to perform difficult and demanding tasks, without the limitations of their personal computer storage space or computer performance. There is a computational time-out warning possible when computing large calculations, though this only occurs when one wants to visualize the data immediately. A way to gain more time on the server is to export the data instead of printing or showing this on the map, hence this gives more computational time but not more memory for the calculations (Google n.d.).

# 3.

## Methodology

The methodology chapter follows a certain workflow to obtain results of a new method for water classification that can be compared with other methods but also with the actual situation. The objective of this research is to determine sub-pixel accurate river-width estimations. For this objective, the mentioned workflow is proposed to obtain a different method of classifying with probabilities by using more information than a single band or index. This workflow can be seen in Figure 5 below, where step 3 to step 7 are the steps to carry out the new method and the other steps help to compare and review the method. The workflow is presented as a simple overview of how this new method can be used. Sections 3.1 to 3.7 of this methodology chapter will explain the steps in more depth.

Section 3.1 below, which is step 1 in the workflow, starts with a section about the study location followed by the conducted Ground truth data [collection](#) at the study location. Section 3.2, the second step of the workflow, is a section about [Current cutting-edge method for water classification](#). Step 1 and step 2 are needed to provide an idea about the actual situation and about different classification methods. For a new method, it is of value to compare results with the actual situation but also with other techniques. Therefore, the ground truth collection and the current classification techniques are implemented.

The sections after the current classification techniques are part of the workflow for the new method of water classification. Section 3.3, step 3 of the workflow, describes how discriminating bands can be found for an area of interest. These bands will be checked on site-specific discriminating abilities and can vary between locations. Therefore, the method is for site-specific applications and not intended to be used uniformly for mapping the whole world. The found discriminating bands in step 3 of the workflow, are used for the next step, step 4, to find combinations of bands that show discriminating abilities between land and water.

When the analysis, of step 3 and 4, for discriminating bands and combinations, is done, step 5 is executed in section 3.5, where two methods for image enhancement are investigated on the discriminating bands. Pan-sharpening for the lower resolution SWIR band of Sentinel-2 is applied, followed by bicubic resampling to 1-metre resolution as a preparation for the next step. After image enhancements, the different indices are created in both the original resolution bands but also in the resampled 1-metre resolution bands. Where an edge detection is applied to the 1-metre resolution indices to sample values on the original resolution. The sampled values are used to assign probabilities to each pixel by using the sampled edge values in combination with a CDF curve. The next step, step 7, is performed together with the previous step in section 3.6, where the probability bands are combined by using Bayes theorem for updating probabilities.

The final section and last step, section 3.7 and step 8, will be where the quality assessment is performed with the use of ROC curves in combination with field data to show if probability bands and combinations of these are better in classifying water than current methods.

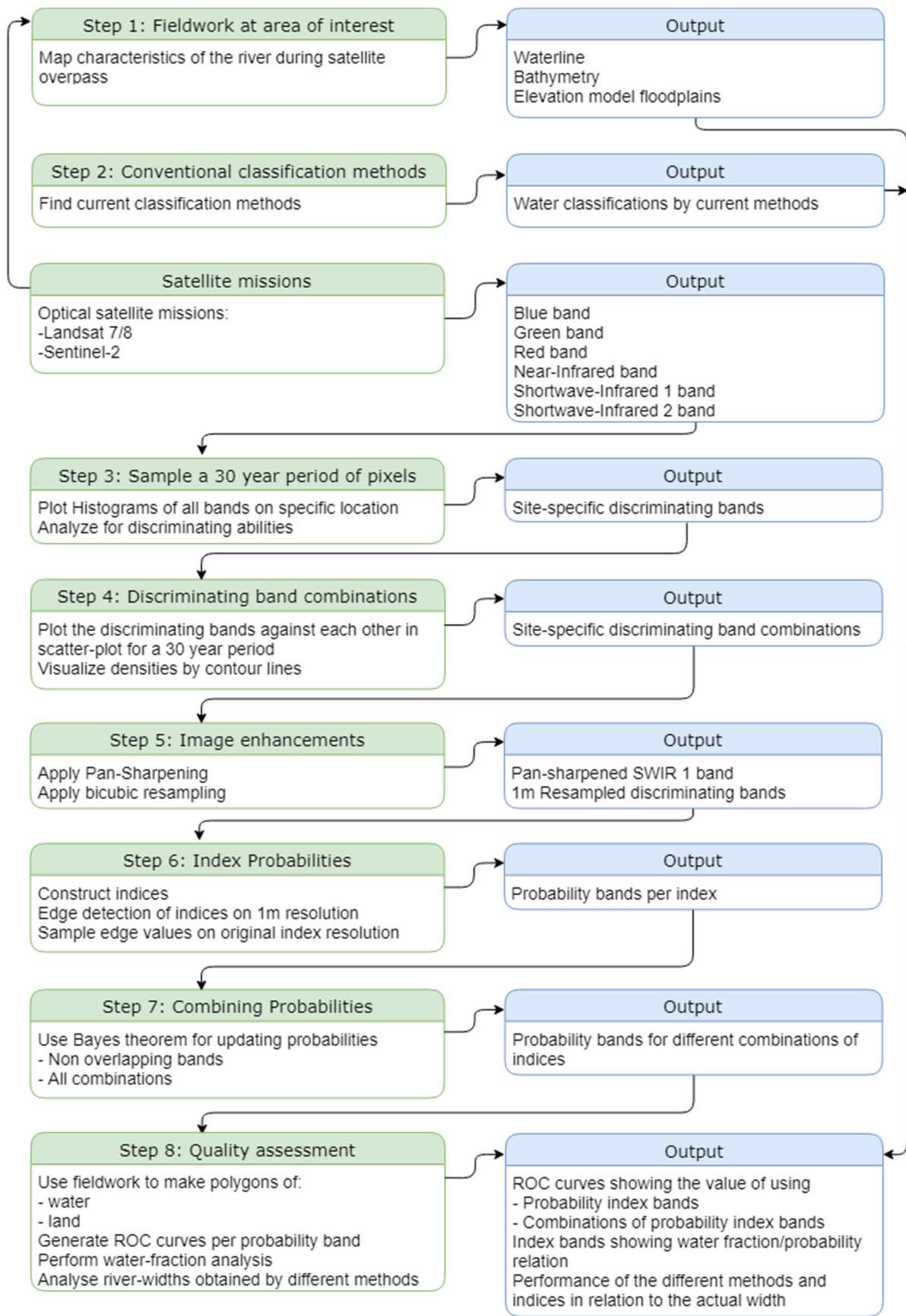


Figure 5 Workflow of the proposed method for classification

### 3.1. Study location

As mentioned earlier in this thesis, the IJssel river basin is taken as a case study for this thesis research. This research is focussed on a new method to determine sub-pixel river width estimation, where finding discriminating bands and combinations to classify water is a part of the research. The discriminating bands for a study location will vary for each location and depending on the condition of land and water. For the application of this research, the methodology is tested on the study location that will be discussed below. Therefore, it is important to know what type of situation, in this case, a river, the research is applied to. The focus of the research and the conducted fieldwork is done at the IJssel river section southwest of the village Herxen, in the Netherlands. The IJssel river basin is discussed in section 3.1.1. The specific study location selected for this research is further described in section 3.1.2. The characteristics of the proposed measuring location used for this research are explained in this part. After this, the fieldwork and the measured components are discussed in section 3.1.3.

#### 3.1.1. IJssel river basin

Noting that reflection patterns of different types of water but also soil differ from each other, the situation needs to be known. This makes sense if one considers applying a water classification method on waters with a high level of suspended sediment versus applying a water classification method on clear mountain waters. The reflectance patterns of these two types of waters are different. For example, the turbid water will show reflectance patterns of water but also of the suspended solids, while clear mountain water, if deep enough, will show mainly reflectance of only water.

The IJssel river is a tributary of the Rhine river. The Rhine river is a river that originates in the Swiss Alps. The River Rhine flows through Switzerland, Liechtenstein, Austria, Germany, France and the Netherlands. The Rhine splits into the main branch called the Waal and the smaller branch the Lower Rhine (Nederrijn) Northwest of Lobith. Southeast of Arnhem, the Lower Rhine branches off a river, the river IJssel. From this point, the river IJssel flows past Deventer and Zwolle into lake IJsselmeer via lake Ketelmeer. Via lake IJsselmeer, the water flows eventually into the North Sea. The river IJssel is a rainfed and meltwater fed river.

The river IJssel has a length of 127 kilometres and its width varies during normal conditions around the 70 to 140 meters (Rijkswaterstaat n.d.). During regular flow, the depth is around four meters. The weir at Driel regulates the proportion of flow through the Lower Rhine and the IJssel. During low flow periods, the weir needs to direct a sufficient part of the flow through the IJssel (Uehlinger and Wantzen 2009).

The flow of the IJssel is a small portion of the total flow of the Rhine, on average 15%, whereas on average 17% of the Rhine flow goes further via the Lower Rhine and 68% via the Waal (Reeze et al. 2017). This means an average discharge of 330 m<sup>3</sup>/s for the river IJssel. The distribution of flow from the Rhine to its tributaries varies as the flow of the Rhine varies. Only the distribution during normative discharge of 16.000 m<sup>3</sup>/s is set by law, which can be seen in Table 3 (Reeze et al. 2017). All other distributions vary due to changes in river morphology of the summer bed but also due to human interactions like the “room for the river” project. These intermediate flows distributions are not set by law.

Table 3 Discharge distribution Rhine branches (Reeze et al. 2017)

Rhine (m <sup>3</sup> /s)	Waal (m <sup>3</sup> /s)	% of total discharge Rhine	Lower Rhine (m <sup>3</sup> /s)	% of total discharge Rhine	IJssel (m <sup>3</sup> /s)	% of total discharge Rhine
750	616	82.1%	30	4.0%	104	13.9%
1000	813	81.3%	30	3.0%	157	15.7%
1250	1006	80.5%	30	2.4%	214	17.1%
1500	1200	80.0%	30	2.0%	270	18.0%
1750	1370	78.3%	70	4.0%	310	17.7%
2000	1461	73.1%	232	11.6%	307	15.4%
2250	1587	70.5%	342	15.2%	321	14.3%
2500	1729	69.2%	425	17.0%	346	13.8%
3000	2049	68.3%	531	17.7%	420	14.0%
3500	2363	67.5%	644	18.4%	493	14.1%
4000	2683	67.1%	756	18.9%	561	14.0%
5000	3355	67.1%	940	18.8%	705	14.1%
6000	4032	67.2%	1122	18.7%	846	14.1%
7000	4690	67.0%	1346	18.8%	994	14.2%
8000	5328	66.6%	1528	19.1%	1144	14.3%
10000	6500	65.0%	2010	20.1%	1490	14.9%
13000	8307	63.9%	2717	20.9%	1976	15.2%
16000	10144	63.4%	3376	21.1%	2480	15.5%

### 3.1.2. Study location southwest of Herxen, Netherlands

The analyses and measurements are performed on the study location southwest of Herxen in the IJssel. This section of the IJssel is chosen due to its straight segment with relative small groins and due to the accessibility of the wide floodplains for measurements. The study location has floodplains on each side of 250 to 300 meters wide. Close to the waterline during normal flow, there is a small summer dike, which is slightly higher than the rest of the floodplain. This means that during higher flows, when the summer dike overflows, the floodplains will be flooded too. The function of the floodplains is mainly for grazing and some farmers grow crops. The winter dike, which is at the far edge of the floodplain, is approximately three meters higher than the summer dike. This dike is the last structure to protect surrounding land, during high flows, from flooding. The study location can be seen in Figure 6. The green polygon is the area of interest for this research. The size of the area is approximately 800 by 800 meters. The west floodplains of the research are privately owned by farmers. The east side is owned by "Staatsbosbeheer", which is a Dutch governmental organization focused on management and preservation of nature.

## Study location

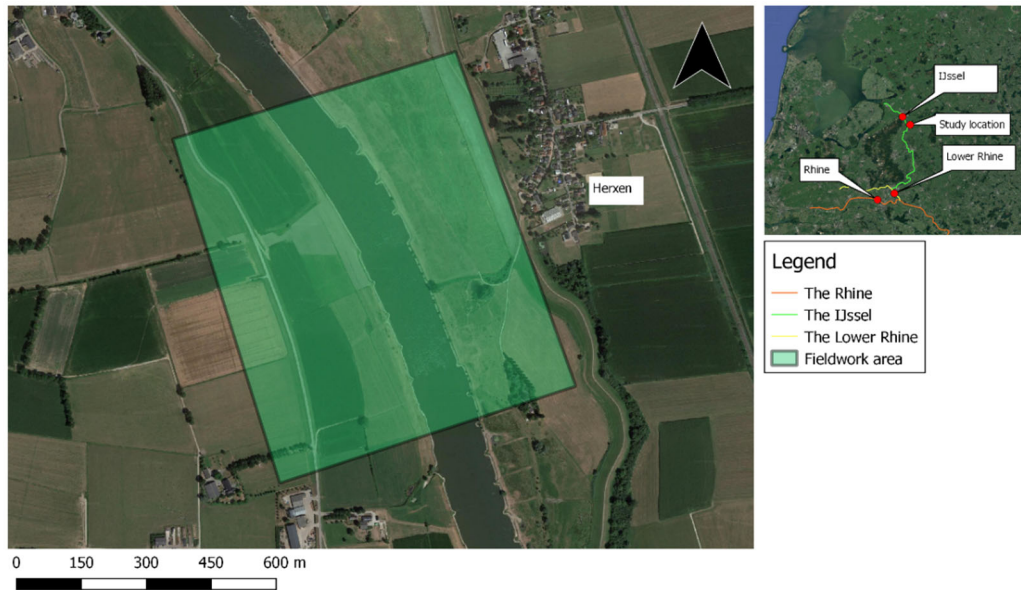


Figure 6 Study location southwest of Herxen

The study area contains no buildings, except for one. On the east side of the river, at the floodplain, there is a house built on a small artificial mound surrounded by trees. During inundation of the floodplains this house is surrounded with water and the mainland is accessed by an amphibious vehicle of the owners. In Figure 7, the mentioned house in the study location can be seen while the floodplains are inundated. During inundation, this section of the IJssel is approximately 600 to 650 meters wide.



Figure 7 Floodplain inundation extend at study location IJssel, Herxen, Domestic house surrounded by water (Hartman n.d.)

### 3.1.3. Ground truth data collection

This research will obtain in the later sections a new method for water classification. The results of this method needed to be compared to the actual situation during satellite overpass but also to other currently used water classification methods. Therefore, this section explains the performed fieldwork and the next section, section 3.2, explains the current water classification methods.

Rijkswaterstaat, the Dutch authority responsible for management and maintenance of the main water-related infrastructures, is already monitoring in the IJssel river. Having noticed that most of the measurements done in the IJssel are continuous point data, measurements in one point, a more elaborated fieldwork mission is conducted to obtain different data on the specific study location. The most common and easy parameter being measured in rivers is water level, while the waterline, the transition of water to land along the river, is something that is not usually measured in the field. The waterline is an important input for this type of research to compare the output of the objective and perform a quality assessment against the river-width estimation from various methods with outer space missions like Sentinel-2.

There are various difficulties possible to encounter when conducting fieldwork at a river to obtain ground truth data for satellite missions. These possibilities needed to be taken into account. First of all, to keep the introduction of errors for comparison as small as possible, the fieldwork needed to be executed at the same day, at the same time, in other words during the satellites acquisition or overpass moment of the area of interest. Therefore, a time schedule was set up to prioritize the measurements for direct comparison to the satellite data during the overpass. Secondly, for good image quality from optical satellites, it was important that a day with a clear sky was chosen for the ground truth data collection. The presence of hazy clouds or shadows of clouds on a measuring day can introduce variations in sensing reflections from the ground and therefore errors in classifying can be introduced (Donchyts et al. 2016). Thicker clouds can even block the reflectance signal from the ground completely, resulting in an image that cannot be used as input data for water detection. Executing measurements on a river, like the IJssel, that is used as a shipping route can also complicate the fieldwork. When certain measurements need to be done on the water itself, the surrounding traffic needs to be closely monitored to avoid hindrance or even dangerous situations. Doing measurements on water, sometimes means accessing the water via someone's property, which can be privately or government owned. Therefore, permission needs to be acquired. Lastly, it was important to double check the equipment before the fieldwork on charged batteries, possible software updates, missing parts and to check if everything still works properly.

While it is important to conduct ground truth data collection on the same moment of the satellite acquisition time, a comparison with a higher spatial resolution image can be made. When the time difference of the two acquisitions is hours or even a day, the water levels can be different and therefore also the location of the waterline. A way to solve this is by measuring the bathymetry of the river and the elevation of the floodplains, like a DSM, in order to create a cross section of the complete river with its floodplains. The combination of the bathymetry and the DSM can then be used to translate water level difference measured by Rijkswaterstaat into width difference for that location.

### 3.1.3.1. Waterline contour

Mapping the exact waterline can be done in various ways. Depending on what is necessary to know a different method can be used. When solely the river width is needed to be known then a Total Station can be used to measure distances from shore to shore. A Total station is a combination of a theodolite and a distance measuring device. However, this method does not enable one to easily map the waterline for a section of several hundreds of meters, while accurately georeferenced. Georeferencing the measured widths can be difficult when this needs to be compared to the satellites' data. Therefore, the choice is made to use a Leica GNSS device to obtain GPS points along the river's waterline. In turn, this can be transformed into a georeferenced waterline that is usable to compare with satellite data. In the section above it is already mentioned that comparing ground truth data to satellite data can be best done under cloud-free conditions. The river IJssel contains some groins at the study location, therefore it is needed to clearly mark the water line at the groins too. On both sides of the river, these GPS points are collected roughly every 50 meters. Each GPS measurement, given by the GNSS device, is programmed to be the average of 5 consecutive measurements.

### 3.1.3.2. Bathymetry and discharge

Bathymetry is referred to as the shape of the underwater surface profile. This profile can be measured simply with a stick to measure the depth and measuring tape for the distances. When the waterbody of interest is becoming bigger than a small stream, for example, the river IJssel, such simple techniques would be difficult to conduct. For larger rivers, an echosounder (a fish finders also contains an echosounder) or an ADCP is more efficient to use. An ADCP (Acoustic Doppler Current Profiler) is chosen to measure the bathymetry but also the discharge. The ADCP itself is a device with several acoustic sensors, a few under an angle and one straight down. The Sontek River surveyor S5 that is used in this research has one vertical beam, and four beams under an angle. The downwards facing sensor tracks its path and measures the depth, while the other sensors measure flow velocities at different depths by using multiple acoustic frequencies. The river surveyor contains a 360 degrees compass and two-axis sensor to measure the tilt (SonTek 2015). The sensor is either attached to the side of a boat or attached to a small floating platform. The latter is preferred to be more stable and also used in this fieldwork.

Known that the river IJssel is around 100 to 120 meters wide on average at the study location it is not possible to use the conventional way of spanning a rope from shore to shore to direct the ADCP over the cross-section of the river. Therefore, an additional boat is needed. In this thesis, a Jet-ski with an extended arm attached to the front is used. The jet-ski is used in the opposite direction of the flow under a small angle to provide sideway propulsion by using just enough throttle to counter the flow of the water. Crossing the river with the ADCP in this manner makes sure that the flow pattern of the river is as little disturbed as possible by the jet-ski. The set-up of this measurement can be seen in Figure 8.



Figure 8 set-up: Jet-ski with the attached ADCP

In total there are three cross sections measured with the ADCP. Each cross section is measured four times by going back and forth twice per cross section. In this way, the measurements can be averaged out and possible large outliers can be left out if needed. Like mentioned in section 2.1.3 ADCP's are not able to measure the full cross-section of a river. The top and bottom layer of the river and a part of the sides, where it is too shallow, are not possible to measure by the ADCP. The provided process software of the ADCP, called RiverSurveyor Live, takes these missed areas into account by interpolation. Therefore, it is important during the ADCP survey to notate in the program at what distance from the bank the sensing starts.

### 3.1.3.3. Photogrammetry of the floodplains

Photogrammetry is the study of interpreting and measuring from photos. This technique is used to map the floodplains of the river IJssel. The photos of the floodplain are transformed into a DSM (Digital Surface Model). To capture the floodplain extent of the river IJssel a drone is used. In this research the DJI Phantom pro 4 has been deployed to follow a grid, with 80% overlap in each photo, to map the floodplains of the study location. The drone was programmed to follow this path with the free mapping software Pix4D Capture. In this application, it is possible to set the overlap percentage, flight speed, flight height, camera angle and the area to be mapped. The application will show the approximated time of flight and the size of the drawn area to be mapped. Also, the direction of the flight grid can be changed. In this research the drone is flown, to have 80% image overlap, at 50 meters height, perpendicular grid to the river, at fast flying speed and with a camera angle of 15 degrees off forward-looking. Before the flight, GCPs (ground control points) need to be placed in the mapping area. As GCP point, a blocked board, a so-called 'Chessboard' is used, which will be well visible in the photos that will be taken by the drone. An example of the used points can be seen in Figure 9. With the GNSS device, the precise location of these GCPs was measured in the x, y, and z-direction. The GPS locations are in the RD projection, EPSG: 28992. The photos of both sides of the floodplains of the river are then processed with the photogrammetry software Pix4D Mapper. The input for this program are the GCPs GPS locations and the floodplain photos. The output will be a DSM and an orthomosaic photo. An orthomosaic photo is a merged RGB photo of all pictures used to create the DSM. The output of the DSM will be used together with the river's bathymetry to construct a cross-section of the river including the floodplains.

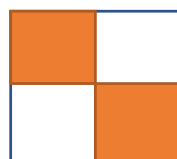


Figure 9 GCP

### **3.2. Current cutting-edge method for water classification**

To validate a new water classification method it is important to know, what other methods are used for water classification and how these methods perform. The two general types of water classification supervised and unsupervised classifications, are already mentioned in section 2.2.3 of the theoretical background.

The ground truth data of this thesis is used to make a quality assessment of the different methods. Supervised methods, that need a training map to be generated, need ground truth data to work. To compare the new water classification method of this thesis with an existing method, a classification technique is chosen that does not rely on ground data either. The cutting-edge method of Otsu is used to find bimodal distributions for thresholding. This method is chosen for comparison due to its ability to obtain a threshold individually per image, instead of taking an average threshold to apply to all images.

Otsu is used to classify water in a conventional way, by using the indices NDWI and MNDWI separately. This creates two water classifications. The Otsu thresholding with NDWI has a resolution of 10-metre and the thresholding with MNDWI has a resolution of 20-metre. Section 2.2.2 already mentioned that MNDWI is better in coping with separating bare-soil and water than NDWI. This means that while NDWI has a higher resolution, more spatial detail than MNDWI, it has more confusion with land classes, which results in misclassification of land as water.

In section 3.5, an image enhancements technique will be used to create a 10-metre resolution band of SWIR1 instead of 20-metre. With this higher resolution SWIR1 band, an  $MNDWI_{10}$  will be made. This is the same index as the MNDWI, but due to the 10-metre resolution SWIR1 instead of the original 20-metre band, an  $MNDWI_{10}$  of 10-metre resolution is obtained. This  $MNDWI_{10}$  is also used to apply Otsu, resulting in three different Otsu classifications.

Besides the Otsu method, the results of using a training map from the collected ground truth data for classification has been obtained as a second method to compare the new method to.

In section 2.2.3, the differences between supervised and unsupervised classification are explained, as well as the theoretical background of Otsu in detail.

### **3.3. Finding discriminating bands between water and land**

Every location has specific conditions due to different land uses but also with different types of water. Therefore, the conventional water indices can turn out to be less effective in certain areas, due to the varying absorptions of light at certain bands. As mentioned in section 2.2.2, misclassification can occur when land and water classes have similar patterns in the used bands for classification. Different land use types will have a strong inter-class variance when the two used bands for an index have a different pattern in their signal. This means that when, for example, water shows an increase in signal from band 1 to band 2 of an index and the other land uses show a decrease in signal, a discriminating behaviour is found. Using a normalized difference index of such band combinations strengthens this behaviour. When the band values between water and land uses are different but both increase from band 1 to band 2, misclassification can occur. This is what can happen with the NDWI index between water and built-up land but also with certain types of soil (H. Xu 2006a). Conventional indices can turn out to be not the most optimal indices for water classification in the area of interest. This can be due to the possibility of better water discriminative abilities in other bands than in the green and Nir bands for the NDWI and, than the green and SWIR for the MNDWI. The variation in performance of the conventional indices, NDWI and MNDWI, depends on the types of land use and on the type of water in the area of interest. To avoid analysing each land use in the study area and combining these with a certain index, a different

approach is used. Therefore, in this part, a method is used to assess the discriminating abilities of the bands obtained by the used optical remote sensing satellites, like Landsat 7/8 and Sentinel-2

To research site-specific discriminating bands, Google Earth Engine is used with a Python API. With this API, a connection is made with Google Earth Engine and the ability to work in Python is enabled. Using Python in Jupyter Notebook works well when one wants to apply different types of plots and calculations from packages. Special packages are made for Python, which helps with certain analyses and visualizations that are not embedded in Google Earth Engine.

To show distributions of data, histograms can be used. The method of researching site-specific discriminating bands is performed by plotting all pixel values of the Area Of Interest (AOI) that contain the two land types that need to be discriminated, in this case, land from water. The idea is to use not a single satellite image but images from several years together to form a general picture of the data that is not specific for one moment in time. Landsat missions exist for many years already, which means the different Landsat mission provide a lot of years of data that can be used for analyses on discriminating abilities of the bands. Landsat 4, 5, 6, 7 and 8 are used to examine the bands, which means many years of data is available where the last 20 years are used. The bands for comparison are the blue, green, red, NIR, SWIR1 and the SWIR2 bands. All images from the different Landsat missions are merged into a collection of images followed by adding a cloud and snow score to the images. To filter out the majority of the cloud and snow invested images, a cloud and snow score is made, where only the images are left with a cloud and snow score less than, respectively 0.2 and 0.3. The cloud score is only used to detect the large obvious clouds. The cloud score is based on brightness, temperature and the NDSI (Normalized Difference Snow Index). It makes use of these three indicators and takes the minimum value of the indicators as relative cloud likelihood, which are designed for Landsat as proposed by the Google Earth Engines Developers guide (Google n.d.). The same is done for a rough and quick snow score, which also makes use of brightness, temperature, and  $NDSI_{rd-sw}$  (Snow Index from red and SWIR1). After merging the images to one collection and adding cloud/snow scores to the images, it means that the data is still in image format, therefore, all pixel values are converted into a DataFrame. Every pixel is a new row, with its coordinates and band values in the different columns. From this point, it is possible to use the pixel values for analyses and plotting.

As mentioned above, histograms are a way to visualize distributions of data, therefore, all bands are plotted in a histogram. If a single band shows a bimodal distribution, it is evident that there is a discriminative ability in the band. It still needs to be checked if this bimodal signal corresponds to the difference between land and water. A band can also show a distribution that does not contain visually a noticeable bimodal signal. Also, in this case, it is needed to check where the mean water values and the mean land values are located on the histogram. Via this method, it can be seen if there is an inter-class variance between land and water or not. Bands that show mean values of land and water at the same location on the histogram are rejected as discriminating bands of land and water.

### 3.4. Finding discriminating band combinations for custom normalized difference water indices

Conditions vary per study location, as already mentioned in chapter 3.3, and therefore also the possibility that the discriminative bands, to distinguish land from water, vary. The conventional water indices, NDWI, and MNDWI make use of the assumption that, respectively, green and NIR, and green and SWIR are the discriminating band combinations. One of the objectives of this research is to find a method to determine not only what bands are discriminative but also what combinations are discriminative, like the assumption behind the NDWI and the MNDWI is. To find out if there are other combinations to classify water and land from each other, again the pixel values of the AOI are used to find site-specific discriminative combinations. The analysis of chapter 3.3 is used to make combinations of the bands with discriminative abilities for land and water.

The method of chapter 3.3 is for this part of the method the same until the part of sampling the images to a DataFrame. Instead of making histograms per band, combinations of two bands are visualized via a scatter plot. The data contains tens of thousands of pixels, therefore the size of each point in the scatterplot need to be small to prevent the loss of detail due to the many points. The objective is to find a separation of classes, in this case, separation of the water and land class. By just looking at the points in the scatterplot it can be difficult to retrieve discriminative abilities as there are so many points. Therefore, to better visualize the details in the scatterplot, a non-parametric density function is used. The kernel density estimation (KDE) is applied to the bivariate distribution by a Gaussian kernel. An example of a univariate kernel density estimation is by converting, from a histogram obtained by 100 random uniformly distributed numbers, which does not show a smooth probability density function (PDF) due to the bins, a smooth function as probability density function (Bilock, Jidling, and Rydin 2016). The KDE makes from every bin a Gaussian distribution and sums these to create the final PDF of the histogram. An example of a PDF by KDE can be seen in Figure 10.

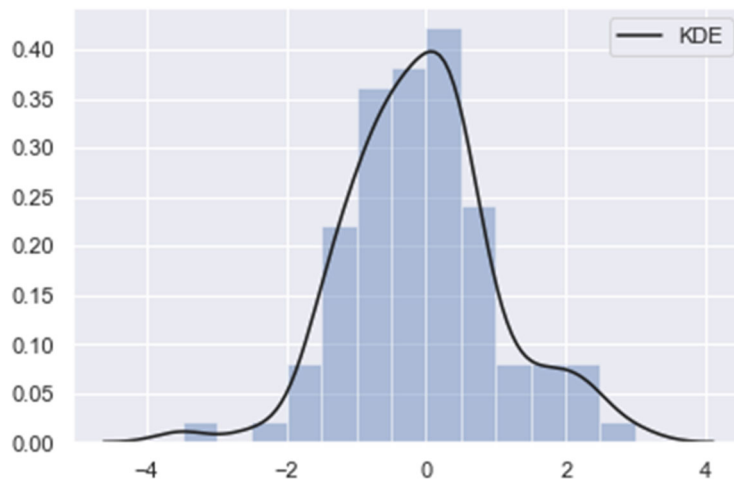


Figure 10 Example of KDE histogram

A bivariate kernel density estimation is obtained the same as a univariate only 2-dimensional, by making Gaussian kernels (PDF's) around each data point and then summing these kernels, this can be seen in Figure 11. A kernel distribution estimation on a scatterplot of two bands could show inter-class variance. Therefore, this method is performed to find discriminating abilities between two bands for water and land, that can be used to make new indices for better classification purposes. The possible combinations can later be used when multiple indices will be combined in section 3.6.2.

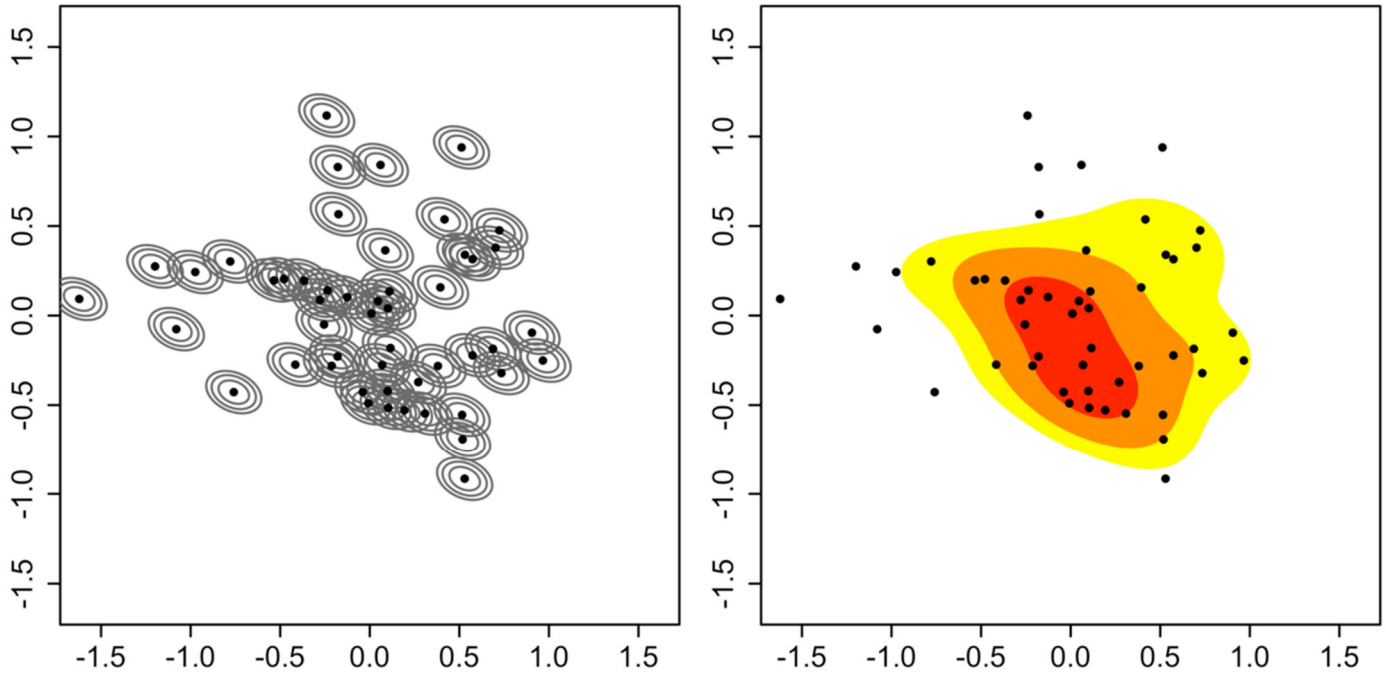


Figure 11 (left) kernels around each data point, (right) kernel density estimation (Wu, Wang, and Xiao 2018)

### 3.5. Image enhancements to improve water classification abilities

There are several methods to enhance satellite imagery to improve water classification. The main disadvantage of mixed land and water pixels is the possible introduction of substantial errors when estimating the river width. When using the conventional water index (NDWI) or the modified water index (MNDWI), the pixel size will be, respectively, 10 metres and 20 metres. Especially when in literature is found that the MNDWI has better discriminating abilities than the NDWI (Du et al. 2016), by lowering the confusion of built-up land classes as discussed in section 2.2.2. By using the MNDWI instead of NDWI, the classification ability goes up in terms of less confusion between land uses, but the spatial resolution goes down of one band, from 10-metre to 20-metre. To counter for this coarser resolution, different enhancement methods are tried.

Pan-sharpening is a concept of using a certain panchromatic band with high resolution to transform low-resolution bands into high-resolution bands. The panchromatic bands have lower spectral resolution and have usually overlap of multiple bands in the spectral domain. With the panchromatic band of Landsat 7/8, the spectral domain covers the blue, green, red and near-infrared domain (Rubayet Rahaman, Hassan, and Razu 2017). The bands of Landsat 7/8 have a resolution of 30-metre and the panchromatic band of 15-metre Sentinel-2 however, does not have a panchromatic band. But the blue, green, red and near-infrared bands are in 10-metre resolution and the SWIR bands have a 20-metre resolution. According to literature, there is considerable research done to see what 10-metre resolution band of Sentinel-2 can be used as a panchromatic band for the SWIR bands (Vaiopoulos and Karantzalos 2016). Research showed that the near-infrared is well capable to be used as a Panchromatic band to sharpen the SWIR band (Du et al. 2016). Pan-sharpening is done via the IHS pan-sharpening method. IHS is short for Intensity, Hue, Saturation method. This method transforms RGB bands to IHS bands. Three bands have to be chosen using this method. Therefore, the chosen bands were SWIR1, green and blue. The SWIR1 band needs to be transformed into 10-metre resolution via this method and the green and blue bands are already 10-metre resolution. The Intensity band is

then switched with the panchromatic band in the IHS. A reverse IHS was then applied on the panchromatic band, the hue and the saturation band to RGB. The output bands of the reverse IHS conversion gave the SWIR1, green and the blue bands. The SWIR band with its original resolution of 20-metre, was, as a result, pan-sharpened via the IHS method by using the NIR band as a panchromatic band.

Resampling is the second image enhancement technique used in this method. Resampling is used to obtain a new set of coordinate points from a known grid. Resampling contains two steps, first the data is interpolated into continuous data, so an interpolated fit is applied, afterwards, the continuous data is resampled back to a new grid (Parker, Kenyon, and Troxel, 1983). Resampling was used in this section of the methods to obtain a smaller pixel size, obtained by interpolation with neighbouring pixels. The resolution was resampled to 1-metre resolution. There are multiple ways of resampling, which can be seen in Figure 12. Nearest neighbour is the standard method Google Earth Engine uses. The downside of the nearest neighbour resampling is that it takes the value of the closest pixel to the point of interest. Nearest neighbour resampling does not preserve sub-pixel data due to the shift to the nearest neighbour in value (Parker, Kenyon, and Troxel 1983). Linear resampling takes the linear value between two pixels and thereby uses more information about the surrounding than the nearest neighbour technique. Cubic resampling takes four pixels and fits a third order function (cubic polynomial) through the data (Richards and Jia 2013). The three just called resampling methods can also be performed in two dimensions. As mentioned above, the difference between these techniques but also between one or two dimensions are visualized in Figure 12. For this research, to, later on, obtain a smooth river edge during edge detection for sampling purposes, the resampling technique is chosen to be 'bicubic' due to its property of taking 16 surrounding pixels into account for the interpolation. The downside of cubic and bicubic resampling is that this method sometimes overshoots its fit, possibly causing indices to exceed its maximum and minimum.

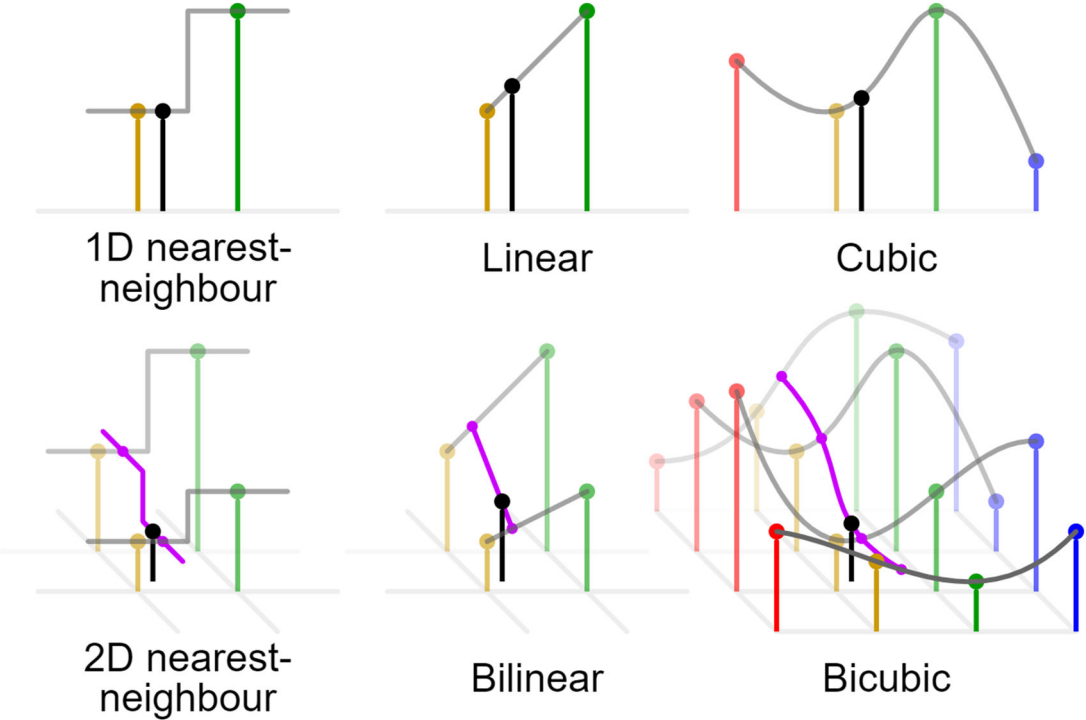


Figure 12 Resampling techniques visualized (C. Lee n.d.)

### **3.6. Combining normalized difference indices to improve classification**

After the analysis of discriminating bands and band combinations, the analysis between the combinations can be made. The objective of this part of the research was to use a more probabilistic method, instead of a binary option for water and land classification. The indices are coupled to probabilities first, instead of immediately, for example via a threshold, to ones and zeros to indicate the class. As seen in this research, the coarse resolution of the original image gives problems near the side-banks of the river for accurate classification. Therefore, the side banks were used to obtain data on the distribution of the various index values that could be encountered. Before any analysis on the data is done, the indices need to be created. The NDWI and the MNDWI are constructed, as well as the indices of the found discriminating combinations, which are presented in the results of section 4.4.

#### **3.6.1. Obtaining index probabilities**

A pixel on the edge of a river will most likely contain some percentage of land but also of water. The percentage of each class, in that pixel, is variable depending on the location of the pixel. Some pixels are located on the river banks with a small section that overlaps with water. Other pixels consist mainly of water with a small percentage of land and many will be between these two cases. From this perspective, the choice was made to sample the values of the indices on the river edge each into a cumulative distribution function. This was done with the wide range of mixed pixels on this edge, ranging both from mainly water to mainly land in the pixels. The edge of the river was found by searching for gradients in each index. To search for edges on the river banks, first, the indices needed to be created, from the discriminative band combinations of section 3.4. The indices are known to differ in value for land and water. Therefore, when a certain gradient is detected in one of these indices, it can be seen as a transition between classes. To correctly assign the right gradient threshold for river edge detection, a visual inspection was performed to obtain the correct gradient threshold where mainly the river edge was seen as edge and not spurious other locations. To better perform the edge detection, the images were first resampled to 1-metre resolution. By resampling the index bands, the edge that was detected resulted in a smoother line that goes through the original pixels instead of edge detection on the original resolution resulting in a line around the pixels. In this way, the actual edge values of the mixed pixels were sampled using the original resolution instead of pixels on both sides of the detected edge.

Edge detection is performed by the CannyEdgeDetection method. J. Canny describes his developed edge detection method as follows: 'The optimal detector has a simple approximate implementation in which edges are marked at maxima in gradient magnitude of a Gaussian-smoothed image.' (CANNY 1987). Gaussian smoothing is performed to reduce noise in the image by convolution of Gaussian distributions in the middle of the pixel values. Further in this research edge detection is used to refer to the CannyEdgeDetection method. When edge detection is performed on the original resolution, the edge will give a rugged line between pixels. When sampling this rugged line, index values of pixels of both sides of the line will be taken, while the goal was to take the mixed pixel values. The edge obtained on the resampled data is used on the original resolution and not on the 1-metre resolution data to exclude results from interpolated values that can cause misleading results.

As mentioned above in this paragraph, the sampled values of the edge are transformed into a CDF curve. The objective of using the CDF curve was, by keeping in mind that the data of the mixed pixels in the river's edge are sampled in this CDF, to connect all index values to a probability of being water. Values outside the range of the CDF will be assigned to its nearest values. Meaning that values of, for example, NDWI, that are below the minimum value of the CDF will be assigned to the probability of the minimum value in the CDF. The same works the other way around above the maxima.

The use of the CDF of the sampled edge values means that every pixel for each of the different indices is used to calculate the probability of water. A new band per index was created with the probability values.

### 3.6.2. Bayes theorem for combining index probabilities

The second part of this chapter is about combining indices, instead of considering and comparing only single indices. By creating probabilities of being water for each pixel, separately per index in the previous section, the base is set to be able to combine multiple indices. In this research, Bayes theorem is used to update a prior probability by the newly gained probability by an index (Triola 2010). There were two classes to consider, water and land. By taking an area that contains both classes, without any other knowledge, the a-priori-probability can be taken as 50% for a pixel to be water and 50% for a pixel to be land. As Bayes theorem was used to update probabilities, the number of index probabilities can be varied to calculate different posterior probability. Bayes theorem for updating the prior of a pixel being water, by an index, can be described as:

$$P(W_{x,y}|I) = \frac{P(I|W_{x,y}) * P(W_{x,y})}{P(I|W_{x,y}) * P(W_{x,y}) + P(I|\overline{W}_{x,y}) * P(\overline{W}_{x,y})} \quad (8)$$

$P(W_{x,y})$  is the prior of a pixel at  $x, y$  being water,

$P(\overline{W}_{x,y})$  is the prior of a pixel at  $x, y$  not being water,

$P(I|W_{x,y})$  is the new information by the index probability of being water,

$P(I|\overline{W}_{x,y})$  is the new information by the index probability of not being water,

$P(W_{x,y}|I)$  is the probability after being updated, the posterior.

The probability of a pixel being land can be described by:

$$P(L_{x,y}|I) = 1 - P(W_{x,y}|I) \quad (9)$$

Equation 8 shows how an index probability can update the prior with Bayes theorem. Equation 10 below shows how multiple index probabilities can be used to calculate a posterior probability.

$$P(W_{x,y}|I_1, \dots, I_n) = \frac{P(I_1|W_{x,y}) * \dots * P(I_n|W_{x,y}) * P(W_{x,y})}{P(I_1|W_{x,y}) * \dots * P(I_n|W_{x,y}) * P(W_{x,y}) + P(I_1|\overline{W}_{x,y}) * \dots * P(I_n|\overline{W}_{x,y}) * P(\overline{W}_{x,y})} \quad (10)$$

Via this way, combined bands are created, with the posterior probability for every pixel in the area of interest. The side note of Bayes theorem of updating probabilities is that this theorem uses the assumption that the new information is independent of the prior information (Triola 2010). Projected on this research, it means when one wants to apply this theorem it is not statistically correct to use combined indices that make use of the same data. Therefore, it should be avoided to combine two indices that make use of the same band. At this point, the discriminating band combination analysis of section 3.4 plays a role to construct the right indices that can be combined via Bayes theorem.

By constructing probability bands for the available indices and by combining these via Bayes theorem, a set of comparison material is created that can be checked on its functionality. The quality assessment of these probability bands will be executed in the next step of the workflow that can be found in the next part of this chapter in section 3.7.

### 3.7. Quality assessment of methods with in-situ measurements

The quality assessment is needed to reference the results obtained during this research to the collected ground truth data and to conventional methods to analyse its results. The fieldwork was conducted during a satellite overpass, therefore the collected ground truth data can be used to verify and assess the methods. During the ground truth data collection, the waterline was mapped with a high-end GPS system.

#### 3.7.1. ROC analysis

The waterline data is used to create a vector layer of water areas and a vector layer of land areas. The satellite data with the probability bands of each index for the study location is clipped on these areas into a water raster layer and a land raster layer. These two raster layers are used to assess the quality of the classification methods. With the help of the water and land layers, a Receiver Operating Characteristics (ROC) curve can be made for the classification bands of the different indices.

A ROC curve can be used to visualize the performance of classifiers (Fawcett 2006). There are four classification rates when analysing a classification method for two classes. The objective is to relate the performance of the classification on one of the two classes. In this case, a method for water classification is developed. Therefore, the classification will be checked for correct classification of water with the use of ground-truth data. Correct classification of water is then called a Hit (True Positive). When an area is correctly classified as non-water, it is called a correct rejection (True negative). These two situations can also occur when an area is not correctly classified. For example, an area that is classified as water while it is non-water, this is called a false alarm (False Positive). The other way around when water is classified as non-water it is called a miss (False Negative). These four situations can be turned into rates. The two rates that are needed to construct a ROC curve are the True Positive Rate (TPR) and the False Positive Rate (FPR). The formulas for these two rates can be seen in equation 11 and 12.

$$TPR = \frac{\sum W_{correct, th}}{\sum W_{correct, th} + \sum L_{false, th}} \quad (11)$$

$$FPR = \frac{\sum W_{false, th}}{\sum W_{false, th} + \sum L_{correct, th}} \quad (12)$$

The True Positive pixels,  $\sum W_{correct, th}$ , with the False Negative pixels,  $\sum L_{false, th}$ , for a threshold form together all the pixels of the water raster layer. This is indicated by the denominator of formula 11. The False Positive pixels,  $\sum W_{false, th}$ , with the True Negative pixels,  $\sum L_{correct, th}$ , for the same threshold as for TPR, form together all the pixels of the land raster layer. This is indicated by the denominator of formula 12.

The indices used are normalized difference indices and therefore range from -1 to 1 in value. However, in the previous section, the different indices are changed for the new method into probability bands based on the edge distribution of the index and range from 0 to 1. Two types of ROC curves are constructed.

The first type is based on the conventional method of using a single index for classification based on the index values. For the first type, the TPR and the FPR are calculated for a range of threshold in the same domain as the index bands, from -1 to 1. This is done in 200 steps with a step size of 0.01. The number of 200 steps is chosen to get a balance between enough detail and low calculation time.

The second type is based on the new method, which uses the probability bands of the indices. For the second type, the TPR and the FPR are calculated for a range of threshold in the same domain as the probability index bands, from 0 to 1. This is also done in 200 steps, which results in a step size of 0.005. For every threshold, a TPR value and an FPR value is created. When the output arrays of the FPR and the TPR values are plotted against each other a ROC curve is made.

The Area Under a ROC curve (AUC) determines how well a classification method works and in theory can range from 0 to 1 (Fawcett 2006). If the AUC is equal to 1, then a perfect discriminating classification method is found. The larger the area under the curve, the better the classification or in this case the index is in discriminating the two classes. AUC values below 0.5 mean that the classification is mirrored and therefore needs to be switched. When random guessing is applied, a diagonal line will be produced. The AUC of this diagonal line from (0,0) to (1,1) is equal to 0.5. Therefore, a classification AUC result should be between 0.5 and 1 to have a valid ROC curve.

A ROC curve can also determine, based on the curve, the optimal threshold for classification. The optimal threshold corresponds to the point on the ROC curve with the lowest distance to the upper left corner in point (0,1). The point in the upper left corner indicates a perfect classification, where there is a TPR of 1.0 and an FPR of 0.0.

As mentioned earlier in this section, two types of ROC curves are constructed. The first type, with ROC curves of all index bands, are shown in one curve to visually analyse the different results of the index classifications.

The second type with ROC curves of all probability bands of the indices but also combinations of these probabilities are shown in one curve to visually analyse the different results of the new type of classification.

### 3.7.2. Water fraction pixel analysis

The second last part of the quality assessment will consist of a sub-pixel analysis. The objective of this part of the analysis was to see if the pixels water fraction has any correlation with the probability of the pixel being water for an index or combination of indices.

The waterline is measured on both fieldwork days. The waterline was measured by point measurement with the GNSS device. The measured points on the waterline are used to calculate the water fraction of the corresponding pixels of these points. The measured points were connected to make a water polygon. This water polygon overlaps pixels partly on the edges. Google Earth Engine was used, first to calculate the area of each pixel in an area map, which has a resolution of 10-metre. After this step the area map was clipped on the polygon, resulting in complete pixels inside the polygon and in cut-off pixels on the edge of the polygon with their corresponding area per pixel. This was done for the waterline on the West side of the river and the East side of the river, for both days. The end member measurement points are not taken into account, because no accurate waterline could be drawn without further points to connect. Only the pixels under the GNSS measurement points are used for this analysis. This is done to prevent errors due to the interpolation of the waterline between the GNSS measurement points.

The pixels under the measured waterline points are sampled on all probability index values but also on the combined index values via Bayes theorem. To see the variation between the West and East bank and between both fieldwork days, these are all plotted into one graph per band, either probability index band or combined index band. A combined linear trendline of the sides and fieldwork days is plotted with its corresponding R-squared value. The R-squared value gives an interpretation of the correlation between the fraction of water in a pixel and the probability of being water derived by an index. The R-squared is the Pearson function squared, with a range of 0 to 1. Where an R-squared of 1 indicates a

perfect predictable dataset by a linear function (Bolboaca and Jantschi 2006). The formula for the Pearson function is as follows:

$$R = \frac{\Sigma(x-\bar{x})(y-\bar{y})}{\sqrt{\Sigma(x-\bar{x})^2 \Sigma(y-\bar{y})^2}}, \quad (13)$$

where, in this case,  $x$  is the water fraction of the pixel of interest and  $y$  is the probability of the same pixel being water set by the probability index.

### 3.7.3. River width analysis

In this section, the approach for the river-widths comparison is explained. Otsu's method, supervised training map classification and the newly proposed method are compared to the actual width measured by the GNSS device. The river width determinations are performed between the GNSS measurement points, as these points are measured on the water edge. The amount of measurement locations is limited to the amount of GNSS present on both sides of the river.

The site-specific indices are used to determine the river-width by Otsu. The conventional NDWI and MNDWI, are among the found site-specific indices. These site-specific indices can be found in Table 7 of section 4.4. The obtained river-widths will be compared to the actual width by calculating the deviation. Because Otsu only classifies on a pixel base, the results will probably vary with the measured location, due to the pixel placement on the actual river's edge, as can be seen in Figure 18. Therefore, all indices are used to obtain river-widths at every measurement location.

Secondly, the river-width results of the supervised training map classification are also compared to the actual width by calculating the deviation of the estimated river-widths to the distance between the GNSS points of the locations.

As of the last comparison, the river-width obtained by the probability bands and combined Bayes bands are compared to the actual river-width. The river-widths from the probability bands and combined Bayes bands are obtained by using the optimum thresholds based on the ROC curves. This means that, just as with the Otsu results, the classification is on a pixel base. The best performing probability index and the best performing combined Bayes index of the water fraction pixel analysis explained in section 3.7.2, will be used to perform a sub-pixel based river width determination. The found relation in the previous section, explained in section 3.7.2, between the water fraction of a pixel and the probability of a pixel being water for an index is used to obtain the water content of the mixed pixel on each side of the river to contribute to the river width measurement.

# 4.

## Results and discussion

In this chapter, the results and discussion of this research will be presented. The results and discussion chapter follows the same workflow for the new method for water classification as the chapter Methodology does. The order of this chapter follows the same order as used in the Methodology chapter, which is derived by following the steps of the workflow of the new method. The objective of this research was to determine sub-pixel accurate river-width estimations. For this objective, the mentioned workflow, that can be seen in Figure 5, is executed and the results and discussion about these results can be found in the subchapters below.

### 4.1. Ground truth data collection

Ground truth data collection, as mentioned before in this research, is important to compare and validate results obtained via remotely sensed data. During the Ground truth data collection of this thesis, various different measurements were conducted. In total there are two ground truth data collection/fieldwork days conducted. Ground truth data collection during a fieldwork mission can turn out to be challenging on its own. The first fieldwork day is conducted on the 7<sup>th</sup> of December in 2018. Unfortunately, this was a day with the presence of thick clouds that resulted in an unusable satellite image of that day. One of the measurements, that can be seen in Figure 13, shows the waterline measurements conducted with the GNSS device, the high-end GPS.

## Waterline measurements



Figure 13 Waterline measurements by GPS \*07-12-18 missing the groynes extend

The GNSS output was point data every 30 to 70 metres with an average error in the x/y direction and z-direction of 0.01 metre. During the first fieldwork day, the outline of the water extent was not fully measured. The extent of the groynes in the water was not taken into account with the GNSS measurements. Therefore, in Figure 13 the left waterline, measured on 07-12-18, is missing the shape of the present groynes. The second day of fieldwork, on 15-02-19, did include the groynes in the measurements, resulting in a more complete and accurate measurement. The measured points were chosen in such a way, that connecting the points would show a close resemblance of the waterline including the groynes. The waterline measured on the first measuring day may not contain the extent of the groyne but in between the groynes, the waterline does follow the actual extent. The waterline is measured on both sides of the river. The west side of the river contains a longer section on both days, this was done to create an approximation of the water surface slope. The visual results of the water surface slope can be found in Figure 66 and Figure 67 of the appendix at the section [Water slope](#). The first and the second fieldwork day resulted in a water surface slope of respectively 5 cm/km and 6 cm/km.

The ADCP measurements were conducted on the first measuring day. The output of the ADCP was discharge data and bathymetry data. The three ADCP crossing locations can be seen in Figure 14. As mentioned in section 3.1.3.2, per location four measurements were conducted to obtain a more precise discharge by averaging the measurements. This was possible since the assumption was made that the discharge of the river does not change significantly within the time of measuring, which was roughly 20 minutes per cross section. Later, this was confirmed by comparing the discharge difference according to the upstream measurements at Olst of Rijkswaterstaat, which increased with 1m<sup>3</sup>/s during the fieldwork day.

## DSM by photogrammetry

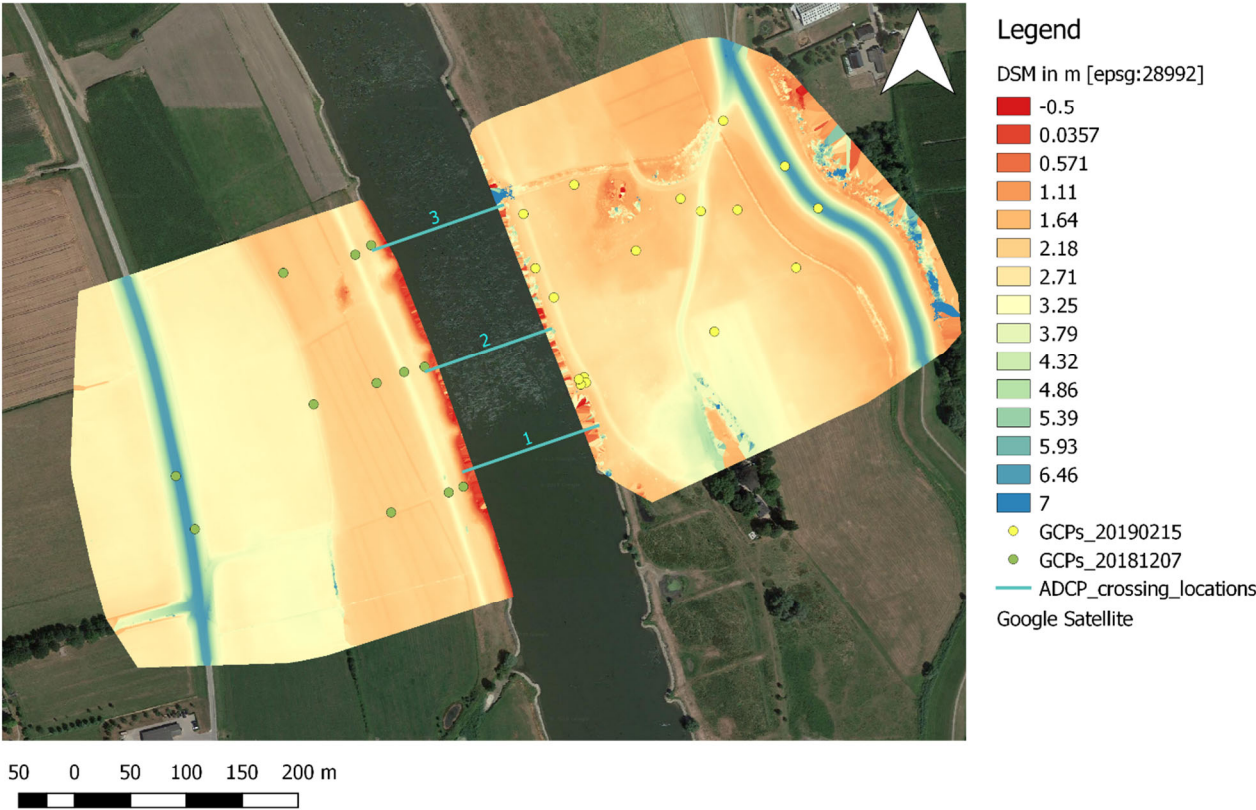


Figure 14 DSM of the floodplains with the ADCP crossing locations

The ADCP discharge measurements at the three cross-sections were all in the same order and the maximum deviation from the average discharge of 201 m<sup>3</sup>/s was 3%, indicating precise measurements. The measurements of Rijkswaterstaat however, showed 183 m<sup>3</sup>/s during the same period. This difference can be due to several reasons. One of the reasons is that the rating curve at Olst could be outdated and is therefore not accurate for the current river situation anymore. Secondly, the water level measurements near Olst could be off, that are used to obtain the discharge via the rating curve, are off. Thirdly, inflow from tributaries between the water level measurements near Olst and the study location could contribute to extra discharge measured. However, there are no substantial tributaries between the study location and Olst that can account for the difference in discharge. Lastly, the discharge measurements of the ADCP can differ from the true discharge due to interpolations at the top, bottom, and sides of the river. The rating curve of Rijkswaterstaat is also constructed via ADCP measurements but then attached to a ship instead of a jet-ski. This means that measurements from the ship of Rijkswaterstaat has even more interpolated values than with the ADCP attached on a jet-ski (Figure 8) as used in this thesis.

The digital surface modelling via photogrammetry software of the obtained photos with the Unmanned Aerial Vehicle (UAV), the DJI Phantom 4 pro-drone, was conducted in two days. During the first fieldwork day the west side of the IJssel at the study location was mapped and during the second fieldwork day the east side of the river. The water level difference between both fieldwork days was around 1.7 metre according to the GNSS device. Due to the higher water level at the second fieldwork day, a part of the east floodplain could not be measured, this was due to this part being under water. The results of the DSM can be seen in Figure 14 with the locations of the used ground control points. The photogrammetry software Pix4d reported a Root Mean Squared Error, RMSE of the west side and the east side of respectively, 0.011 metres and 0.012 metres. In Figure 14 it can be seen that there is on both of the DSM's a summer dike close to the waterline, light coloured line in the DSM, that is lower than certain parts of the floodplains. When the summer dike overtops during a flood, not the entire floodplain will be flooded immediately.

The bathymetry of cross-section 1, location is visualized in Figure 14, is combined with both DSM's to obtain a cross-section of the flow area of the river. The bathymetry of the ADCP output is used together with the DSM of the west and east side of the river to construct a cross-section of the river with its floodplains. The result of the cross-section can be seen in Figure 15.

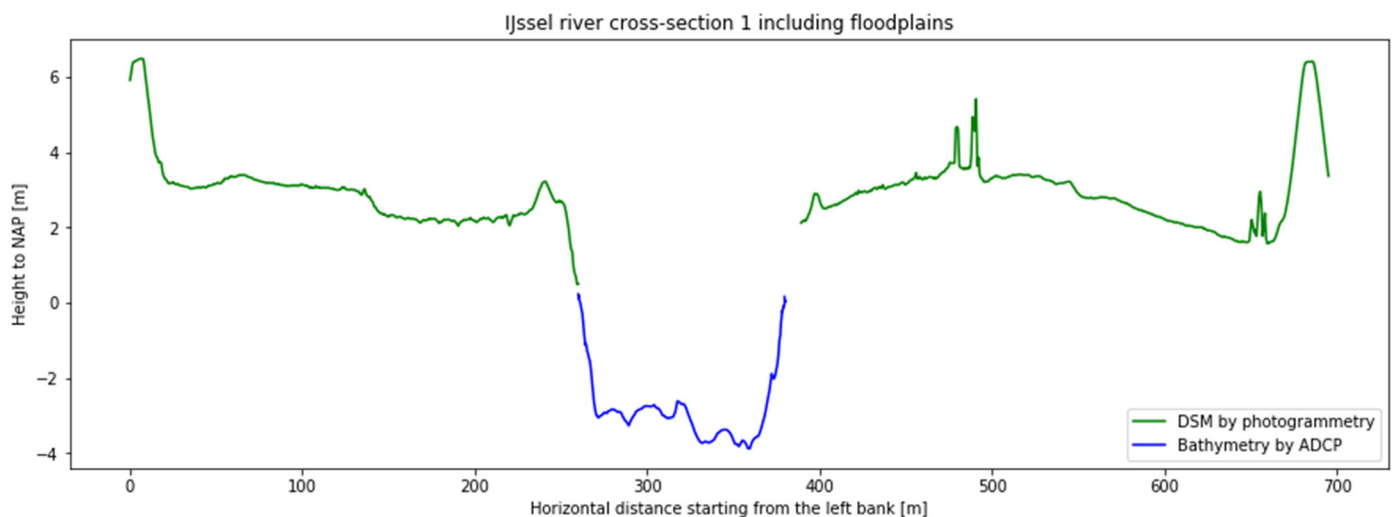


Figure 15 River cross-section at the study location

Between the west floodplain and the bathymetry, a small part of data is missing. This is due to the basalt blocks on the side of the river giving fluctuating heights. On the east side, there is a larger part missing.

This is due to the same basalt blocks and due to the different day of measuring the east sides floodplain than the bathymetry and west side. From the cross-section, it can be seen that the winter dikes on the far end of the floodplains are equal in height but the summer dikes next to the river are not. The land of the west floodplain is owned by a farmer who grows crops on the floodplain and is therefore probably better protected by a higher summer dike. The east side of the river's floodplain is owned by Staatsbosbeheer, which is the nature conservation organization of the Netherlands, containing only grass and some bushes. Therefore, the east-side is likely to have a lower need for protection by the summer dike. On the east side of the river's floodplain, there are peaks and an increased level found in the cross-section. The peaks correspond to the trees and the increased level corresponds to the elevated ground of a house that is built on the floodplain, which was shown in Figure 7.

The cross-section of the river was intended to be used to relate water level measurements of Rijkswaterstaat at Olst to the water level of the first fieldwork day. In this way, the water level difference can be used to relate water level with the width via the cross-section.

Unfortunately, the water level difference measured by the GNSS device and measured by Rijkswaterstaat do not correspond. The water level difference between both fieldwork days was 1.7 metre according to GNSS measurements. The water level difference at Olst between both fieldwork days, located approximately 11 kilometres upstream, measured by Rijkswaterstaat was 2.3 metre. The water level measuring location Wijhe, which is approximately four kilometres upstream of the study location, is missing water level data for the period of the second fieldwork day. Therefore, this station cannot be used to compare the water level differences. According to E. Kater (personal communication, January 21, 2019), advisor in river hydrology at Rijkswaterstaat, a rise of water level caused by wind influences, could reach up to regions upstream of Zwolle and thereby possibly the study location. During the first fieldwork day, there was a strong wind present. The strong wind could contribute to the varying water level differences between GNSS measurements and Rijkswaterstaat measurements. Olst is further upstream and therefore possibly less affected by the backwater effect caused by wind.

Three days before the fieldwork day, on the 4<sup>th</sup> of December, Sentinel-2 managed to capture the area of interest during cloud-free conditions. The measured water level near Wijhe on both days can be used to correct for the difference in acquisition time. The gauging station for water level near Wijhe is approximately four kilometres upstream of the study location without any tributaries in between. For this reason, the water level difference of both days at Wijhe is assumed to be the same as the difference in the study location. According to Rijkswaterstaat the water levels of the 4<sup>th</sup> and the 7<sup>th</sup> of December were the same, resulting in no water level difference and therefore no need for changes in the results for the 4<sup>th</sup> of December.

## 4.2. Current cutting-edge method for water classification

As a new method or technique needs to be compared to the current techniques, it was needed to obtain results of these methods. Two methods are applied to obtain results for the comparison of the new method. The first technique used is the Otsu thresholding and the second technique is supervised classification with the use of a training map. The training map is used as reference reflectance data of land and water areas.

### 4.2.1. Otsu thresholding results

Otsu thresholding, the first conventional method applied, searches for the threshold corresponding to the largest inter-class variance. The assumption of this technique is that the value distribution of the applied data is bimodal. Below, the results of Otsu thresholding can be found for the two commonly used water indices, NDWI and MDNWI but also for the pan sharpened MNDWI, noted as MNDWI<sub>10</sub>. Of each of the three indices, the results from the dates 04-12-18 and 15-02-19 are shown, to compare later with the ground truth data collection of the two fieldwork days. The GNSS measurement points of the corresponding day can also be found in the images as the black dots. Note that the 7<sup>th</sup> of December 2018, was infested by clouds during fieldwork, therefore the satellite image taken three days before is used. According to the water level data of Rijkswaterstaat, the water level of the 4<sup>th</sup> and the 7<sup>th</sup> of December were exactly the same at the measuring location in Wijhe, four kilometres upstream, and therefore the 4<sup>th</sup> of December is used to represent the first fieldwork day. In Figure 16 and Figure 17 the Otsu thresholding result of the NDWI can be seen for both days.

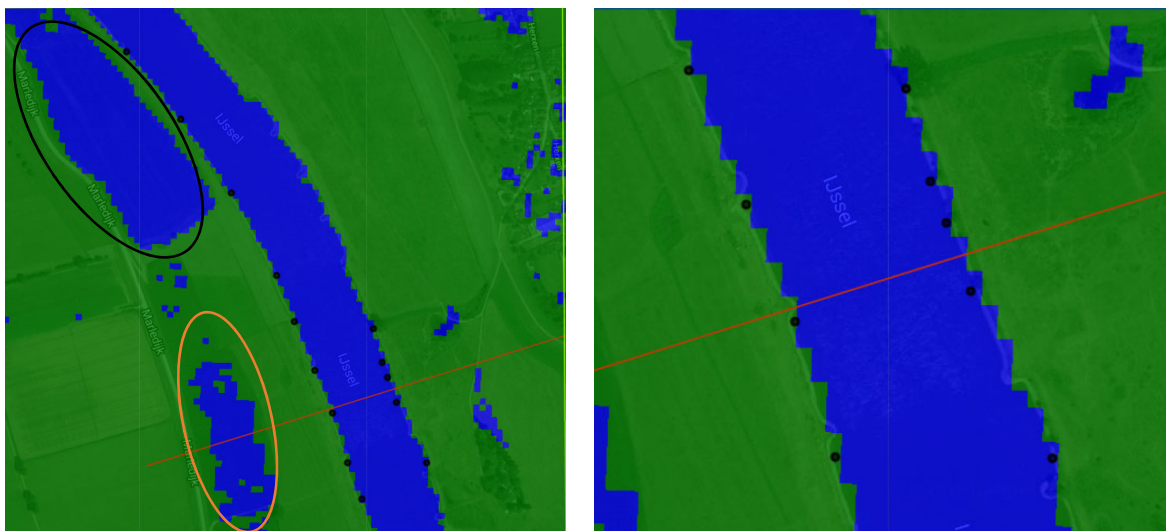


Figure 16 Otsu on NDWI, threshold: -0.143, Left: overview, Right: close-up \*04-12-18

In the results concerning NDWI, it can be noted that Otsu overestimates water. In the north-west part, marked with the black oval, it can be seen that the present bare-soil is classified as water on 04-12-18, as well as in the lower part of the floodplain, marked with an orange oval. The right image, the close-up, shows that the 10-metre resolution pixels do follow the measured GNSS points that indicate the waterline at these points. On 15-02-19 in Figure 17, the misclassification also occurs in the north-west, but in the lower part, marked in orange, the misclassification does not occur as it did on 04-12-18. While on 15-02-19 there was some water present, which is indicated by the GNSS points on the floodplains in Figure 17, this does not show in the Otsu results of the image.

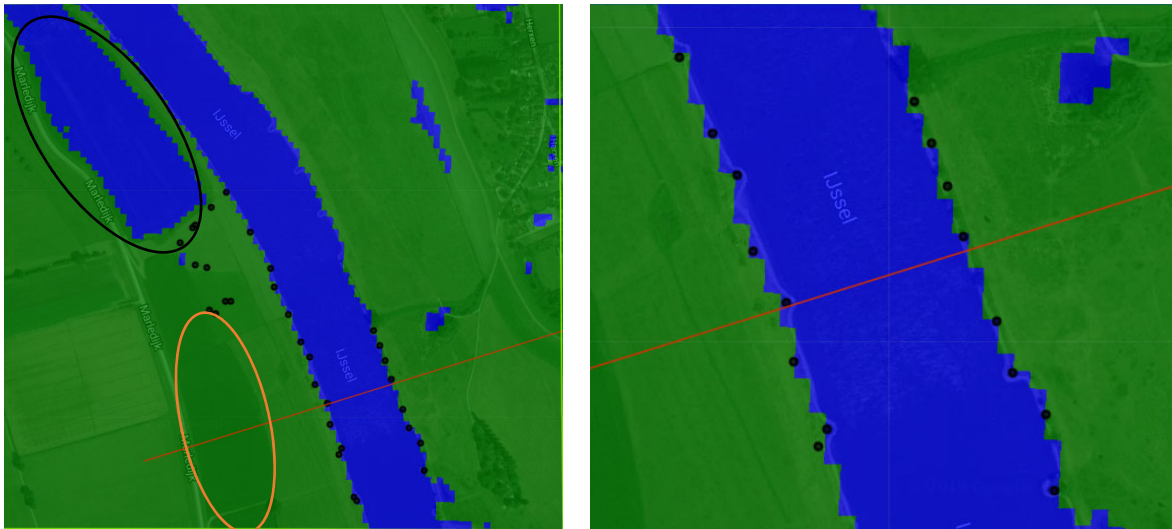


Figure 17 Otsu on NDWI, threshold: -0.111, Left: overview, Right: close-up \*15-02-19

The NDWI results confirm the literature (H. Xu 2006b), where it is stated that NDWI has difficulties with discriminating water and certain soil types. Both days show a threshold by Otsu for NDWI that varies around -0.11 to -0.14. Water mainly shows an NDWI higher than 0. When a minimum threshold is set, misclassification still occurs on the bare soil parts.

Figure 18 and Figure 19 show the MNDWI results of applying Otsu thresholding. It can be seen in the close-up that the MNDWI uses a SWIR1 band of 20-metre, resulting in coarser spatial detail. The water pixels follow the measurement points of the waterline but with the influence of the coarse 20-metre SWIR1 band in the MNDWI. Therefore the accuracy of the taken river-width highly depends on the location of measuring. This example can clearly be seen in the close-up view of Figure 18 for the location of the red line. It can be seen that the river-width would be underestimated when measured along the red line. This is also the case with the NDWI, but due to the high resolution of both bands in the index, it would result in a lower underestimation at some locations. The presence of land in the mixed pixels on the edge of the river seems to be dominant, causing no classified water pixels overlapping the ground truth points. The combination of the lower resolution of the SWIR1 band and the dominance of land values in the pixels result in a large river-width error.

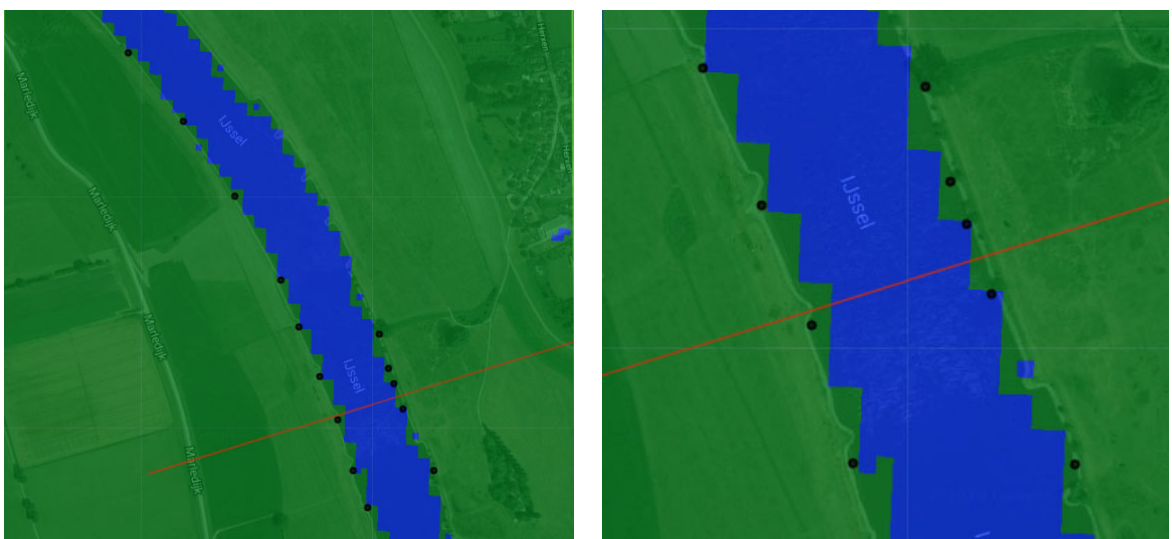


Figure 18 Otsu on MNDWI, threshold: 0.162, Left: overview, Right: close-up \*04-12-18

It can also be seen that the bare-soil is not misclassified as water with the MNDWI as was the case with NDWI. The lower resolution has the advantage that there is a better discriminative ability between land and water in the index used, the MNDWI. On 15-02-19, as stated earlier, there were flooded parts present on the floodplains. Some of these parts were measured by the GNSS device, other areas were identified by photos of the fieldwork day. The actual flooded parts are visualized by the yellow ovals in Figure 19. Where in the overview of the second fieldwork day a few pixels are recognized as water, the majority is not. The thresholds set by Otsu's method is for both days around 0.16.

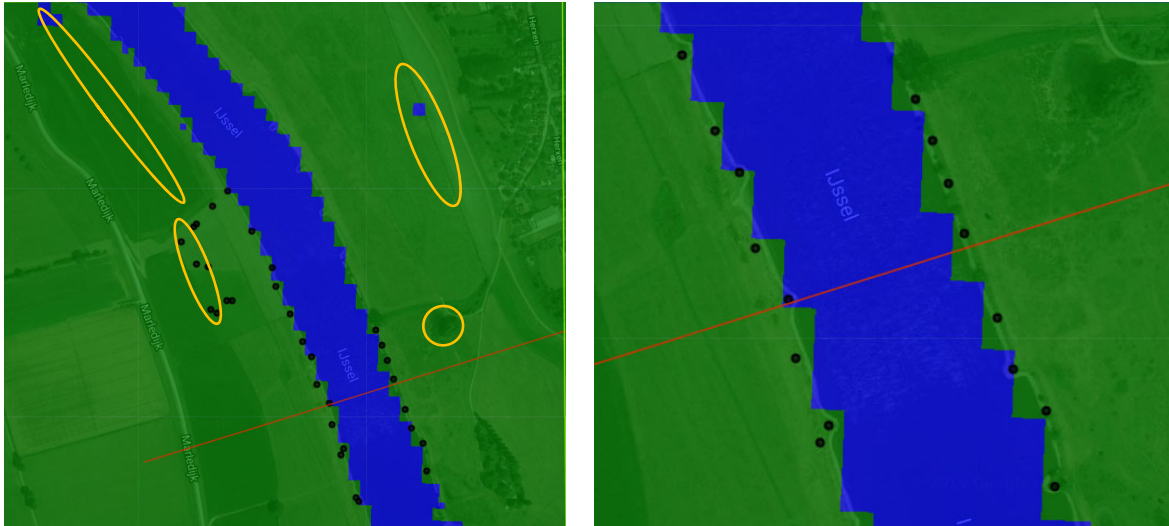


Figure 19 Otsu on MNDWI, threshold: 0.168, Left: overview, Right: close-up \*15-02-19

As last, the pan sharpened  $MNDWI_{10}$  is used to apply Otsu thresholding. Unfortunately, by using the IHS pan-sharpening method in combination with the NIR band as described in 3.5 of the methodology, the unwanted influence of the NIR bands is transferred. This can be seen in Figure 20, where again the bare-soil is classified as water. However, the spatial resolution is improved as can be seen in the close-up image.

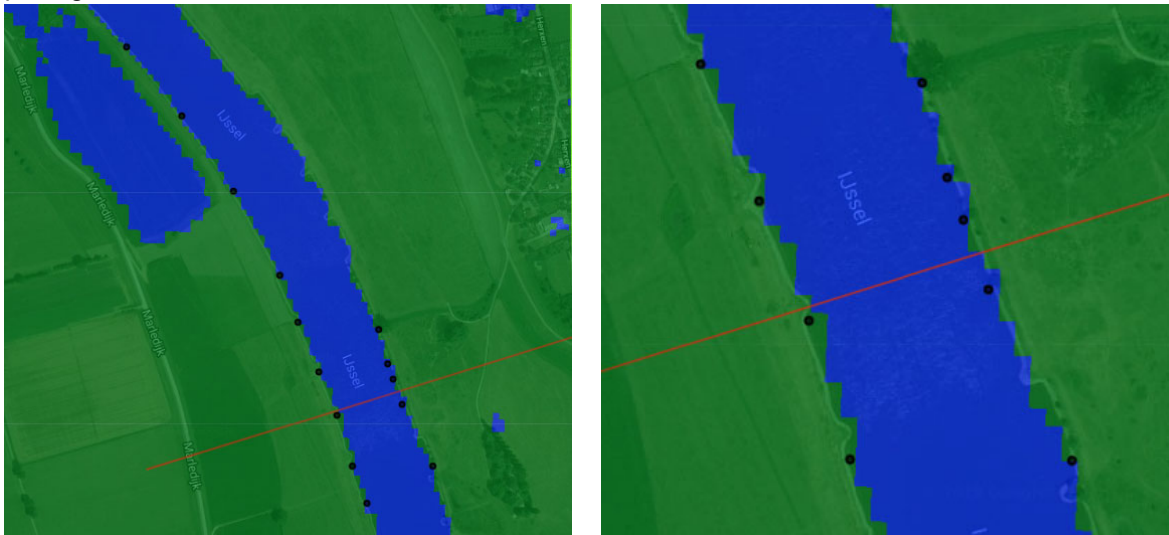


Figure 20 Otsu on  $MNDWI_{10}$ , threshold: 0.160, Left: overview, Right: close-up \*04-12-18

The Otsu thresholding with  $MNDWI_{10}$  looks visually better on the second fieldwork day. The inundated floodplain areas are shown without a lot of misclassification, as can be seen in Figure 21, again marked with yellow ovals. The better recognition of the inundated areas could be because the division of land and water plus inundated areas is more equal. Without the inundated areas, there is only deep water with some hard to classify edges and land present. Therefore, dry land patches that have values

between most water and land values, like bare-soil, can be earlier classified as water via this bimodal thresholding technique. The threshold set is around the same value as with the normal MNDWI Otsu threshold, indicating that the pixel values are changed during pan sharpening. This can be noted by the same threshold resulting in different output.

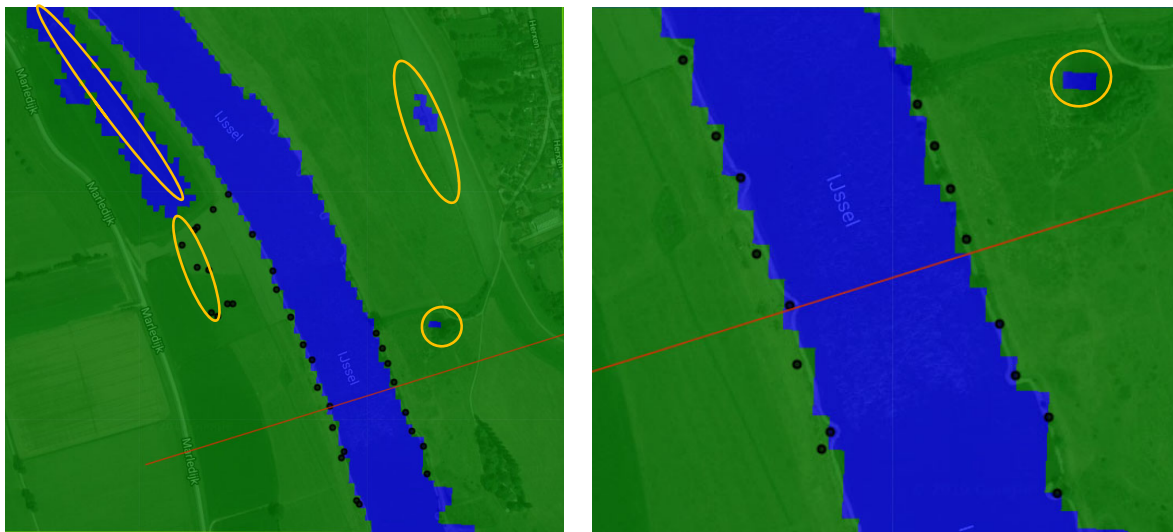


Figure 21 Otsu on MNDWI<sub>10</sub>, threshold: 0.168, Left: overview, Right: close-up \*15-02-19

#### 4.2.2. Supervised classification with the use of a training map

The second conventional method, applied for comparison reasons, is by the use of a training map originating from fieldwork data. This method is also applied on both fieldwork days as has been done for the Otsu thresholding results. The first fieldwork day is again represented by the satellite image three days before on the 4th of December. The results of the training map classification can be seen in Figure 22 and Figure 23. The first fieldwork day does not show misclassification parts in the overview of Figure 22. The close-up of the same figure shows that the classification is on the preservative side. The accuracy of the classification is 95.8%. The accuracy is calculated by using the corresponding confusion matrix and dividing for each class the correct classified pixels over the total pixels of that class in the training map. The resulting confusion matrix of this classification incorrectly classified 13 out of 139 water pixels as land and 0 pixels out of 175 land pixels as water. The accuracy and confusion matrix is based on the training map. This confusion matrix shows that the classification is on the preservative side due to the zero incorrectly classified land pixels.

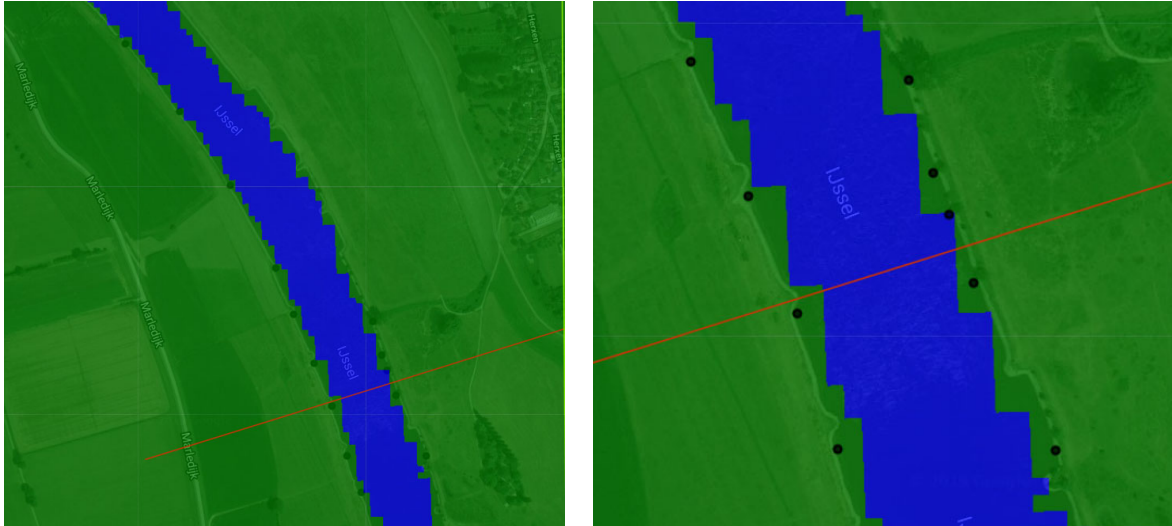


Figure 22 Supervised training map classification result, Left: overview, Right: close-up \*04-12-18

The second fieldwork day has an accuracy of 94.9%. In this case, the classification seems to recognize the inundated areas for a large part. On this image, there are 8 out of 155 water pixels incorrectly classified as land and 6 out of 119 land pixels incorrect classified as water. It can be seen in both Figure 23 and the confusion matrix that there is less underestimation. The measured inundation areas by the GNSS are again not recognized as water, indicating that shallow patches of water contain strong land reflectance patterns present in its signal.

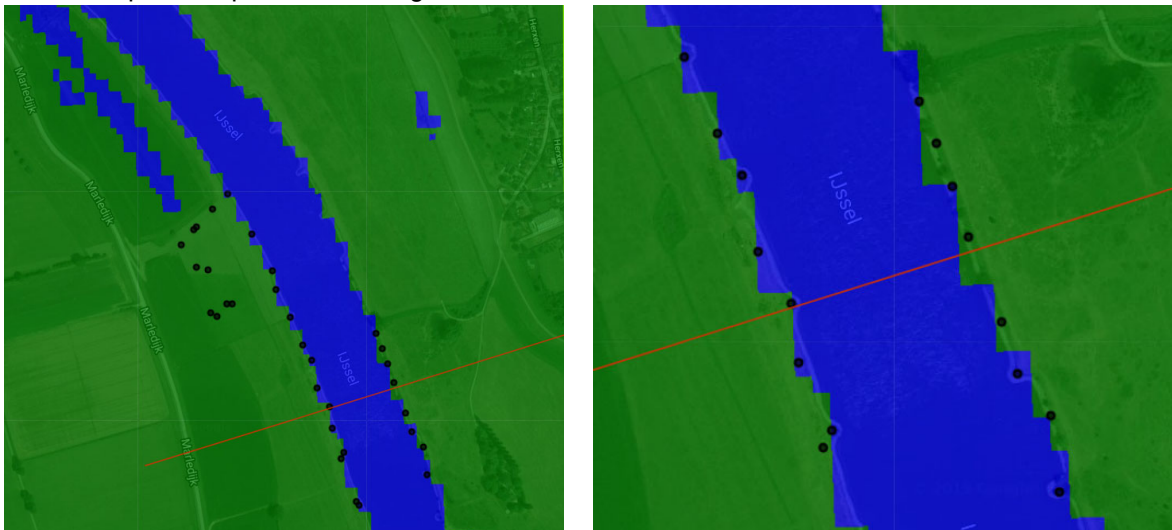


Figure 23 Supervised training map classification result, Left: overview, Right: close-up \*15-02-19

### 4.3. Discriminating bands between water and land

In subchapter 4.2.1, it is seen that at the study location of the IJssel, misclassification occurs when using the NDWI. NDWI is an index that is commonly used to map water, while it can happen that this index is not the only index suitable for your location. To make an approach of analysing the study area, possible discriminating bands need to be found. First, some information about the two classes, water and land, need to be known to be able to identify the discriminating ability.

Table 4, Table 5 and Table 6 show the mean, min and max values for each available band of the used satellite missions. The values are sampled over water and land areas based on fieldwork data. This enables the possibility to compare the mean land and the mean water values of each band. The min and max sample values are useful to see the deviation of the land and water values from its mean. This could show an overlap of values of a band within the two classes for example, which can cause confusion during classification and therefore leads to misclassification.

Table 4 Mean values of water and land for each band

Water	Land
Mean	Mean
Blue: 0.111	Blue: 0.111
Red: 0.087	Red: 0.079
Green: 0.094	Green: 0.098
NIR: 0.049	NIR: 0.212
SWIR1: 0.014	SWIR1: 0.156
SWIR2: 0.007	SWIR2: 0.096

Table 5 Min values of water and land for each band

Water	Land
Min	Min
Blue: 0.108	Blue: 0.104
Red: 0.083	Red: 0.064
Green: 0.091	Green: 0.092
NIR: 0.046	NIR: 0.123
SWIR1: 0.011	SWIR1: 0.110
SWIR2: 0.006	SWIR2: 0.058

Table 6 Max values of water and land for each band

Water	Land
Max	Max
Blue: 0.114	Blue: 0.115
Red: 0.089	Red: 0.089
Green: 0.096	Green: 0.108
NIR: 0.056	NIR: 0.389
SWIR1: 0.040	SWIR1: 0.192
SWIR2: 0.020	SWIR2: 0.105

From the mean values of the blue band, it can be seen that these are equal for both land and water. The min and max values are close to each other too, resulting in no sign of a discriminating ability. The red band, however, shows that the mean, min and max values of water are close to each other and within the land class there is more spread in min and max values. The mean value of the red band is also different for land and water. The green band shows something similar, except that the mean value for land and water is more close to each other than with the red band. For the bands NIR, SWIR1 and SWIR2 however, the differences are larger. Between the mean values, there is a more noticeable difference than with the red and green bands. This indicates that these bands have a larger discriminating ability.

For the study area, 20 years of sampled pixel data is presented for each band separately in the figures below. The mean values for water and land found in Table 4 are plotted as vertical lines in the histograms of each band to show the location in the histogram.

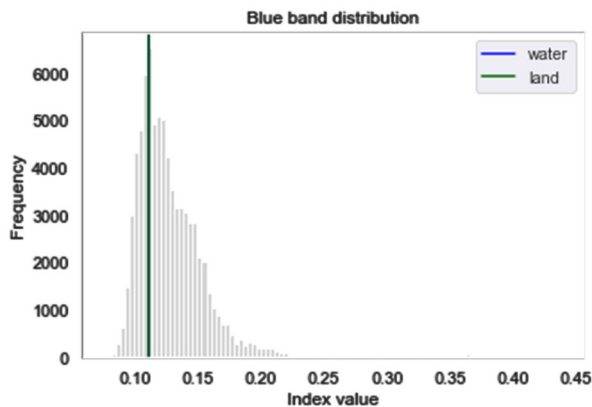


Figure 24 Blue band value distribution with mean land and water values

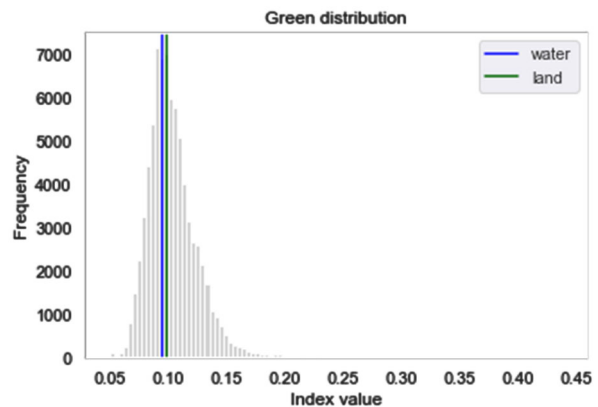


Figure 25 Green band value distribution with mean land and water values

Figure 24 shows that the water and land mean values are at the same location, which indicates that there is no discriminative ability for water and land present. The histogram does show a spread in values. This spread in values should, therefore, be due to other variations like built-up land and roads, for example, which are not sampled for value comparisons. The green band, visualized in Figure 25, shows a small difference in mean values between land and water. The green band is commonly used in water indices and can be found in the NDWI but also the MNDWI. The larger spread in its distribution can be, as mentioned for the blue band, due to other influences besides the differences between land and water. A strong discriminative ability is sensed when the water and land classes have a high inter-class variance. The higher the inter-class variance, the easier it is to distinguish the classes.

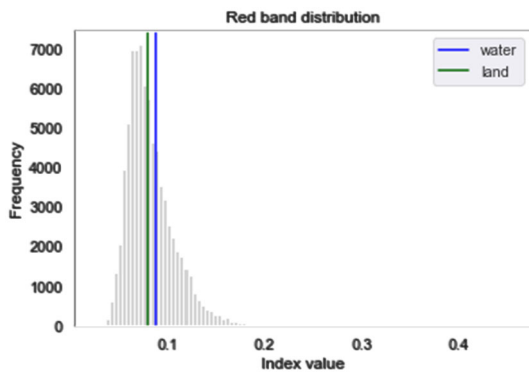


Figure 26 Red band value distribution with mean land and water values

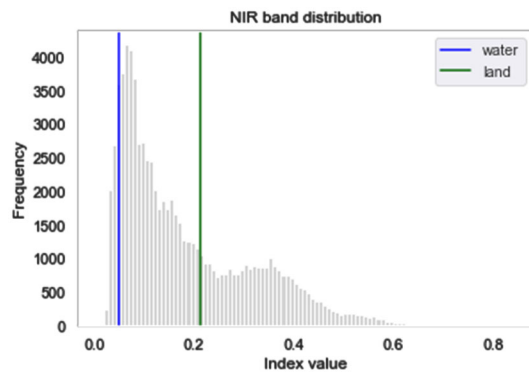


Figure 27 NIR band value distribution with mean land and water values

The red band distribution, in Figure 26, shows that the mean values of water and land within this band are close but they are further apart than within the green band. This shows that this band could also be considered as a candidate for further combinations besides the commonly used green band. The NIR band, in Figure 27, shows a bimodal distribution indicating a large discriminating ability. The mean value of land for the NIR band lies more in the middle of the two peaks than on the second peak what would be expected in a bimodal distribution. This could also explain the confusion in this study area with the bare-soil areas.

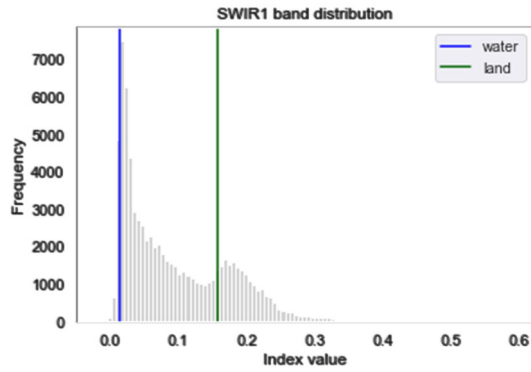


Figure 28 SWIR1 band value distribution with mean land and water values

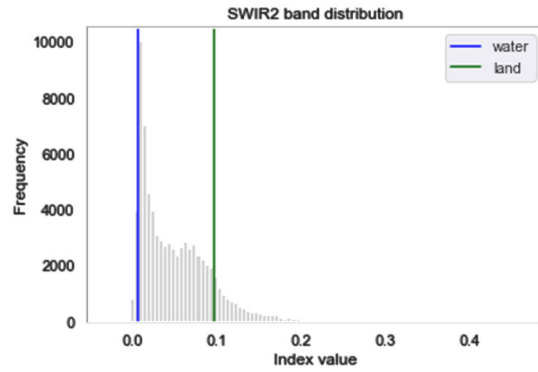


Figure 29 SWIR2 band value distribution with mean land and water values

The last two bands are the SWIR1 and the SWIR2 bands that can be seen in Figure 28 and Figure 29, respectively. SWIR1 shows again, like the NIR band, a clear bimodal distribution. The mean values of water and land do lie on the different peaks, hence this could explain the better inter-class variance between water and land in this band compared to the NIR band. SWIR2 shows a more compact distribution where the two peaks of the bimodal distribution are closer to each other. The mean values of both classes do show a difference indicating the discriminating abilities of the band.

After analysing the distributions of each band separately, the bands that show potentially discriminating behaviour are used to create combinations for custom normalized difference indices. Of the six analysed bands, five of them showed signs of discriminating abilities. The blue band was the only band that did not show any sign of different values between land and water and is therefore not used in the next subchapter.

#### 4.4. Discriminating band combinations for custom normalized difference water indices

The results of the discriminating band combination density analysis can be seen below for the different band combinations. The mean values of each band for water and land that are presented in Table 4 are plotted in the same scatterplot to indicate the mean areas of both class values. The same 20 years of data from section 4.3 is used in this part but now all the combinations of the five separate bands are plotted as a scatterplot for analysis. The band values can be found on the x and y-axis of the scatterplots. Because there are a lot of data points plotted, it is hard to see an inter-class variance between classes in the image. Therefore, a kernel density estimation is used as is explained in subchapter 3.4 of the methodology. Each point has a bivariate kernel density estimation, where overlapping kernels are added and shown as coloured contour lines. The summed densities can be found at the scale on the right of each figure indicated by colour.

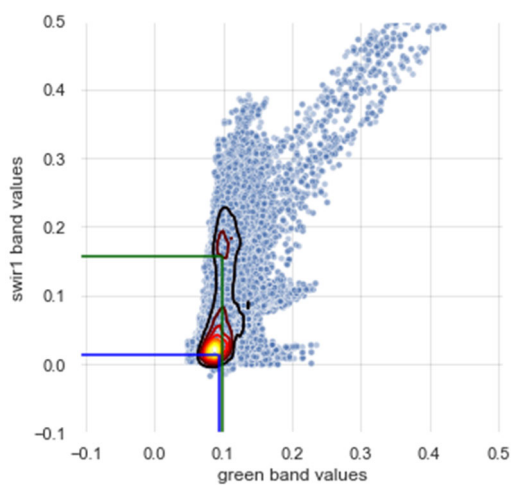


Figure 30 Scatterplot combined with density plot, green band vs SWIR1 band

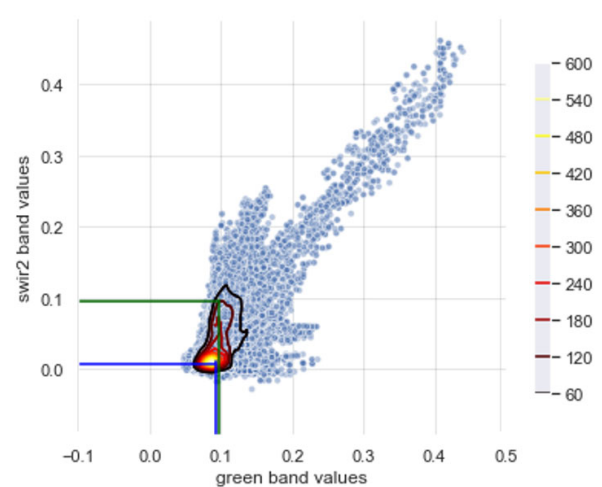


Figure 31 Scatterplot combined with density plot, green band vs SWIR2 band

In Figure 30, the green vs SWIR1 band are plotted, this combination is also known as the MNDWI. In the scatterplot, a clear interclass-variance can be seen between water and land. It also shows that the land values are more spread out. The spreading of the land values is not remarkable when considering that multiple land types are combined as one land class in this thesis. Green vs SWIR2 band scatterplot, in Figure 31, also shows a separation between water and land. Within this combination, the different values are closer to each other compared to the green and SWIR1 combination.

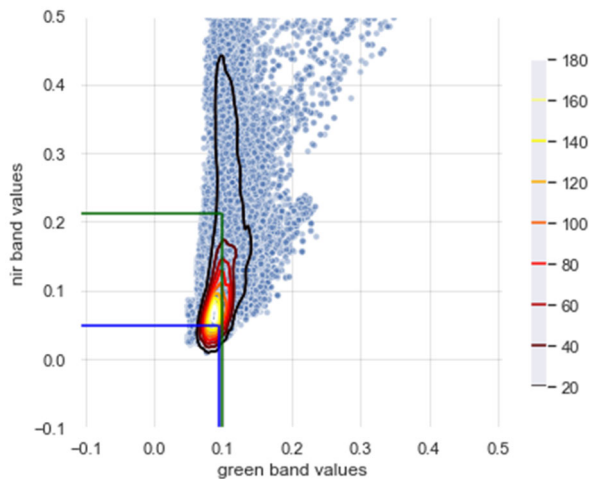


Figure 32 Scatterplot combined with density plot, green band vs NIR band

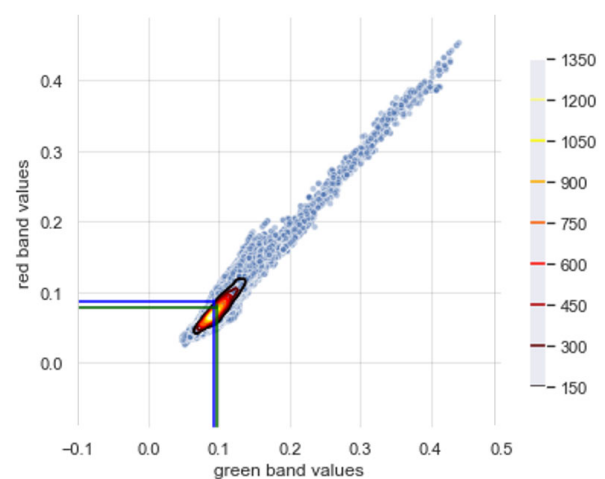


Figure 33 Scatterplot combined with density plot, green band vs red band

Figure 32, shows the green vs NIR band, which is also known as the NDWI. It can be seen in this figure that there is a separation between water and land but the land values are more distributed. This means that the intra-class variance of the land class in this combination is on the high side. There is discriminating ability present but due to the high intra-class variance misclassification is likely to occur. The green vs red band scatterplot, in Figure 33, shows that there is no discriminating ability present between the two bands for water and land. Both classes are present at the same location in the plot, indicating a low discriminative ability and therefore will not be used as a combination in the further analyses.

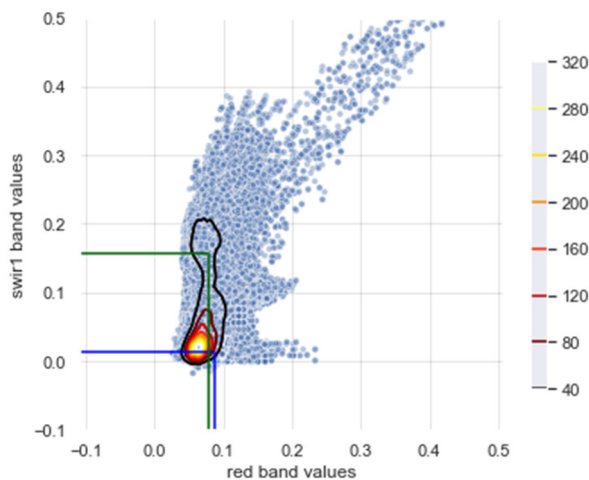


Figure 34 Scatterplot combined with density plot, red band vs SWIR1 band

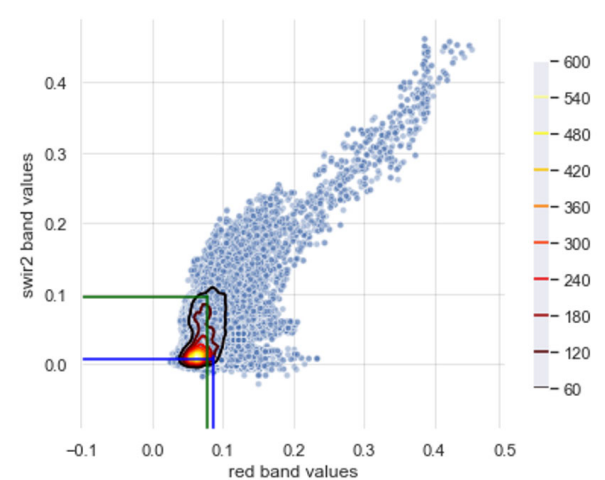


Figure 35 Scatterplot combined with density plot, red band vs SWIR2 band

The red vs SWIR1 band scatterplot, in Figure 34, also shows a separation between the two classes. This combination of bands shows a less dense land class compared to the green vs SWIR1 band combination. The red vs SWIR2 band scatterplot, of Figure 35, shows like green with SWIR2 that the two classes are closer to each other compared to the combinations with SWIR1. Despite the classes being more close to each other, still, a separating ability can be found.

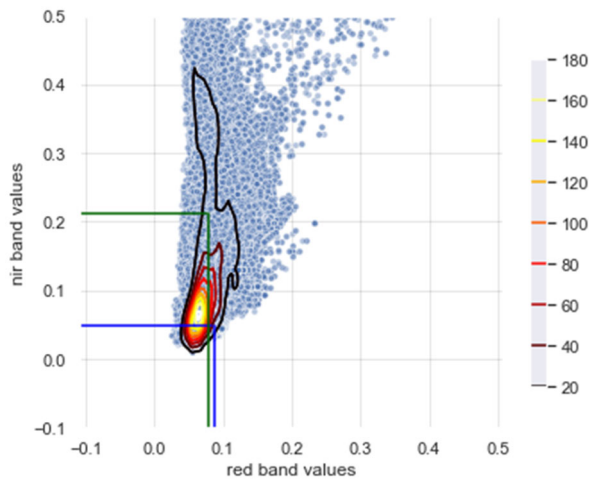


Figure 36 Scatterplot combined with density plot, red band vs NIR band

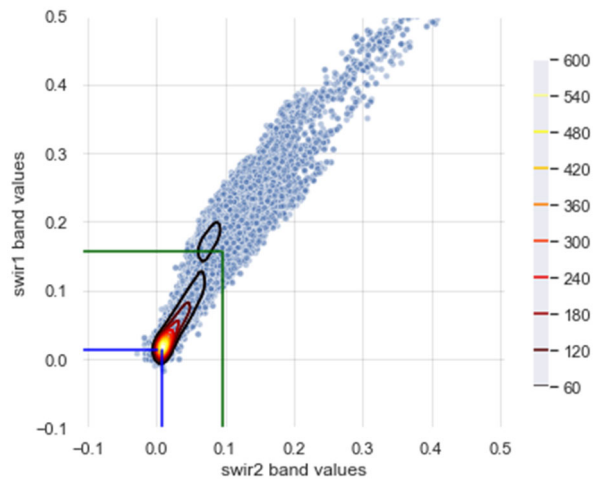


Figure 37 Scatterplot combined with density plot, SWIR2 band vs SWIR1 band

Figure 36, shows again that a combination with the NIR band contains a lot of spread within the land class. The mean of the land class values does not lie in the middle of the upper-density contour line in the figure. The mean values of the land and water classes are still showing discriminating behaviour. It is worth noting that, when two classes both increase with the same rate in value from band x to band y, they will be close to each other in value when converted to a normalized difference index. This is not the case for the combinations above, except for SWIR2 vs SWIR1 in Figure 37. This combination does show discriminating behaviour but within more or less the same increment rate.

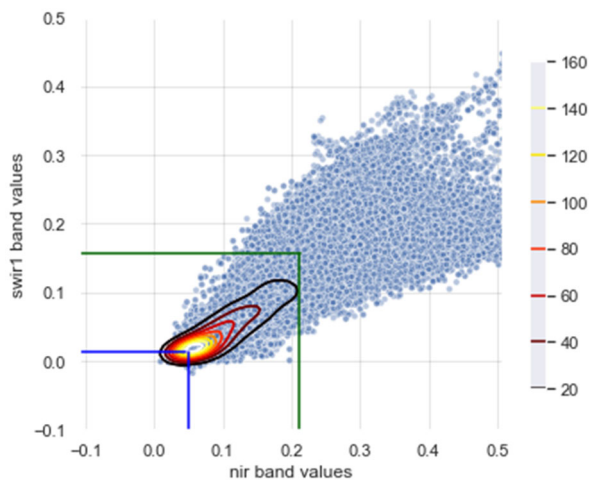


Figure 38 Scatterplot combined with density plot, NIR band vs SWIR1 band

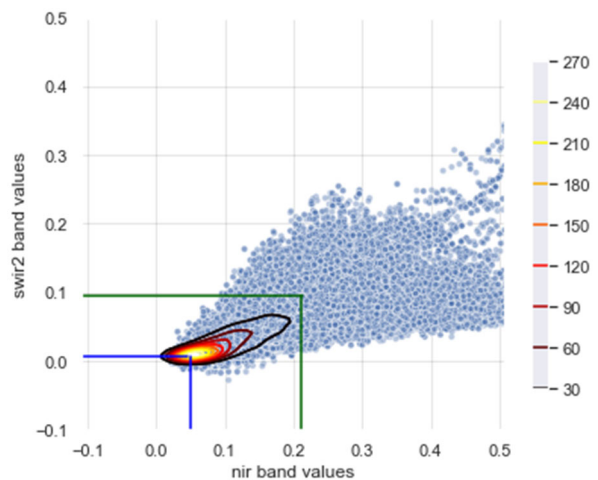


Figure 39 Scatterplot combined with density plot, NIR band vs SWIR2 band

The latter is the same for the combination of NIR vs SWIR1 and NIR vs SWIR2, as can be seen in Figure 38 and Figure 39. Therefore, the three last combinations are not suitable to be used as a normalized difference index for water classification purposes.

The potential band combinations used for the indices can be found in Table 7. In the table, the combination number, the bands in the combination and the index name can be found. The combination numbers will be used further in subchapter 4.6.2 to indicate the combined indices via Bayes theorem. The three combinations that can be made with NIR, SWIR1, and SWIR2 as indices were not discriminating enough to perform accurate edge detection. The slope from SWIR1 to SWIR2 was to identical for the water and land classes, which caused similar results for both classes in the index. This was also the case for NIR vs SWIR1 and NIR vs SWIR2. Therefore, as mentioned above, these three indices are discarded.

Table 7 Band combinations for discriminating indices

Band combination number	Band 1	Band 2	Index name
0	Green	NIR	NDWI
1	Green	SWIR1	MNDWI
2	Green	SWIR1- Pan-sharpened	MNDWI_10
3	Red	SWIR2	ND_rd_sw2
4	Red	SWIR1	ND_rd_sw1
5	Red	NIR	ND_rd_nr
6	Green	SWIR2	ND_gr_sw2

#### 4.5. Image enhancements to improve water classification abilities

The results of the pan-sharpening applied to the SWIR1 band are already shown in Figure 20 and Figure 21 of subchapter 4.2.1. The spatial resolution of the SWIR1 band is improved to 10-metre. However, the spectral resolution inherited influences of the NIR band, which are not wanted.

The 'bicubic' resampling is used on the bands used for the NDWI, MNDWI and the pan-sharpened MNDWI to obtain these in 1-metre resolution, instead of their original resolution of 10 and 20-metres. The resampled indices are classified by Otsu's method. The influences of the NIR band in the NDWI results in Figure 40 and Figure 41, is still present, but the waterline follows the GNSS measurements better than with the original resolution. The resampled image of the NDWI also seems to follow the waterline in more detail where even the outline of the groynes is visible.

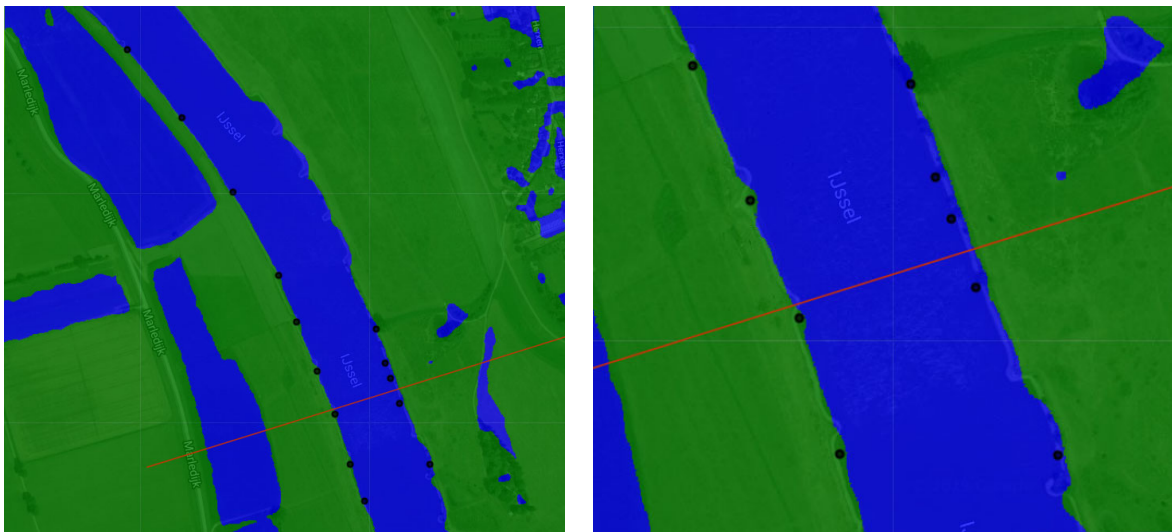


Figure 40 Otsu on NDWI 1m resolution, threshold: -0.169, Left: overview, Right: close-up  
\*04-12-18

The inundated areas on the floodplains indicated by the black points and the yellow ovals in Figure 41 are on this resolution not observed by the classification. This indicates that resampling does not improve the classification of mixed pixels when there is no water around as is the case on the river's edge.

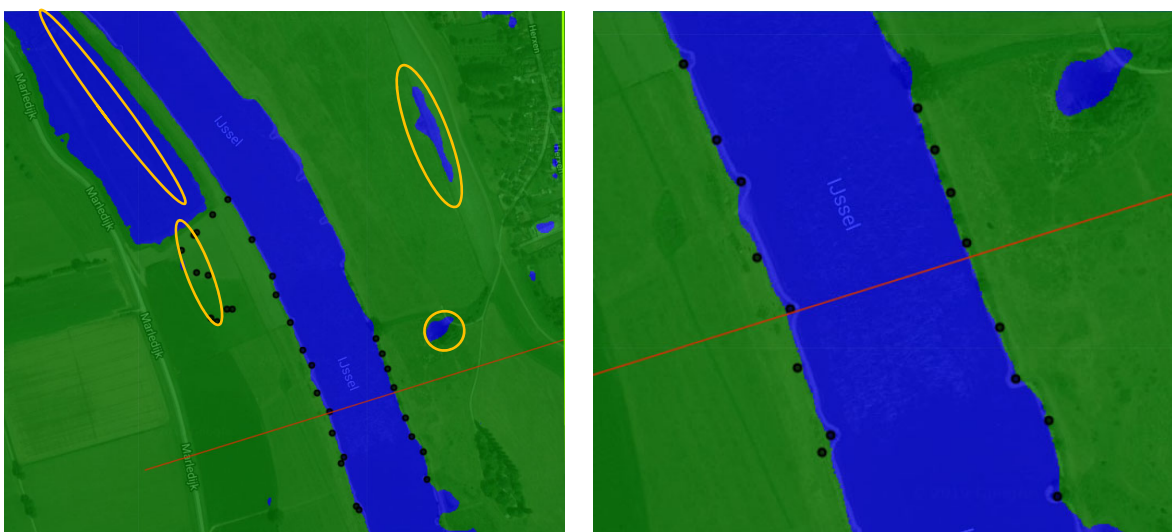


Figure 41 Otsu on NDWI 1m resolution, threshold: -0.112, Left: overview, Right: close-up  
\*15-02-19

The results of the 1-metre resolution MNDWI after applying Otsu seems to underestimate the water classification as can be seen in the close-up of Figure 42 of 04-12-18. The second fieldwork day also shows an underestimation of the water classification in the close-up of Figure 43.

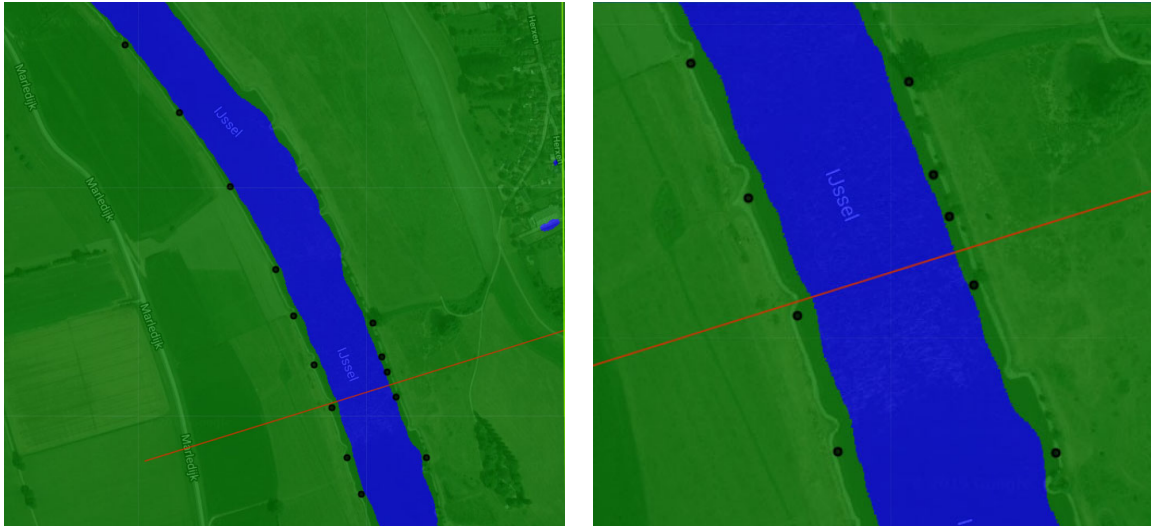


Figure 42 Otsu on MNDWI 1m resolution, threshold: 0.172, Left: overview, Right: close-up \*04-12-18

On both fieldwork days, the Otsu results, of the 1-metres resolution MNDWI, show that the misclassification is not present. The inundated areas, on the other hand, are not classified as water. This shows that resampling to a higher resolution does make the river's edge more smooth and possibly a better fit, but it does not introduce more spectral detail in terms of recognizing different parts as water.

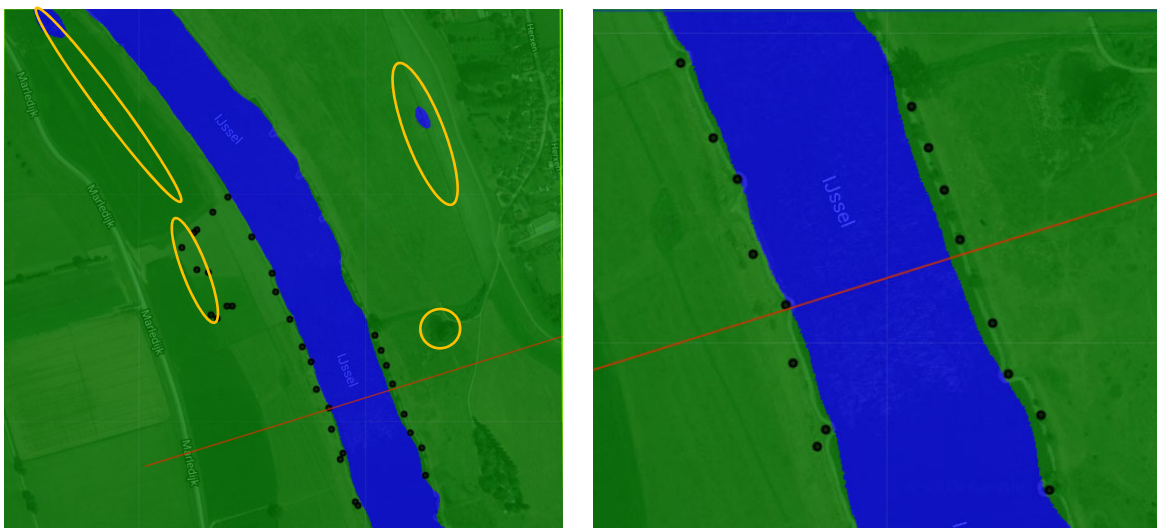


Figure 43 Otsu on MNDWI 1m resolution, threshold: 0.184, Left: overview, Right: close-up \*15-02-19

The same counts for the pan sharpened MNDWI, the same sort of results can be seen, in Figure 44 and Figure 45. Just like the case with the original resolution results of Figure 20 and Figure 21, only now with a smoother river edge. No improvements are seen compared to the original resolution Otsu results on misclassification, or recognition of inundated areas. The second day of fieldwork also shows in the higher resampled resolution the inundated area on the bare soil.

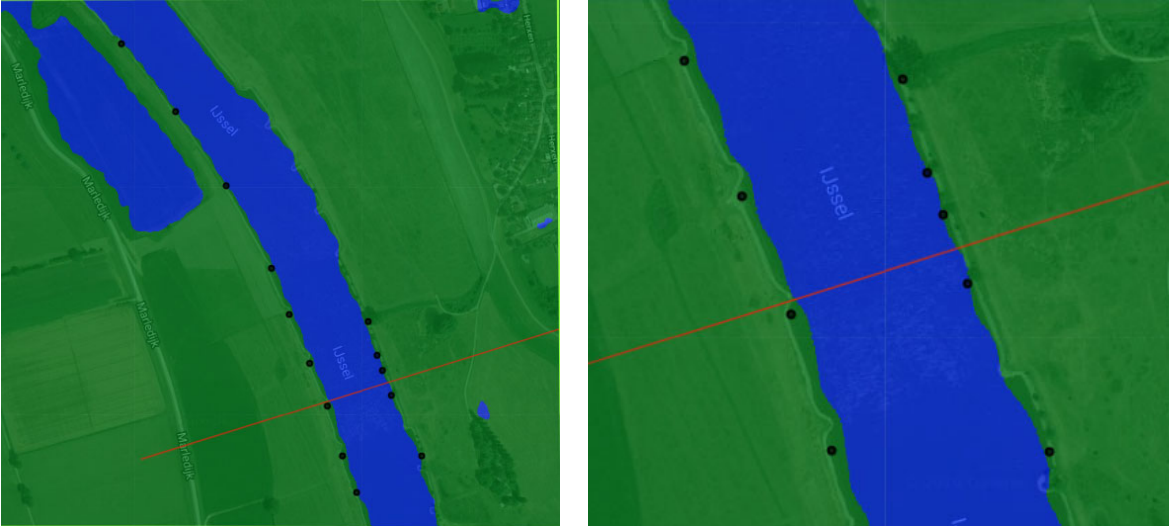


Figure 44 Otsu on MNDWI<sub>10</sub> 1m resolution, threshold: 0.152, Left: overview, Right: close-up \*04-12-18

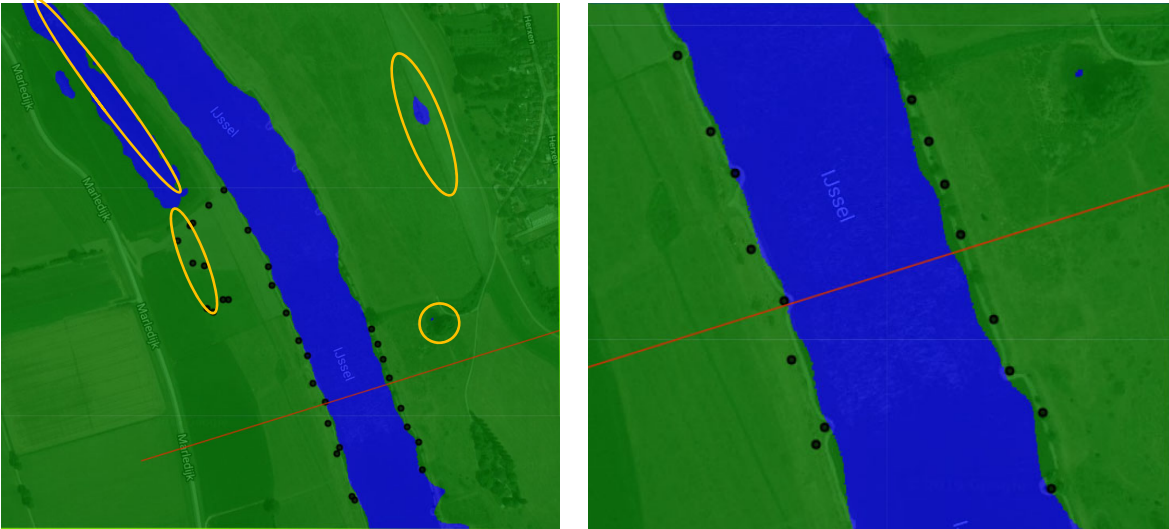


Figure 45 Otsu on MNDWI<sub>10</sub> 1m resolution, threshold: 0.175, Left: overview, Right: close-up \*15-02-19

The 1-metre resolution bands of the NDWI, MNDWI and the MNDWI<sub>10</sub> will be used in the next step, where edge detection is performed.

## 4.6. Combined normalized difference indices to improve classification

This subchapter uses the results of the discriminating band combinations found in subchapter 4.4. The new combinations will be converted into normalized difference indices as indicated in Table 7. From these indices, probability bands will be made in subchapter 4.6.1 and these probability bands will be combined in subchapter 4.6.2 via Bayes theorem.

### 4.6.1. Obtaining index probabilities

The custom indices are constructed in its original resolution but also on 1-metre resolution scale, besides the NDWI, MNDWI and the MNDWI<sub>10</sub>. The resampled 1-metre resolution scale was used to perform Canny edge detection, that finds the slopes above the set thresholds in the index values indicating a transition of class. This transition mainly happens in the study area at the river's edge when the right slope threshold is set. For now, the threshold for the different indices is manually found. This edge was thereafter used to sample pixel values of the original resolution index band. The distribution of these sampled edge values of each index was then used to construct a cumulative distribution function curve, a CDF curve. The CDF curve of the different indices can be seen in Figure 46 and Figure 47 for dates 04-12-18 and 15-02-18, respectively.

Every index now has its own CDF curve that is used to assign probabilities to each pixel for being water. All pixel values within the CDF get a probability between 0 and 1. The pixel values lower than the CDF get a probability of 0 and the pixel values above the CDF get a probability of 1 assigned. The CDF curves do not align on the same location due to different reflectance values of water and land between the indices. Water and land have varying reflectance values over the frequency domain and therefore also different values of the band values measured by the satellite.

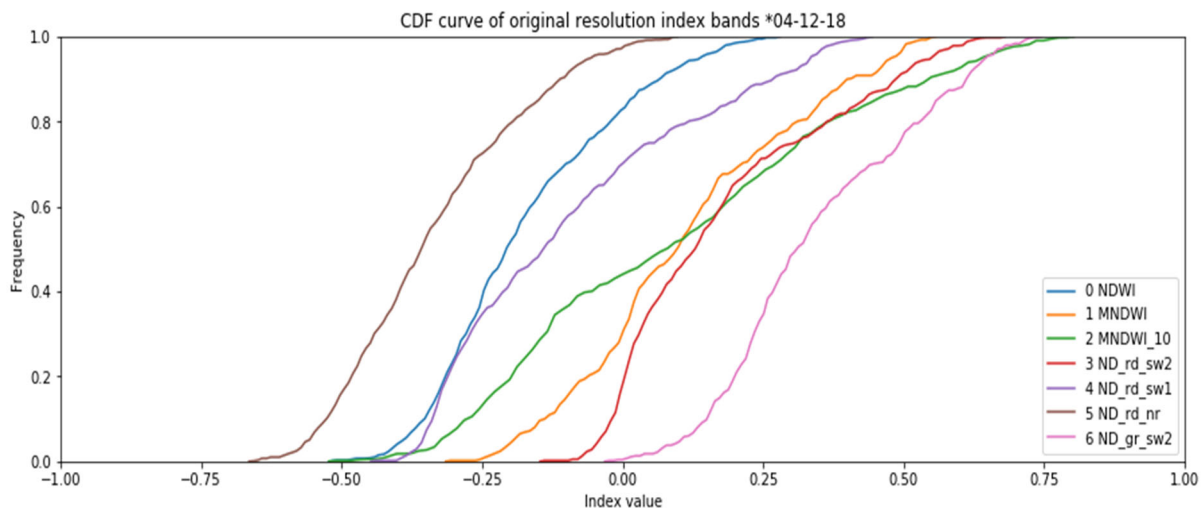


Figure 46 Combined CDF curves of index value samples on Canny edge \*04-12-18 \*sw1 and sw2 are bands instead in indices

The CDF curves of both days are not exactly the same. This can be due to different pixel values and different atmospheric conditions resulting in slightly different values. Different positions of the sampled pixels on the edge could also cause a difference in CDF curves between the two days. Index number 3 and 6 of both days seem to be different on the land side of the CDF curves, the bottom of the curve. Index number 5 and 6 of both days seem to be different on the water side of the CDF curves, the top of the curve.

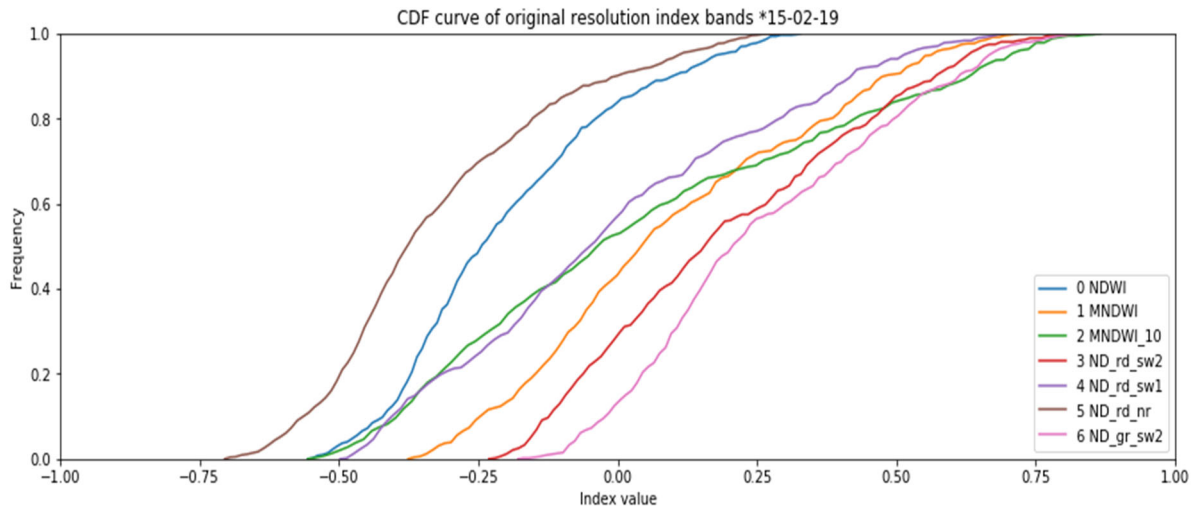


Figure 47 Combined CDF curves of index value samples on Canny edge \*15-02-19 \*sw1 and sw2 are bands instead in indices

Figure 48, shows the custom index with the green and SWIR2 band as probability band, which is the best performing index found in the next section, section 4.7.1.2. The colours in the figure show a visualization of the probabilities in the study area. Indicated by the black circle, there is an uncertainty of classifying pixels in the middle of the river as water. This turns out to be a large transport ship in the image. The probability above the bare-soil does not show a value close to zero for being water like the grass patches around it, but the probability of the bare-soil is much lower than that of actual water. The inundated areas at the GNSS points, indicated by the black dots are now also indicating that there is a chance of water present. Also, the inundated areas based on taken photos during the fieldwork, indicated by the white ovals, show an increase in probability for being water.

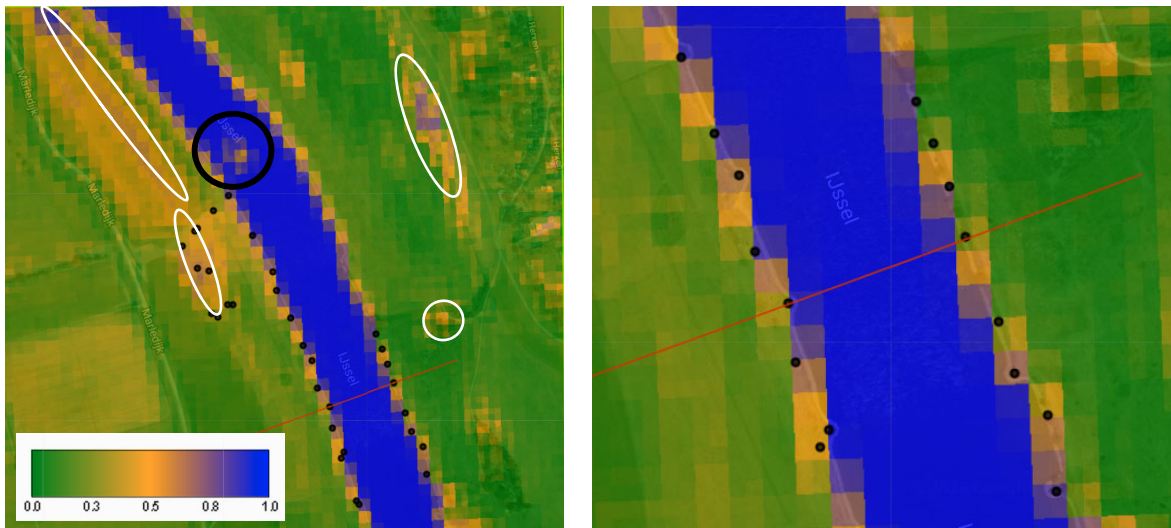


Figure 48 Probability band of the custom index: ND\_gr\_sw2, Left: overview, Right: close-up \*15-02-19

## 4.6.2. Bayes theorem for combining index probabilities

With the obtained probability bands of each index, combinations are made to perform Bayes theorem of updating probabilities. The index combinations for the application of Bayes theorem can be found in Table 8. The Bayes combinations are constructed without a combination containing twice the same band. This means NDWI, which uses the green and NIR band, cannot be combined MNDWI. This is because MNDWI also makes use of the green band. An exception is made for the last two combinations to see if combining more indices result in more robust results. Note, statistically this is not correct to combine depended information with each other via Bayes theorem, because this means data is used multiple times to obtain new probabilities (Triola 2010).

Table 8 Bayes index combinations used for analysis

Index combination name	Index 1	Index 2	Index 3
Bays0-3	NDWI	ND_rd_sw2	-
Bays0-4	NDWI	ND_rd_sw1	-
Bays1-3	MNDWI	ND_rd_sw2	-
Bays1-5	MNDWI	ND_rd_nr	-
Bays4-6	ND_rd_sw1	ND_gr_sw2	-
Bays5-6	ND_rd_nr	ND_gr_sw2	-
Bays0-3-4	NDWI	ND_rd_sw2	ND_rd_sw1
Bays1-5-6	MNDWI	ND_rd_nr	ND_gr_sw2

Figure 49, shows the combined probability band Bayes 4-6. Bayes 4-6, as can be seen in Table 8, combines the red and SWIR1 bands (ND\_rd\_sw1 index) together with the green and SWIR2 bands (ND\_gr\_sw2 index) for the second fieldwork day. This combination of two indices is the best performing index for both days found in the next section, section 4.7.1.3, according to the ROC analysis. Indicated by the black circle in the figure, there is a smaller uncertainty of classifying pixels in the middle of the river as water than seen in the single probability index of Figure 48. This turned out to be a large transport ship as mentioned in the previous section, which is filtered out in the index combination due to the lower deviating signal of one the indices, the ND\_rd\_sw1. The probabilities seen in Figure 49, where the inundated areas are marked with the white ovals, show signs of probabilities indicating indeed present water. Above the bare-soil region in the most North-Western part, where a part was inundated on the second fieldwork day, the probability values show a higher value for being water. The combined index band seems to show a better distinction between bare-soil and inundated areas. The other visualized probability indices and combinations can be found in the appendix, in section [Probability bands visualized](#).

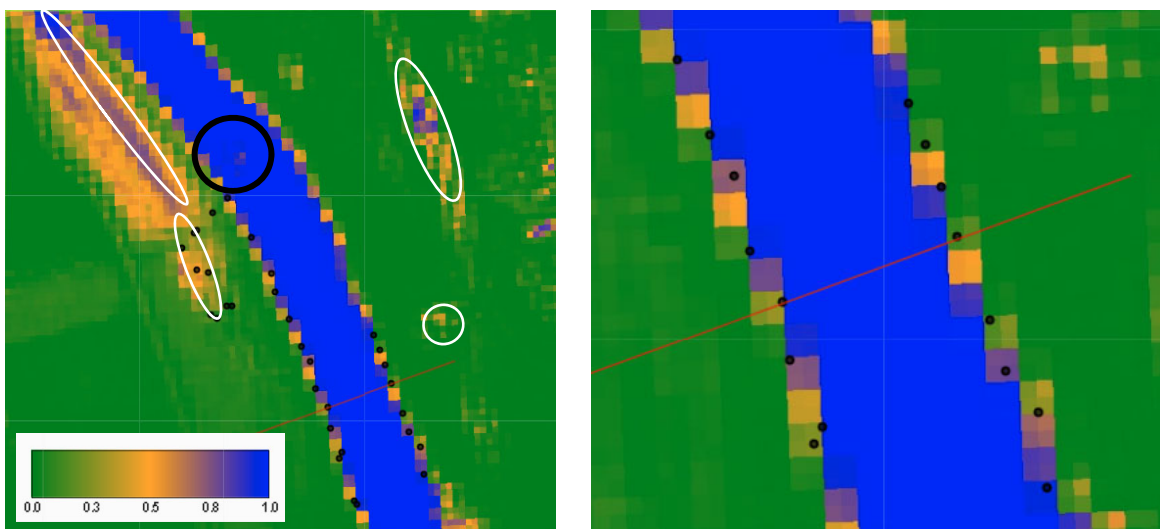


Figure 49 Probability band of combined indices: Bayes 4-6, Left: overview, Right: close-up \*15-02-19

## 4.7. Quality assessment of methods with in-situ measurements

The results of the site-specific indices, probability bands of the indices and combinations of the probability bands by Bayes need to be assessed. This assessment is done by checking the water classification ability with a Receiver Operating Characteristics curve, a ROC curve.

### 4.7.1. ROC analysis

The ROC analysis contains comparisons of curves between the site-specific indices, the constructed probability bands of these site-specific indices but also combinations of these probability bands. The Area Under the Curve, AUC in short, indicates how well a discriminating separation can be made within the used band or index.

The True Positive Rate and the False Positive Rate are based on water and land areas of the fieldwork data. Where, for example, one of these fieldwork based water areas overlap partly a pixel, as happens on the river edges, this pixel will be seen as water, while it is partly water. The ROC curves look at the performance of classification of water and not of land, meaning that the curves show how well water is classified by the different indices. When ROC curves are used on the probability index bands, this indirectly also shows the classification performance of land. This is because the probability relation between land and water is known, which is:

$$P_{land} = 1 - P_{water} \quad (14)$$

#### 4.7.1.1. ROC analysis of the site-specific index values

The analysis of the site-specific indices are made for both fieldwork days and can be seen in Figure 50 and Figure 51. The indices used for these two figures are constructed to see how well the indices perform on their own, before making probability bands of the indices. The AUC values that can be found in the legend of the figures are relatively close to each other. The used indices are already filtered on discriminating behaviour and therefore all indices used score relatively high on the AUC. To show more detail in the variation of the curves at the upper-left corner, the ROC graph starts from 0.7 on the y-axis. The legend shows the index number of each normalized difference index, which will be used to refer the indices used in the Bayesian combinations.

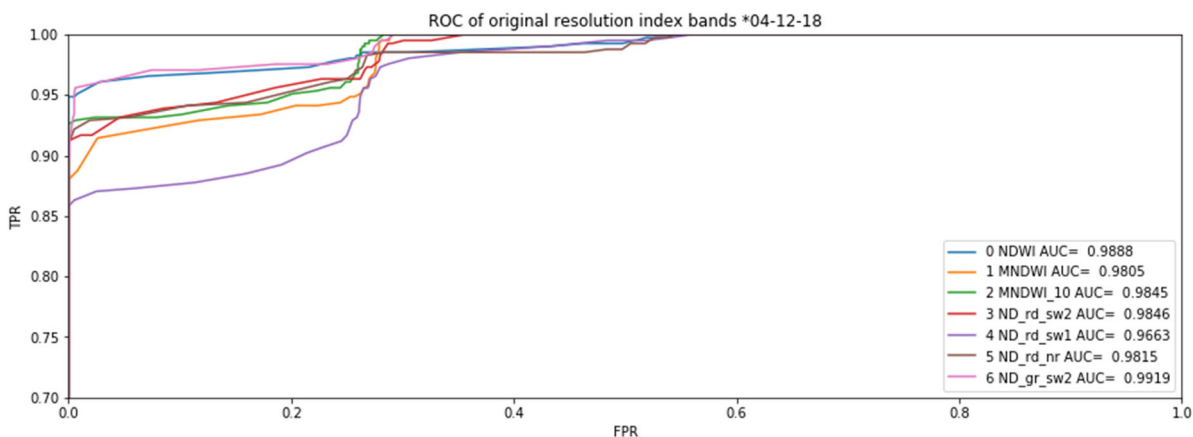


Figure 50 ROC curve of index band values \*04-12-18

Index 4 is the worst performing of the first day. On the second day, index 4 is not the worst performing, but is still one of the less performing indices, indicating that the combination red and SWIR1 is less

performing compared to the others. It is also noticeable that index 0, NDWI, performs rather well on the first fieldwork day but belongs to the less performing indices for the second day. The decrease in performance of the NDWI is due to the addition of the inundated areas on the floodplain that was measured by the GNSS device. When these inundated areas are not taken into account for the ROC analysis, the NDWI performs as one of the better indices for the second fieldwork day, as is the case for the first fieldwork day, where no inundated areas were present. Index 5 shows the same change in performance as the NDWI, which both contain the NIR band, possibly indicating that the NIR band is not well capable of classifying inundated areas.

In Figure 50 and Figure 51, the combinations with the SWIR2 band perform well, whether it is in combination with the green band or the red band. For both fieldwork days, index 6, the combination of the green band and the SWIR2 band has the highest AUC. Index 3, red and SWIR2 combination, has the third highest AUC and the second highest AUC on the first and second fieldwork day, respectively. This could be explained by the small intra-class variance of the two separated classes in these combinations, seen in Figure 31 and Figure 35, of section 4.4. The red band performs good, while normally only green is used, this could potentially be a good option to use for index combinations via Bayes theorem. Especially, because in this theorem it is statistically not allowed to use data that is depended on partly the same information, in this case, bands. When analysing the hyperspectral reflectance signal of Figure 2, it can be seen that green vegetation has on average a slightly higher reflectance signal in the green domain than the red domain. The dry bare soil reflectance signal, found in the same figure, has higher reflectance in the red domain than in the green domain. Our study location contains large patches of bare soil but also of green grass, and therefore the red band used in the indices is likely to be performing rather well. When the study location would contain only green grass, the advantage of using only the green band would most likely come to the surface.

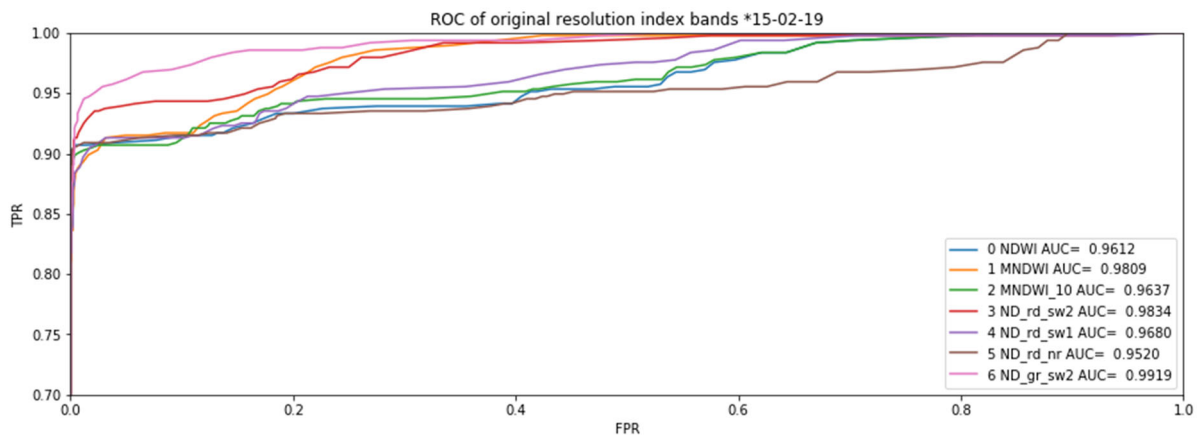


Figure 51 ROC curve of index band values \*15-02-19

The indices of the first fieldwork day show a shorter graph with more or less a jump to a TPR of 1. This jump is around the threshold value where the bare soil is seen as water, after analysing the values. When reviewing the band combinations containing either SWIR1 or SWIR2, the bare soil has a higher probability of being water than the vegetation areas, but do contain lower values than the water values. For the band combinations containing the NIR band, the probability values of the bare-soil look a lot more like the water values. The spatial difference can be seen in the visualized probability bands of the appendix, section [Probability bands visualized](#). From the moment the FPR increases from 0, parts of the bare soil start to be misclassified as water. This jump in the first fieldwork day ROC curves also happens with index 3, around a TPR of 0.95 to 1. The index threshold values that belong to these TPR's decrease from 0.206 to 0.115. Around the index threshold value of 0.206, most bare soil is misclassified, but not all water pixels are classified as water yet, TPR is still lower than 1. Therefore, this jump looks to be the contribution of the mixed pixels, that are assigned as water located on the border of the study area derived water areas, as mentioned in the introduction of this subchapter, subchapter 4.7.1. These

mixed pixels on the border of the river have a lower water signal and a present land signal and therefore need a threshold farther away than the typical water threshold for such an index. The second fieldwork day results show a more substantial spread in the graph of the ROC curves. The spread could be caused by the inundated areas on the floodplain, resulting in more confusion for classification.

#### 4.7.1.2. ROC analysis on the probability bands of the site-specific indices

The constructed probability bands are analysed on classification performance in Figure 52 and Figure 53 below, in the form of a ROC curve. A similar pattern is found as with the ROC curves of the site-specific index band values. The performance by the AUC is also similar between the index values and the index probability values. This means that according to the results of this method by using a ROC curve, the discriminative abilities stayed more or less the same after conversion to probability bands. For date 04-12-18, the jump in the ROC curve to a TPR rate of 1 is less sudden than with the index values of section 4.7.1.1. This jump could be smoothed by the use of the CDF curves obtained by the edge data, to obtain probabilities. The band combination ND\_gr\_sw2 performs best for both days as can be seen in Figure 52 and Figure 53. The second best performing index for both days is index ND\_rd\_sw2. These combinations of the red or green band with the SWIR2 band showed in Figure 31 and Figure 35 of section 4.4, two density classes close to each other. The two density classes, indicating water and land, were close to each other but both with low intra-class variance, indicating a low spread of values of the classes in the scatter plot. This low spread of values could result in the output seen in Figure 52 and Figure 53 for these two indices performing rather well without a lot of misclassification.

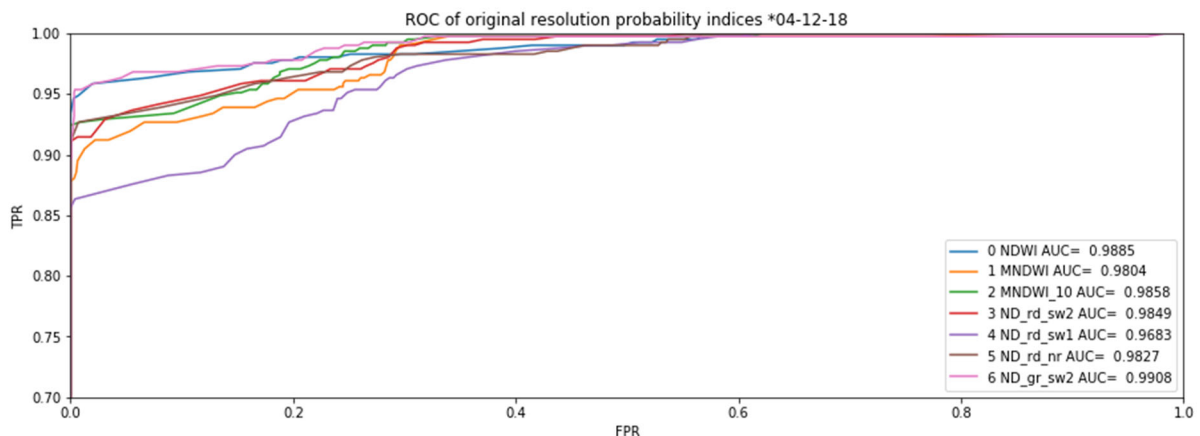


Figure 52 ROC curve of index probability band values \*04-12-18

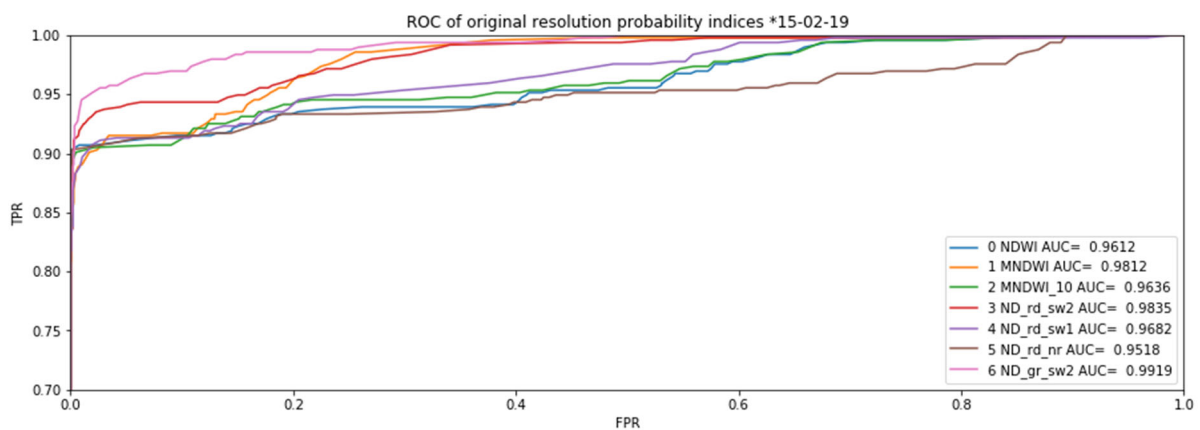


Figure 53 ROC curve of index probability band values \*15-02-19

### 4.7.1.3. ROC analysis on the combined probability bands with Bayes theorem

By combining the probability bands of the site-specific indices, more information of multiple bands can be used for the classification. The ROC curves of the Bayes combinations are less diffuse than the ROC curves of the single probability bands. This could be explained by the fact that better and worse performing bands are also combined and thereby reaching values more close to other combinations. The combined probability bands show again a shorter transition to the maximum TPR rate of 1 for the first fieldwork day. The Bayes combinations including index 0, NDWI, show a good performance for the first fieldwork day but a less performing ability on the second fieldwork day. This again shows that the influence of the NIR band for classifying the inundated areas has an impact on the results. First, it was only seen that the NIR band had a lower discriminative ability on bare-soil in the study location, but now it seems that inundated areas have an effect on the performance of classification by indices that contain the NIR band.

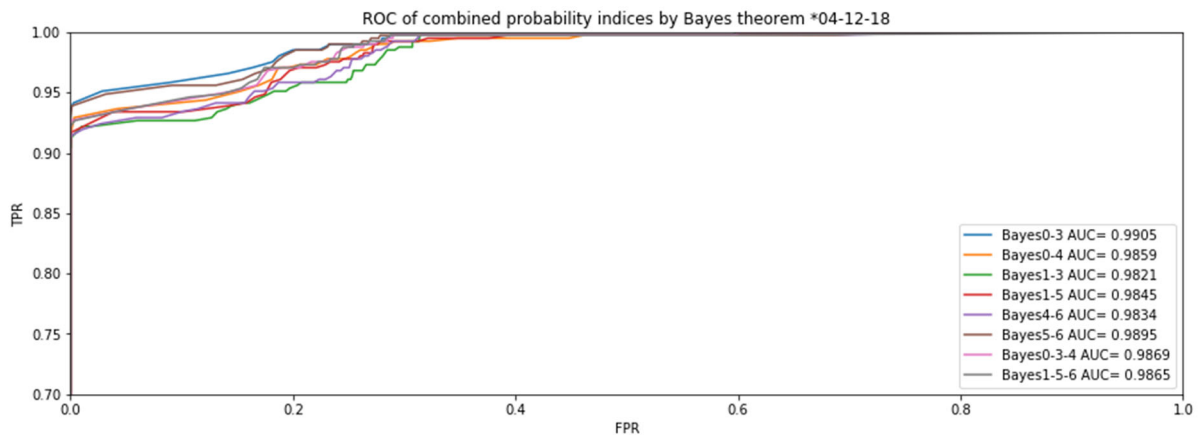


Figure 54 ROC curve of combined index probability values by Bayes theorem \*04-12-18

The two combinations that contain the green and red bands together with the SWIR1 and SWIR2 bands, noted as Bayes 1-3 and Bayes 4-6, show both a consistent performance for both days. Indicating that this combination delivers stable results between the two fieldwork days. The ROC curves for the second day of Figure 55, are less dense. It can be seen that there are two groups of combinations, where Bayes4-6 and Bayes1-3 seem to have better abilities to classify inundated areas as water. Bayes1-5-6 shows to be located in the middle of the ROC curves. This shows that an index with the NIR band combined with two indices containing SWIR bands shows that influences of less functioning indices are averaged out by combining multiple indices. Yet when inundated soil areas can be present it seems to be best, not to use a combination that contains the NIR band.

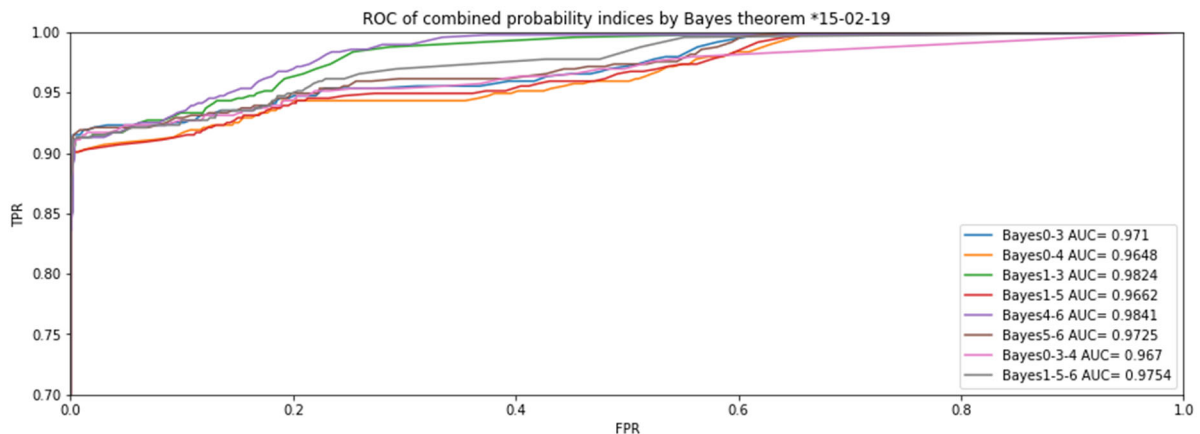


Figure 55 ROC curve of combined index probability values by Bayes theorem \*15-02-19

### 4.7.2. Water fraction pixel analysis

Besides the ROC analysis on the different probability bands and Bayes combinations, an analysis is done on the water fraction of a pixel and the probability bands and Bayes combination bands. The two best performing results of the probability bands, the best performing of the ROC analysis and the two best performing Bayes combinations are plotted below. The plots of the four remaining probability bands and the remaining six Bayes combinations can be found in the appendix under section [Water fraction relation images](#). As mentioned in the methodology section under section 3.7.2, the measured waterline points by the GNSS device are used to sample water fraction values and probability index values of the underlying pixel. The GNSS points are used to avoid interpolations errors of a constructed waterline between the GNSS waterline measurement points. The sampling of the west side and the east side of the river are plotted separately. This is done to see if there is a variation between the two riversides. Secondly, the two different fieldwork days are also plotted separately in the figure. Finally, a linear trendline is plotted based on the combined results of both riversides and both days. To obtain for each side and each day separately a trendline, more waterline measurement points were needed. The R-squared coefficient is also given with each plot, to give an indication of the predictability of the data by linearization. If a probability index seems to show a relation between the water fraction of a pixel and the probability of that pixel being water, the index and relation can be used to dissect mixed pixels into land and water. The dissected pixels on the riversides can, therefore, be used to obtain a more detailed river-width not only on pixel-basis but also on a sub-pixel basis.

The results of the pan-sharpened MNDWI sampled points at the GNSS locations in Figure 56 show a few outliers from the trendline, but the majority of the points are close to the trendline. This index scores the highest on the R-squared compared to the other probability indices, indicating that this index has a lower variance in the data to be interpreted as linear. Based on the results presented in Figure 56, the use of the pan-sharpened MNDWI seems to be suitable for sub-pixel analysis and possible pixel dissection. The different riversides and fieldwork days seem to perform equally around the trendline, without one side of the river or a fieldwork day showing different results. Therefore, the choice to obtain a trendline from the combined data is grounded. The results of the water fraction analysis for MNDWI\_10 seem to show a relationship and will, therefore, be used in the next section for river-width analysis. For the original MNDWI, however, there is a low relationship found. This shows that the pan-sharpening introduces positive influences for the water fraction relationship.

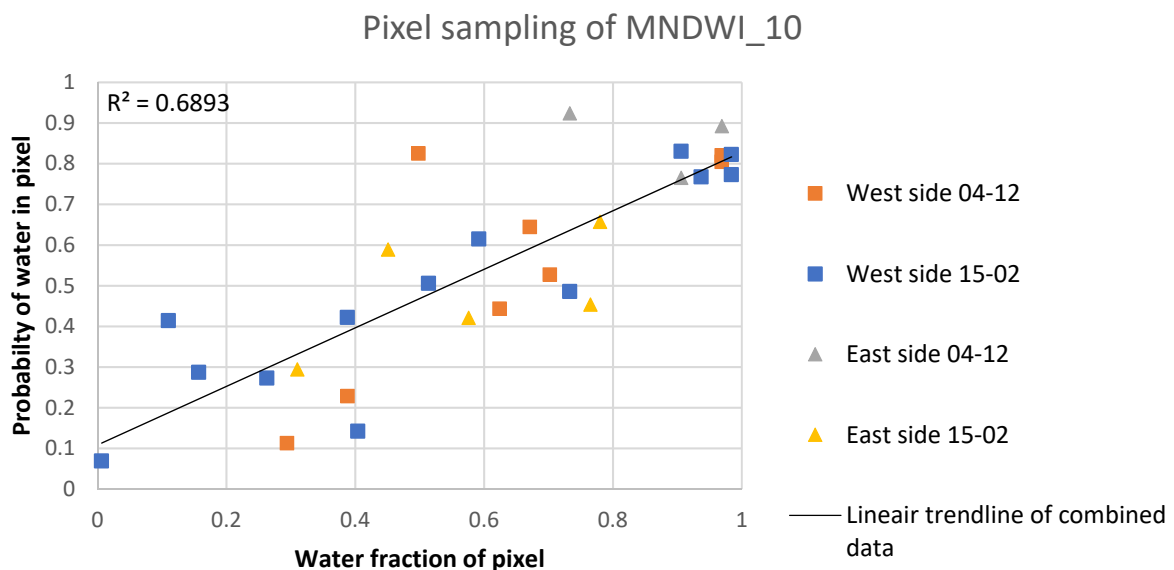


Figure 56 Pixel sampling of MNDWI\_10, for the GNSS waterline points

The sub-pixel analysis of the NDWI probability band shows the second best performance in terms of R-squared results of the probability bands. The data is overall performing well except for a part of the data on the west side of the 4<sup>th</sup> of December. The other points are located close to each other and seem to be more linearly distributed. The four deviating west side GNSS points on the 4<sup>th</sup> of December, marked with an orange oval in Figure 57, are measured directly next to groynes in the river. The extents of the groynes were not mapped correctly on the 4<sup>th</sup> of December and therefore it could be the case that the water fraction of the underlying pixels is overestimated. A shift of these four points under the curve to the left, a lower water fraction, would result in a better outcome. Therefore the NDWI does seem to be potentially a suitable probability band for sub-pixel analysis. The four mentioned deviating points are in all plots possibly shifted. However, the R-squared value is considerably lower than that of the pan-sharpened MNDWI and will therefore not be used for pixel dissection in the next section.

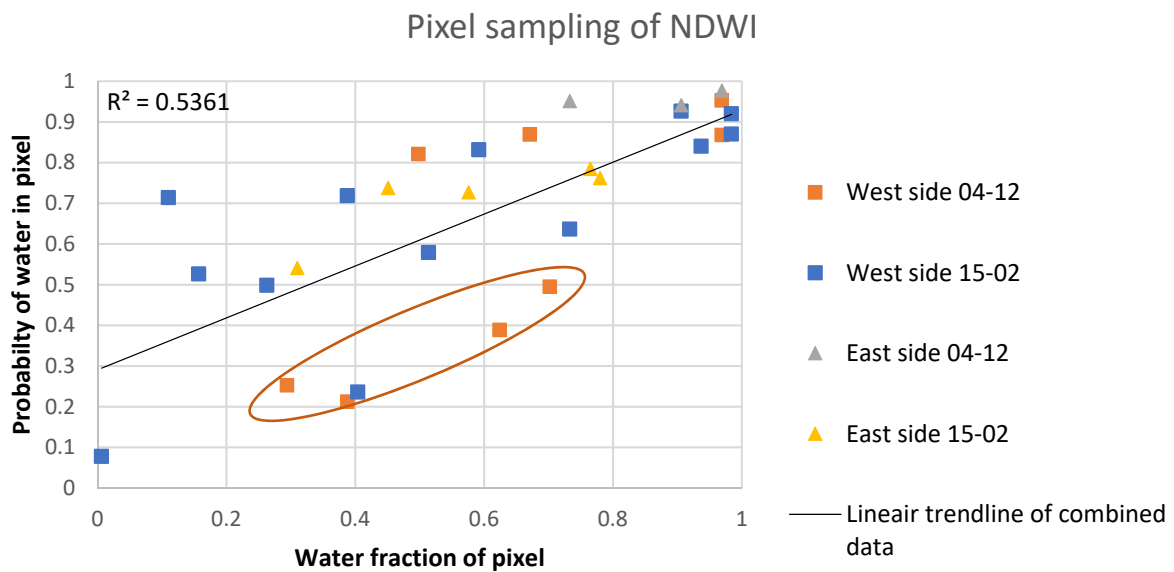


Figure 57 Pixel sampling of NDWI, for the GNSS waterline points

Figure 58 contains more scattered data, indicating that there is a weaker relation between the water fraction of a pixel and the probability of a pixel being water for the green and SWIR2 index compared to the pan sharpened MNDWI. This is also confirmed by the low R-squared value. The probability index ND\_gr\_sw2 is discussed as well because it showed one of the better results during the ROC analysis for classification. In this sub-pixel analysis, it shows to be less suitable for sub-pixel analysis. The west side of the 4<sup>th</sup> of December shows more or less a linear pattern as well as the West side of the 15<sup>th</sup> of February. The east side seems to show the most scattered data. But it has to be noted that the east sides contained only three to four points while the west side contained ten to eleven points, making it difficult to obtain a grounded conclusion on a few points.

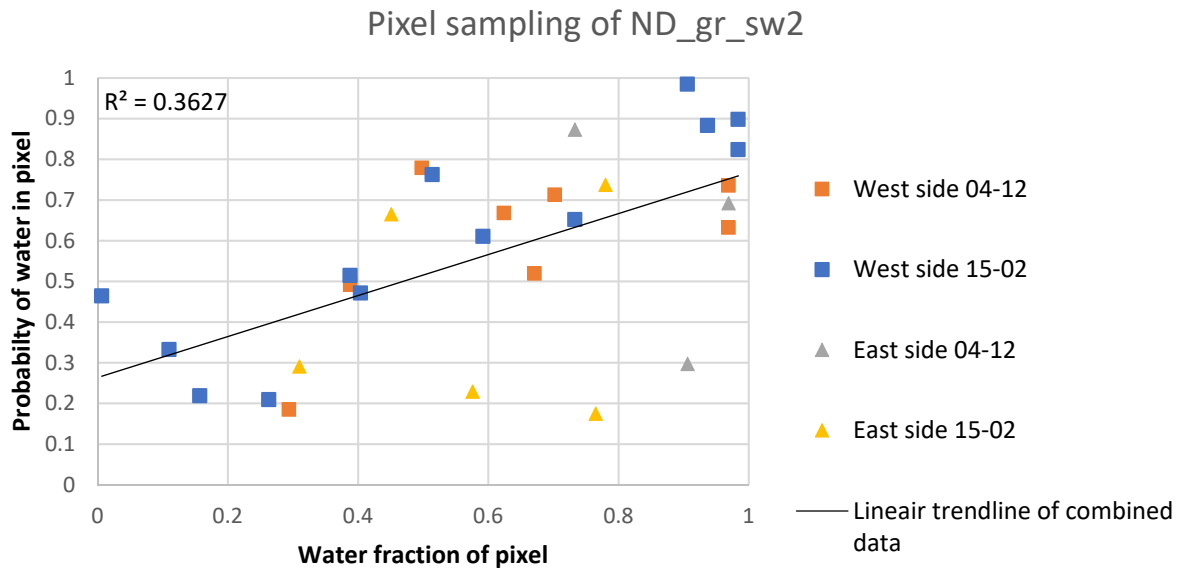


Figure 58 Pixel sampling of ND\_gr\_sw2, for the GNSS waterline points

The majority of the pixel sampling results of the combined indices with Bayes theorem seem to have a higher linear relation than with the single probability index bands. This could indicate that for sub-pixel analysis the combinations of probability indices perform better. Figure 82 of the appendix, section [Water fraction relation images](#), also shows a low relation in the probability band of ND\_rd\_sw2 with the water fraction, but the Bayes combination, Bayes 0-3, of NDWI with this index, ND\_rd\_sw2, shows the highest linear relation of the water fraction pixel analysis results. Not only does the Bayes 0-3 band shows a possible relationship in the water fraction pixel analysis, but the visualisation of this band also shows better discriminative behaviour to detect inundated areas, as can be seen in Figure 77 of the appendix, section [Probability bands visualized](#). It seems that a relationship between the probability band Bayes 0-3 and the water fraction of the underlying pixels is present and will, therefore, be used in the next section for river-width analysis.

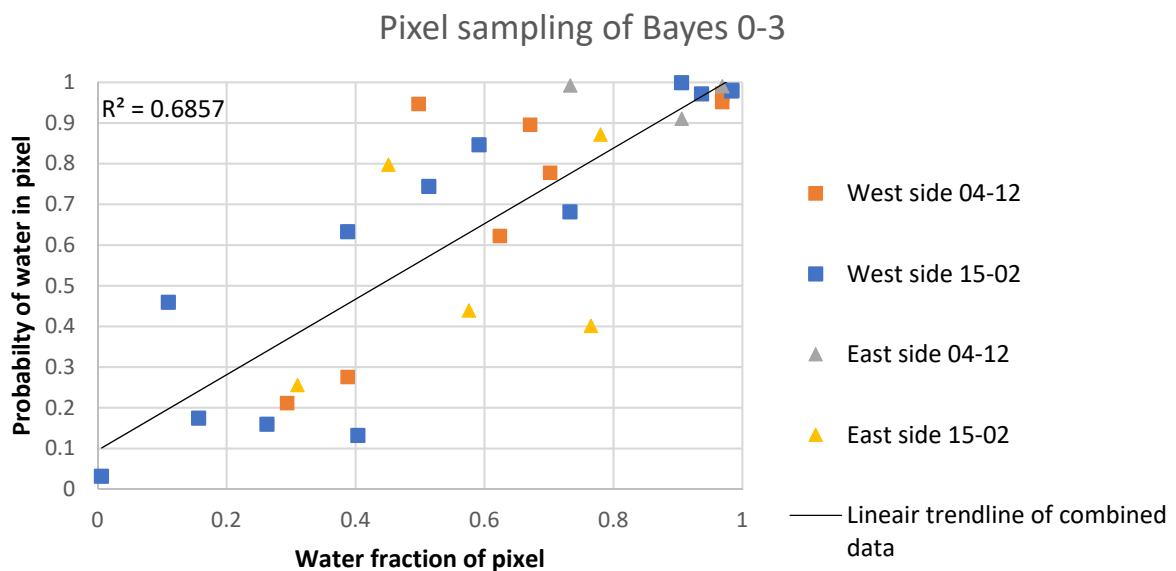


Figure 59 Pixel sampling of Bayes 0-3 combination, for the GNSS waterline points

The second best performing Bayes theorem combination within this sub-pixel analysis is the combination with index 0, NDWI and index 4, ND\_rd\_sw1. The scatter of the data points are larger than

with the Bayes combination 0-3. There is not a large difference in the spread of values between the riversides and the days noticeable. In the four best performing bands mentioned in this section, the data points close to a probability of 1, are also close to a water fraction of 1, indicating that a high water fraction correlates well with the probability of being water or a pixel. However, the visualized image of the Bayes 0-4 band shows a lower discriminative behaviour for inundated areas, compared with the Bayes 0-3 band. The visualization of Bayes 0-4 can be seen in Figure 76, of the appendix, section [Probability bands visualized](#).

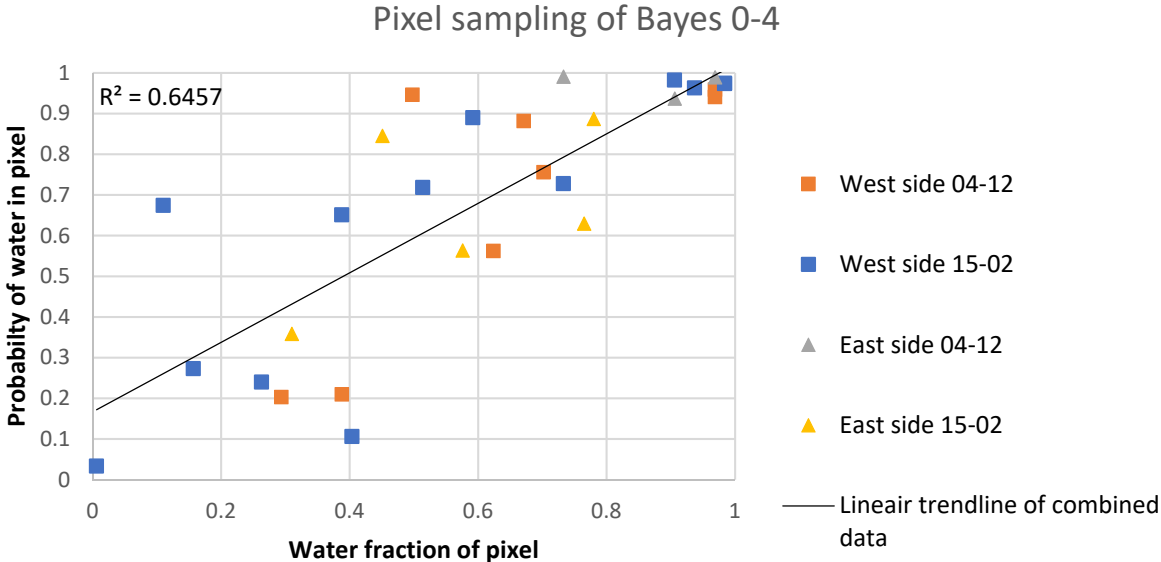


Figure 60 Pixel sampling of Bayes 0-4 combination, for the GNSS waterline points

The water fraction pixel analysis was performed, on GNSS points, during a clear sky satellite overpasses. From the results obtained of the two fieldwork days so far, there does not seem to be a large variation between the two days. This could indicate that the relations found between water fraction and the probabilities of being water are constant over time. However, there is not enough data to fully support this. More measurements in different periods of the year have to be conducted to also analyse if seasonal varieties have an influence. The two measuring days of this research were both during the winter period. There is also a need for research to see if the found relations hold for other study locations. When the found water fraction relations also count for other locations, it would mean that once the relationship is constructed, there is no need for additional fieldwork, for this step, when applying the method of this thesis. The water fraction relationship is needed for pixel dissection and would be a step of this new method that is based on fieldwork as long as there is no further research done to other locations and periods.

### 4.7.3. River width analysis results

In this section, the river-width results obtained by the different methods are shown. The river-width measurements are performed on five locations for the first fieldwork day and on eight locations for the second fieldwork day. The amount was limited by the GNSS measurements points on both sides, as the river width is measured between the GNSS points on both sides of the river. This was done to exclude any interpolation errors by applying river-width estimations on the interpolated river outline between the GNSS points. This interpolated river outline can be seen in Figure 13, of section 4.1.

For comparison purposes, the two conventional classification methods, Otsu thresholding and Supervised Training map classification, are tested on the same river cross-sections as the new sub-pixel based method of this research. The measured river widths in the tables below, show the average absolute, the minimum and the maximum deviation over the locations for an index, per fieldwork day. The absolute deviation is calculated by using the actual distance between the measured GNSS points as actual width. Figure 61 to Figure 65 show per method for the different indices a boxplot, with the data of all locations of both days combined. This means that each boxplot contains 13 measurement locations with the absolute deviation as input.

The site-specific indices are used to obtain a river-width via Otsu's thresholding method. These results, for the two fieldwork days, can be seen in Table 9 and Table 10. Otsu's thresholding method uses a hard threshold, by classifying on pixel scale, therefore not taking into account mixed pixels. The classified water pixels over the waterline vary in the longitudinal direction due to this hard threshold, as seen in the close-up part of Figure 18, in section 4.2.1. In Table 9, it can be seen that the indices NDWI and ND\_rd\_nr show large deviations in river widths caused by misclassification of bare-soil as water. The misclassification is due to the influence of the NIR band in the indices. However, the influences on misclassification of the Pan-sharpening method with the NIR band is lowered for the MNDWI<sub>10</sub> band as probability band, as can be seen in Table 12 and Table 13. The MNDWI<sub>10</sub> in combination with Otsu' thresholding seems, based on the results of the two days, the best performing due to the lowest average absolute deviation on both days. All indices classified by Otsu's method resulted in the second fieldwork day having, on average, a lower deviation than the first fieldwork day over the locations. It seems like this difference between days has something to do with the soil conditions or the higher amount of basalt blocks present at the river edge. The first fieldwork day was during a long dry period, with the river at a low level, which causes large parts of the basalt river edge protection blocks to be visual. While the second fieldwork day was during wetter conditions, even with inundated areas on the floodplains.

Table 9 River width average, min and max absolute deviations by Otsu's method \*04-12-2018

<i>Index</i>	<i>Average absolute deviation [m]</i>	<i>Min [m]</i>	<i>Max [m]</i>
<i>NDWI</i>	88.4	60.7	112.6
<i>MNDWI</i>	21.3	9.9	30.0
<i>MNDWI<sub>10</sub></i>	16.9	0.3	63.0
<i>ND_rd_sw2</i>	28.0	7.4	47.0
<i>ND_rd_sw1</i>	20.2	6.9	28.8
<i>ND_rd_nr</i>	109.2	57.7	132.1
<i>ND_gr_sw2</i>	30.1	26.4	36.3

Table 10 River width average, min and max absolute deviations by Otsu's method \*15-02-2019

<i>index</i>	<i>Average absolute deviation [m]</i>	<i>Min [m]</i>	<i>Max [m]</i>
<i>NDWI</i>	13.1	4.4	32.8
<i>MNDWI</i>	11.2	0.7	16.7
<i>MNDWI<sub>10</sub></i>	8.8	0.7	12.5
<i>ND_rd_sw2</i>	11.1	0.7	16.7
<i>ND_rd_sw1</i>	11.1	0.7	16.7
<i>ND_rd_nr</i>	9.2	0.7	32.8
<i>ND_gr_sw2</i>	11.1	0.7	16.7

Figure 61 shows the boxplots corresponding to the river width deviations obtained by applying Otsu's thresholding method. The NDWI and the ND\_rd\_nr bands show large deviations as was also presented above in Table 9 and Table 10. The bands MNDWI, MNDWI<sub>10</sub> and ND\_rd\_sw1 show all three a low Interquartile Range, indicating that the middle 50% of the data is within a small range. The yellow line in the boxplots represents the median of the data. The medians of all indices are located close to each

other around 20 metre deviation, indicating half of the data is below the 20 metre deviation. The overall classification results by Otsu thresholding show a high deviation in the river-width estimation, which is on average missing a 10-metre water pixel on each riverside.

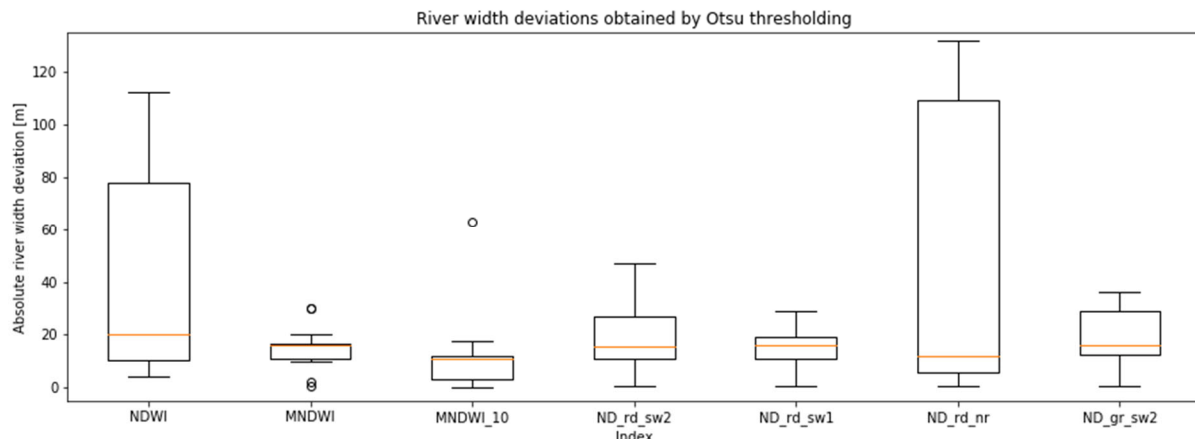


Figure 61 Boxplot of river width deviations by Otsu thresholding \*data of both fieldwork days

The second conventional method that is performed for comparisons reasons was the Supervised Training map classification. The average, minimum and maximum absolute deviation results of this method for the different locations can be seen in Table 11 for both fieldwork days. Figure 64 shows the boxplot of the Supervised Training map results of all 13 measured locations. It can be seen that the Interquartile Range (IQR) is small for this method. The deviations for both fieldwork days are small, but it has to be noted that this classification is on a pixel base. This means that a pixel is classified as either water or land. When a classifier is able to perfectly classify water on pixel basis, then the maximum deviation should be around 10 metres for the river width. This is a 5-metre error on both sides when the water fractions of a pixel below 50% are not seen as a water pixel and everything above is. This is when the pixels lay perpendicular over the river. If the pixel placement is diagonal the error could be maximum around 7-metre per riverside. The resolution of the satellites pixels plays a role in the possible error. Secondly, to obtain a training map, fieldwork is needed to ‘train’ the classification method, which is not always possible to conduct.

Table 11 River width average, min and max deviations by Supervised Training map classification

Fieldwork Day	Average absolute deviation [m]	Min [m]	Max [m]
4-12-2019	7.6	0.3	15.2
15-2-2019	5.5	0.7	11.1

The results of the new method proposed by this research can be seen in Table 12 and Table 13. The probability index bands and the combined Bayes bands are used to obtain river-widths at the same locations as used above with the other two methods. The optimum thresholds resulted from the ROC curves of section 4.7.1.2 and 4.7.1.3, are used to classify the single probability bands but also the combined Bayesian bands. The average, minimum and maximum absolute deviation results of this method for the different locations can be seen in the columns of the tables. Again, also after transforming the index values to probability values, the second fieldwork day shows lower deviations between the modelled and the actual width. The NDWI shows as probability band also large deviations, while the ND\_rd\_nr band significantly decreased its deviations. This indicates that the transformation from index values to probability values has a positive effect on the classification for this band. The probability band ND\_rd\_sw2 seems to be the best-performing band for the sub-pixel river width estimation of the single probability bands according to the average deviations. Bayes 1-3 seems to be the best performing of the combined Bayesian indices. When analysing the boxplots of Figure 62 and Figure 63 it shows that the MNDWI\_10 has a lower Interquartile Range than the ND\_rd\_sw2 but has an overall higher deviation. This lower IQR could indicate why the MNDWI\_10 shows a better water fraction relation than the other Indices. Bands Bayes 0-3, Bayes 1-5 and Bayes 5-6 show within the Bayesian combinations a low IQR, with Bayes 1-5 showing the lowest spread. From Figure 62 and Figure 63 it can be seen that using probabilities instead of the original index values improves the classification. Combining the probability

indices results in more equal results between the bands. However, for the first fieldwork day, larger deviations are still present.

Table 12 River width average, min and max absolute deviations by ROC thresholding on single and combined probability indices \*04-12-2018

Index	Average absolute deviation [m]	Min [m]	Max [m]
NDWI	83.2	14.3	112.6
MNDWI	15.7	6.9	32.8
MNDWI_10	17.8	9.5	32.3
ND_rd_sw2	15.2	9.4	32.3
ND_rd_sw1	17.3	6.0	32.8
ND_rd_nr	25.4	17.3	39.5
ND_gr_sw2	22.4	0.3	57.5
Bayes 0-3	16.2	6.9	32.3
Bayes 0-4	25.4	16.8	40.0
Bayes 1-3	14.9	3.1	32.8
Bayes 1-5	18.9	10.8	32.8
Bayes 4-6	15.5	0.4	32.8
Bayes 5-6	17.8	7.4	32.8
bays034	24.2	10.8	40.0
bays156	21.9	10.8	32.8

Table 13 River width average, min and max absolute deviations by ROC thresholding on single and combined probability indices \*15-02-2019

Index	Average absolute deviation [m]	Min [m]	Max [m]
NDWI	116.7	76.1	128.7
MNDWI	38.8	25.4	49.3
MNDWI_10	8.9	0.7	13.0
ND_rd_sw2	5.6	0.2	11.3
ND_rd_sw1	7.2	0.7	12.5
ND_rd_nr	12.0	4.4	20.9
ND_gr_sw2	5.7	0.2	11.3
Bayes 0-3	7.8	0.7	12.5
Bayes 0-4	8.9	2.2	13.0
Bayes 1-3	5.7	0.2	11.3
Bayes 1-5	8.4	0.7	13.0
Bayes 4-6	6.1	0.7	12.3
Bayes 5-6	7.7	0.7	12.5
bays034	7.8	0.7	12.5
bays156	7.8	0.7	12.5

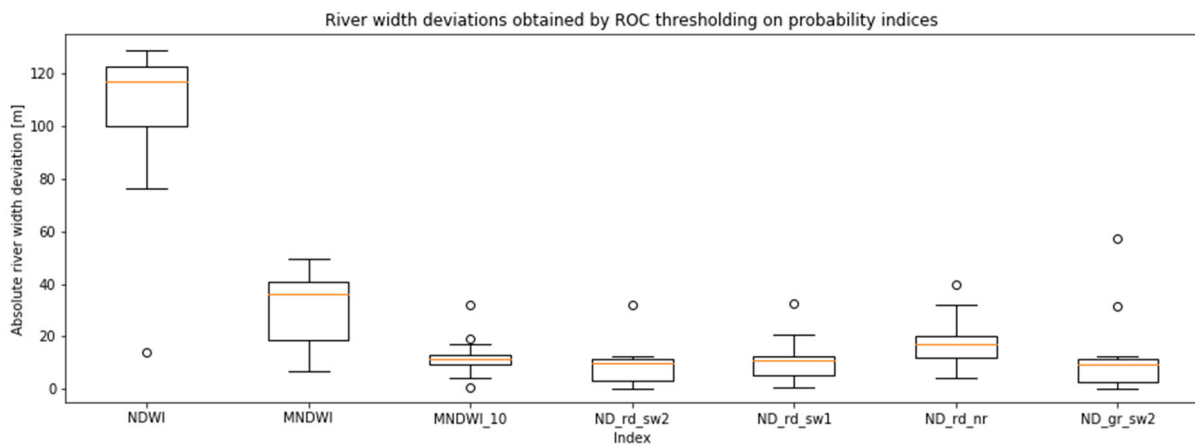


Figure 62 Boxplot of river width deviations by ROC threshold for probability indices \*data of both fieldwork days

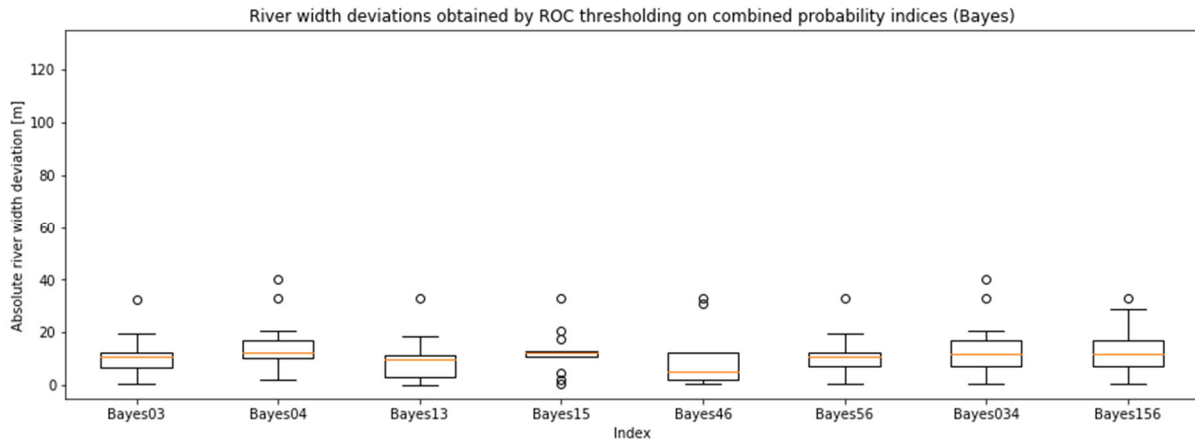


Figure 63 Boxplot of river width deviations by ROC threshold for combined Bayes probability indices \*data of both fieldwork days

The previous section, section 4.7.2, showed that there were two probability bands that seemed to indicate a relationship between the probability of water by the index and the actual fraction of water in the same underlying pixel. Therefore in Table 14 and Table 15, these two bands, MNDWI\_10 and Bayes 0-3 are used to perform a river width estimation on sub-pixel base with the found water fraction relation. The results of the use of sub-pixel base analysis show a more accurate river width-estimation. The first fieldwork day shows low deviation results, as well as the second fieldwork day. The average river-width deviations of the pan-sharpened MNDWI and Bayes0-3 decreased to under 5 and 7 metres deviation by including the found water fraction relationships. This indicates that the larger deviations found by determining river widths on only pixel base can be highly improved by the use of this new sub-pixel analysis. With the addition of the mixed pixel water content, the placement of pixels on the measured location has less influence on the results for the river-width. Figure 65 also shows these small ranges in values in the boxplots of the bands MNDWI\_10 and Bayes 0-3.

Table 14 River width average, min and max absolute deviations on sub-pixel level \*04-12-2018

Index	Average absolute deviation [m]	Min [m]	Max [m]
MNDWI_10	4.0	0.6	11.7
bays03	4.9	1.0	10.9

Table 15 River width average, min and max absolute deviations on sub-pixel level \*15-02-2019

Index	Average absolute deviation [m]	Min [m]	Max [m]
MNDWI_10	6.2	0.7	18.6
bays03	6.7	1.9	17.4

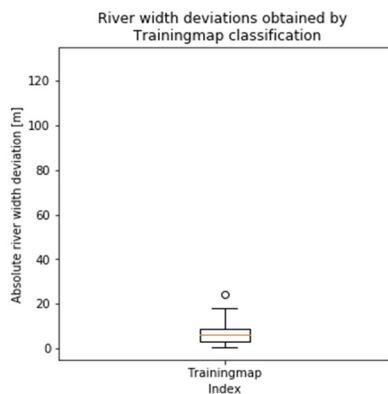


Figure 64 Boxplot of river width deviations by Training map classification \*data of both fieldwork days

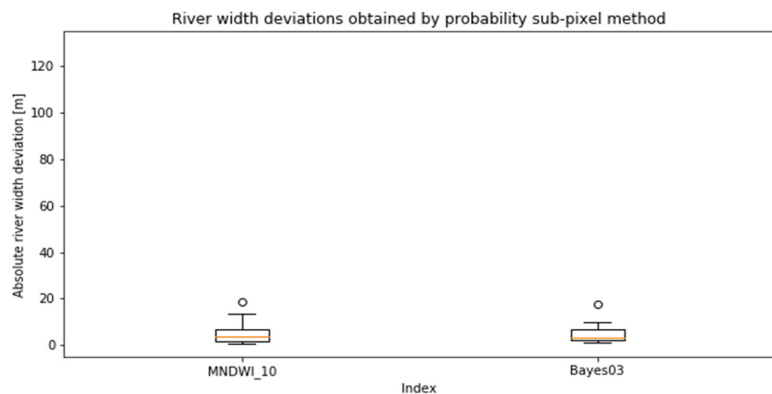


Figure 65 Boxplot of river width deviations by ROC threshold for probability indices on sub-pixel level \*data of both fieldwork days

The ROC analysis, of section 4.7.1, was used for the thresholding on the probability bands to perform water classification for the river-width estimations. The ROC curves were obtained by using the GNSS points to construct water and land polygons for the true positive rates and the false positive rates. This means that also for this part, ground truth data was required. Thresholds obtained by the optimum ROC threshold and Otsu's threshold are different from each other when applied to the probability indices, as can be seen in Table 16. Otsu's thresholds are mainly lower than those obtained via the

ROC curve for the probability bands, which is due to the wide separation of the classes, high inter-class variation, after transforming the indices to probability bands. There are a few points in between, resulting in Otsu's method thresholding a value between the two classes, around a probability value of 0.5, as can also be seen for the thresholds of Table 16. The edge detection used in this research could be a potential solution for the need of ground-truth data for the construction of the ROC curves. This needs to be further researched to be able to do the ROC analysis with only remote data.

Table 16 Comparison ROC and Otsu threshold for probability bands

Index	4-12-2018		15-2-2019	
	ROC threshold	Otsu threshold	ROC threshold	Otsu threshold
prob_NDWI	0.63	0.46	0.51	0.45
prob_MNDWI	0.63	0.50	0.86	0.48
prob_MNDWI_10	0.82	0.50	0.65	0.50
prob_ND_rd_sw2	0.70	0.53	0.41	0.50
prob_ND_rd_sw1	0.75	0.53	0.61	0.51
prob_ND_rd_nr	0.96	0.50	0.89	0.48
prob_ND_gr_sw2	0.56	0.49	0.51	0.53



# 5.

## Conclusion

The main objective of this research was to obtain a better method for water classification to improve river-width determinations. This was studied by conducting remote analyses in combination with obtained ground-truth data. In this section, the conclusions of the research and the newly developed method are presented. This 'Conclusion' chapter addresses the main research question followed by the sub-research questions stated in section 1.5.

### **'How to optimally assess sub-pixel accurate river widths from optical remote sensing?'**

Band combinations, indices, transformed into probability bands, based on the spread of river edge values, result in filtering out a part of the unwanted influence of certain land types that are similar in reflectance signal to water. Obtaining probability bands of site-specific water discriminating combinations enable the ability to analyse and obtain relationships between the water fraction of a pixel and the probability of an index value. In this research, it is shown that there is a large potential in getting a more accurate river width estimation by the use of water fraction relationships to obtain sub-pixel data of the pixels adjacent to the classified waterbody.

### ***'What is the current cutting-edge water classification method for land and water?'***

The use of automated methods are popular, this is also the case for water classification methods. Otsu's thresholding method applied to the spectral satellite image is one of these automated methods. This method looks at the pixels value distribution and is independent of ground-truth data collection. The results of this method are highly dependable on the inter-class variance found in the band or index for the classification. In the results of this method, section 4.2.1, it showed that the conventional water index, the NDWI, works well in combination with certain land classes. However, in the study location, there was a land type present, bare-soil, that caused misclassifications and therefore at certain locations overestimation of the river width. The modified water index, MNDWI, which is a newer index, was constructed to avoid this misclassification by using a satellite band that has a higher discriminative ability between water and the land classes causing classification confusion. The downside of this index is the introduction of the lower spatial resolution from the SWIR1 band.

### ***'How can bands be found that discriminate land from water?'***

As seen with the NDWI, some indices perform less than other indices, depending on the location and the present land and water conditions. Therefore, researching, site-specific, indices are of the essence. To do this, it is first needed to know what bands show discriminative abilities. Sampling historical satellite data of a study location can result in a complete dataset containing variations of signals through the years. By using 20 years of satellite data, a considerable analysis was performed. Plotting separate satellite bands as histogram data combined with average pixel values for land and water classes shows a first impression of the discriminating abilities of the bands in the area of interest.

***'How can combinations of bands be found that discriminate land from water?'***

After obtaining site-specific discriminating bands, an analysis can be performed on combinations of these found bands. Using the same 20 years of data as mentioned above to plot two bands, at a time, in a scatterplot combined with a kernel density estimation over the points in the scatterplot, showed to be a well working approach to obtain discriminating combinations for water. The inter-class variance and the spread of values can be analysed with the combination of two bands in a scatterplot with a kernel density estimation visualized in density contour lines.

***'What image enhancements can be done to improve the classification to obtain a more precise river-width?'***

There are different types of image enhancement methods. The in this research applied pan-sharpening method on the SWIR1 band to obtain a 10-metre resolution instead of 20-metres worked well for water fraction relations. The water fraction of the pixels based on ground-truth data compared to the pan-sharpened MNDWI probability band showed a linear relationship with an R-squared value of 0.689, as can be seen in Figure 56. This was the best resulting index for obtaining a relation between the water fraction of a pixel and the probability of the pixel of being water. For general water classification, however, the pan-sharpening effect of using the NIR band as a panchromatic band has negative influences. The NIR band seemed to transfer the band's characteristics that result in misclassification of bare-soil to the SWIR1 band by pan-sharpening via the IHS method.

'Bicubic' resampling turned out to be a well working technique to obtain 1-metre resolution indices, that can be used to perform river edge detection on sub-pixel scale. Via this 1-metre scale detected edge, the pixels on the river edge could be sampled and used to construct cumulative density functions, CDF's, of the indices. The CDF's were needed to transform the obtained indices into probability indices for being water.

***Do combinations of locally chosen normalized indices improve the water classification compared to the conventional classification indices like MNDWI and NDWI?***

By looking at sub-pixel river width estimations based on the newly proposed method it seems there is more information available to obtain a more accurate river-width by using probability indices. For the pixel-based classification techniques, the techniques that do not look at the sub-pixel base, it depends on the water fraction of the mixed pixels whether these pixels are classified as water or as land, which directly influences the deviation of the river width. The river-width results, of section 4.7.3, show that, by combining probability indices, the spread of results between the combinations is significantly decreased, indicating lower importance for the choice of bands that should be combined. From the water fraction pixel analysis, it seemed that the probability band of the pan-sharpened MNDWI and the combined Bayes band, Bayes0-3, show the best results for a relation between the water fraction in a pixel and the probability of a pixel for being water by these bands. The average river-width deviations of the pan-sharpened MNDWI and Bayes0-3 decreased from 16 and 9 metres, respectively for the first and second fieldwork day, to under 5 and 7 metre deviation by including the found water fraction relationships. Based on this research, these two probability bands show the highest potential for sub-pixel river width estimations.

# 6.

## Recommendations

In the Results and discussion chapter, the findings of this research were reflected. Interesting and useful results were found for a new method to obtain river-widths on sub-pixel base. However, there are still some recommendations that followed from the discussions of the results.

The objective was to find a new method for sub-pixel accurate river-width determinations. But this research also emphasized the usefulness of methods that could be applied remotely without the need of ground-truth data. The Results and discussion chapter mentioned the need for ground-truth data to obtain the relationship between the water fraction and the probability of a pixel by a certain index. However, it seemed from the water fraction analysis results, of section 4.7.2, that there is not a large variation between the two days. More measurements in different periods of the year have to be conducted to also analyse if seasonal varieties have an influence. The two measuring days of this research were both during the winter period. There is also a need for research to see if the found relations hold for other study locations. When the found water fraction relations also count for other locations and periods, it would mean that once the relationship is constructed, there is no need for additional fieldwork when applying the new sup-pixel base river-width estimation method of this thesis.

The optimum thresholds based on the ROC curves are used for the probability bands to make a water classification. It is recommended to analyse if land and water polygons based on the used edge detection is sufficient to eliminate the current need for ground-truth data to make these polygons.

Another implementation that would benefit the usability of this new method is to make an automatization of the processes of the methods. There are still some steps in the workflow of the new sub-pixel base method like analysing the discriminating band combinations, which are manually performed at the moment. The threshold set for canny edge detection for the different indices is also manually chosen in this research. This could be further researched to construct an automated process.

An option that is worth further research is to construct relations between river-widths based on its probability of being water without the need of ground-truth data, which would aid in the step to automatization. This could be illustrated as a distribution in a figure. In combination with this figure, the distribution of values can be analysed and a river-width can be obtained belonging to a certain probability of interest. An example of how such a curve looks like can be seen in Figure 91, section Probability-width curve of the appendix. So far it seems like the probabilities of the different indices differ and result in the different river-widths.

## References

- Bilock, Alexander, Carl Jidling, and Ylva Rydin. 2016. *Modelling Bivariate Distributions Using Kernel Density Estimation*.
- Bolboaca, SD, and L Jantschi. 2006. "Pearson versus Spearman, Kendall's Tau Correlation Analysis on Structure-Activity Relationships of Biologic Active Compounds." *Leonardo Journal of Sciences* (9): 179–200. [http://ljs.academicdirect.org/A09/179\\_200.htm](http://ljs.academicdirect.org/A09/179_200.htm).
- Brodu, Nicolas. 2017. "Super-Resolving Multiresolution Images With Band-Independent Geometry of Multispectral Pixels." *IEEE Transactions on Geoscience and Remote Sensing* 55(8): 4610–17.
- Burazerović, Dževdet et al. 2013. "Detecting the Adjacency Effect in Hyperspectral Imagery with Spectral Unmixing Techniques." *IEEE Journal of Selected Topics in Applied Earth Observations and Remote Sensing* 6(3): 1070–78.
- CANNY, JOHN. 1987. "A Computational Approach to Edge Detection." *Readings in Computer Vision*: 184–203. <https://www.sciencedirect.com/science/article/pii/B9780080515816500246> (June 5, 2019).
- Combe, Steve. 2014. "A Few Things to Consider When Purchasing Your Next ADCP." *september 4*. <http://www.elecdata.com/blog/a-few-things-to-consider-when-purchasing-your-next-adcp/> (December 15, 2018).
- Donchyts, Gennadii et al. 2016. "A 30 m Resolution Surfacewater Mask Including Estimation of Positional and Thematic Differences Using Landsat 8, SRTM and OPenStreetMap: A Case Study in the Murray-Darling Basin, Australia." *Remote Sensing* 8(5).
- Du, Yun et al. 2016. "Water Bodies' Mapping from Sentinel-2 Imagery with Modified Normalized Difference Water Index at 10-m Spatial Resolution Produced by Sharpening the Swir Band." *Remote Sensing* 8(4).
- ESA. "Sentinel-2, Main Page." <https://sentinel.esa.int/web/sentinel/missions/sentinel-2> (December 12, 2018a).
- . "Sentinel-2 MSI Introduction." <https://sentinel.esa.int/web/sentinel/user-guides/sentinel-2-msi> (April 11, 2019b).
- . "Sentinel-2 Resolution." <https://earth.esa.int/web/sentinel/technical-guides/sentinel-2-msi/msi-instrument> (March 5, 2019c).
- . "SNAP." <http://step.esa.int/main/toolboxes/snap/> (February 25, 2019d).
- Fawcett, Tom. 2006. "An Introduction to ROC Analysis." *Pattern Recognition Letters* 27(8): 861–74.
- Fekete, B. M., and Charles J Vörösmarty. 2007. "The Current Status of Global River Discharge Monitoring and Potential New Technologies Complementing Traditional Discharge Measurements." *Predictions in Ungauged Basins: PUB Kick-off (Proceedings of the PUB Kick-off meeting held in Brasilia, 20–22 November 2002)*, IAHS publication no. 309 (November 2002): 129–36.
- Geomatca. 2013. "PAN Sharpening." *Technical Specifications*: 2. <http://www.pcigeomatics.com/pdf/PanSharp.pdf>.
- Gis geography. 2018. "What Is NDVI?" *24-02-2018*. <https://gisgeography.com/ndvi-normalized-difference-vegetation-index/> (February 25, 2019).
- Google. "Debugging GEE." *march 18, 2019*. <https://developers.google.com/earth-engine/debugging#scaling-errors> (April 3, 2019a).
- . "Relative Cloud Likelihood." <https://developers.google.com/earth-engine/landsat#simple-cloud-score> (April 23, 2019b).
- Gorelick, Noel et al. 2017. "Google Earth Engine: Planetary-Scale Geospatial Analysis for Everyone." *Remote Sensing of Environment* 202: 18–27. <https://doi.org/10.1016/j.rse.2017.06.031>.
- Hartman, Raymond. "Floodplain Inundation, Lonely House." <http://www.raymondhartman.nl/gallery/ijssel-bij-herxen-drone-fotografie/> (April 13, 2019).
- Huang, Chang, Yun Chen, Shiqiang Zhang, and Jianping Wu. 2018. "Detecting, Extracting, and Monitoring Surface Water From Space Using Optical Sensors: A Review." *Reviews of Geophysics* 56(2): 333–60.
- Lee, CMG. "Resampling Image." [https://commons.wikimedia.org/wiki/File:Comparison\\_of\\_1D\\_and\\_2D\\_interpolation.svg](https://commons.wikimedia.org/wiki/File:Comparison_of_1D_and_2D_interpolation.svg) (May 10, 2019).
- Lee, Huang Chen et al. 2011. "A Low-Cost Method for Measuring Surface Currents and Modeling Drifting Objects." *IEEE Transactions on Instrumentation and Measurement* 60(3): 980–89.
- Leica. "Leica GS14 Manual." : 4. <https://w3.leica-geosystems.com/downloads123/zz/gpsgis/vivags14/brochures->

- datasheet/leica\_viva\_gnss\_gs14\_receiver\_dat\_us.pdf (January 12, 2019).
- Li, Wenbo et al. 2013. "A Comparison of Land Surface Water Mapping Using the Normalized Difference Water Index from TM, ETM+ and ALI." *Remote Sensing* 5(11): 5530–49.
- Ma Jianwen, Li Xiaowen, Chen Xue, and Feng Chun. 2006. "Target Adjacency Effect Estimation Using Ground Spectrum Measurement and Landsat-5 Satellite Data." *IEEE Transactions on Geoscience and Remote Sensing* 44(3): 729–35.
- Makaske, Bart, Gilbert J. Maas, Claus Van Den Brink, and Henk P. Wolfert. 2011. "The Influence of Floodplain Vegetation Succession on Hydraulic Roughness: Is Ecosystem Rehabilitation in Dutch Embanked Floodplains Compatible with Flood Safety Standards?" *Ambio* 40(4): 370–76.
- McFeeters, S. K. 1996. "The Use of the Normalized Difference Water Index (NDWI) in the Delineation of Open Water Features." *International Journal of Remote Sensing* 17(7): 1425–32.
- Otsu, Nobuyuki. 1979. "A Threshold Selection Method from Gray-Level Histograms." *C*(1): 62–66.
- Pan, Feifei, Cheng Wang, and Xiaohuan Xi. 2016. "Constructing River Stage-Discharge Rating Curves Using Remotely Sensed River Cross-Sectional Inundation Areas and River Bathymetry." *Journal of Hydrology* 540: 670–87. <http://dx.doi.org/10.1016/j.jhydrol.2016.06.024>.
- Parker, J. Anthony, Robert V. Kenyon, and Donald E. Troxel. 1983. "Comparison of Interpolating Methods for Image Resampling." *IEEE Transactions on Medical Imaging* 2(1): 31–39.
- Pix4D. "Pix4D Output Page." <https://support.pix4d.com/hc/en-us/articles/202558889-Accuracy-of-Pix4D-outputs>.
- RECONNECT Consortium. 2018. "RECONNECT." [www.reconnect.eu](http://www.reconnect.eu) (December 12, 2018).
- Reeze, Bart et al. 2017. *Watersys- Teemrapportage Rijntakken 1990-2015. Ontwikkelingen Waterkwaliteit En Ecologie*.
- Richards, John A. 2015. *Erratum To: Remote Sensing with Imaging Radar*.
- Richards, John A., and Xiuping Jia. 2013. *Remote Sensing Digital Image Analysis Remote Sensing Digital Image Analysis*.
- Rijkswaterstaat. "Watervaarwegen IJssel." <https://www.rijkswaterstaat.nl/water/vaarwegenoverzicht/ijssel/index.aspx>.
- Rubayet Rahaman, Khan, Quazi Hassan, and Ahmed Razu. 2017. "Pan-Sharpening of Landsat-8 Images and Its Application in Calculating Vegetation Greenness and Canopy Water Contents." *ISPRS International Journal of Geo-Information* 6(6): 168.
- Silva, Wim, Frans Klijn, and Jos Dijkman. 2001. "Room for the Rhine Branches in The Netherlands." *SonTek*. 2015. "RiverSurveyor S5 and M9." (858): 4. <http://www.sontek.com/productsdetail.php?RiverSurveyor-S5-M9-14>.
- Triola, Mario F. 2010. "Bayes' Theorem." : 1–9.
- Uehlinger, Urs, and Karl M Wantzen. 2009. *The Rhine River Basin*.
- United States Geological Survey (USGS). 2018. *Landsat Collections | Landsat Missions*. <https://landsat.usgs.gov/landsat-collections>.
- . "Landsat 8 Mission." [https://www.usgs.gov/land-resources/nli/landsat/landsat-8?qt-science\\_support\\_page\\_related\\_con=0#qt-science\\_support\\_page\\_related\\_con](https://www.usgs.gov/land-resources/nli/landsat/landsat-8?qt-science_support_page_related_con=0#qt-science_support_page_related_con).
- . "Landsat Surface Reflectance." [https://www.usgs.gov/land-resources/nli/landsat/landsat-surface-reflectance?qt-science\\_support\\_page\\_related\\_con=0#qt-science\\_support\\_page\\_related\\_con](https://www.usgs.gov/land-resources/nli/landsat/landsat-surface-reflectance?qt-science_support_page_related_con=0#qt-science_support_page_related_con) (April 11, 2019b).
- . "What-Are-Best-Spectral-Bands-Use-My-Study." <https://landsat.usgs.gov/what-are-best-spectral-bands-use-my-study> (March 5, 2019c).
- Vaiopoulos, A. D., and K. Karantza. 2016. "Pansharpening on the Narrow VNIR and SWIR Spectral Bands of Sentinel-2." *International Archives of the Photogrammetry, Remote Sensing and Spatial Information Sciences - ISPRS Archives* 41(July): 723–30.
- Vliet van der, Nils. 2018. *The Limitations of Sentinel-2 for Water Quality Data*.
- Wang, Bin, Atsuo Ono, Kanako Muramatsu, and Noboru Fujiwaratt. 1999. "Automated Detection and Removal of Clouds and Their Shadows from Landsat TM Images." *IEICE Transactions on Information and Systems* E82–D(2): 453–60.
- Wu, Jinlong, Jianxun Wang, and Heng Xiao. 2018. "Physics-Informed Machine Learning for Data-Driven Turbulence Modeling Physics-Informed Machine Learning Framework Statistical Metrics Application I . Flow in A Square Duct Application II . Flow over Periodic Hills." In , 34603.
- Xu, Hanqiu. 2006a. "Modification of Normalised Difference Water Index (NDWI) to Enhance Open Water Features in Remotely Sensed Imagery." *International Journal of Remote Sensing* 27(14): 3025–33.
- . 2006b. "Modification of Normalised Difference Water Index (NDWI) to Enhance Open Water Features in Remotely Sensed Imagery." *International Journal of Remote Sensing* 27(14): 3025–33.

Xu, Xiangyang, Shengzhou Xu, Lianghai Jin, and Enmin Song. 2011. "Characteristic Analysis of Otsu Threshold and Its Applications." *Pattern Recognition Letters* 32(7): 956–61. <http://dx.doi.org/10.1016/j.patrec.2011.01.021>.

### Water slope

To get the water slope of the river measurements over a long extent need to be conducted. In this research, the GNSS device is used over a reach of a kilometre to map the water level. To get a more accurate result of the water slope a longer extent would be better but due to different property owners around the study location, this became difficult. The distance between each point and the water level difference are then used to get an average water slope of this section of the river. The GNSS has an error in the z-direction of approximately one centimetre and the slope of the river IJssel has an average water surface slope of 8 cm/km (Reeze et al. 2017), therefore a reasonable water slope can be achieved with this method, which would be more precise for a longer reach. The slope of the IJssel upstream is 12cm/km and starts to decrease from the middle until downstream of the river.

The results of the GNSS measurements for the slope resulted in 5cm/km and 6cm/km, respectively for the first and second fieldwork day, as can be seen in Figure 66 and Figure 67. Taking into account that the study location is on 3/4<sup>th</sup> of its length, the slope of the river should also be less than the average of 8cm/km. This means that the slope estimation is in a reasonable range.

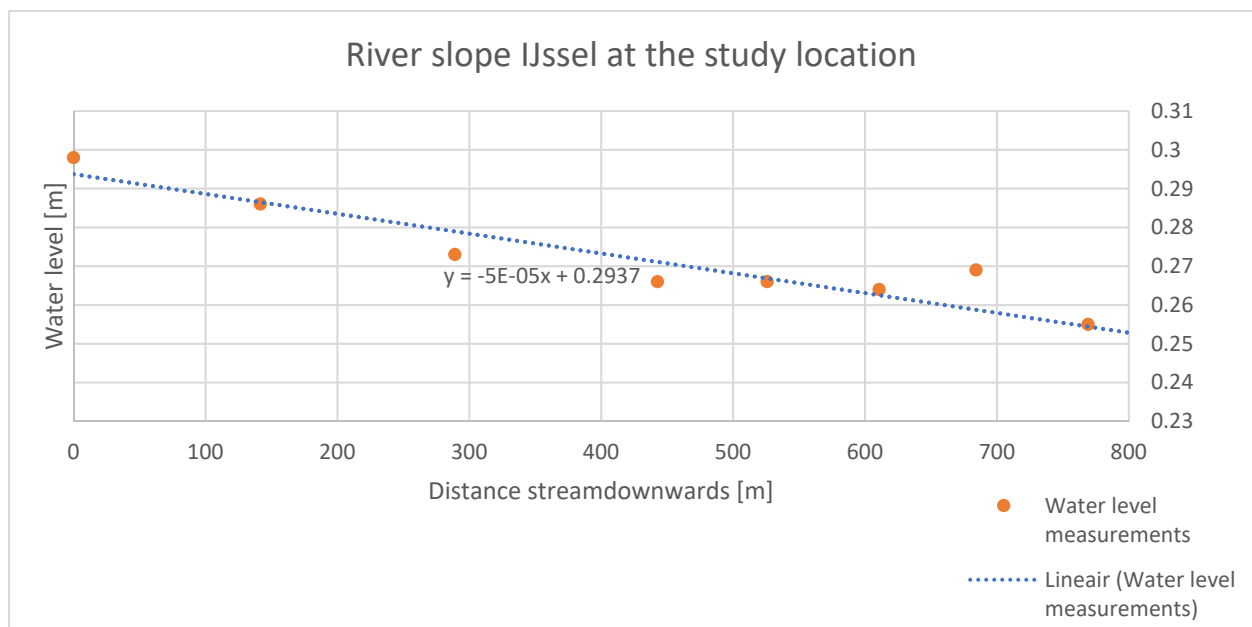


Figure 66 Slope of the river IJssel at the study location on 07-12-18 = 5cm/km

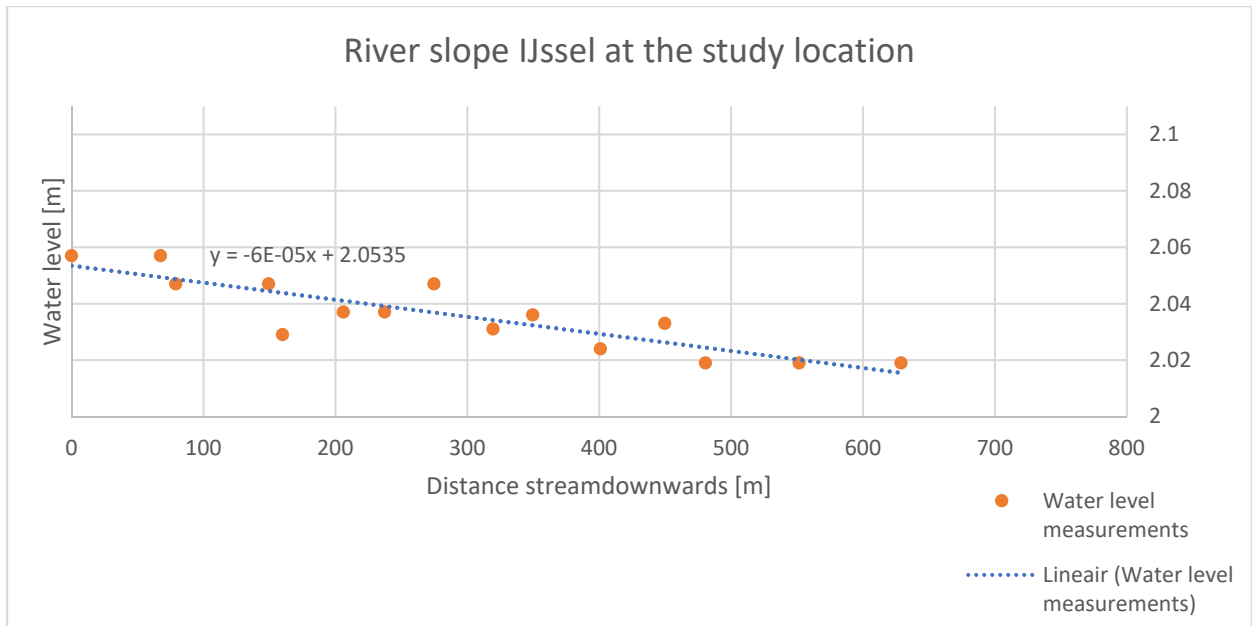


Figure 67 Slope of the river IJssel at the study location on 15-02-19 = 6cm/km

Probability bands visualized

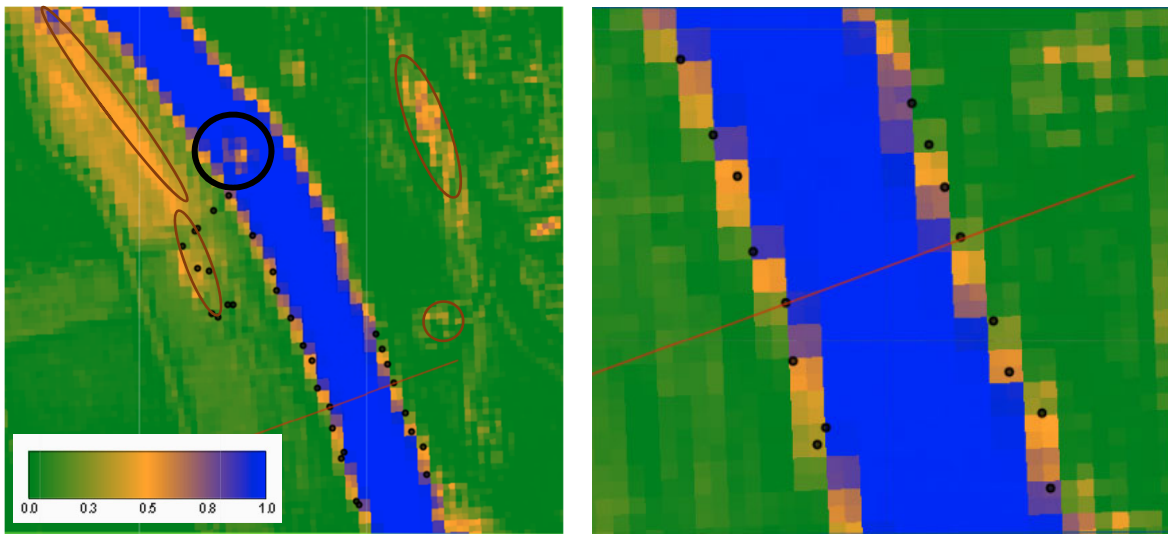


Figure 68 Probability band of the custom index: ND\_rd\_sw2, Left: overview, Right: close-up  
\*15-02-19

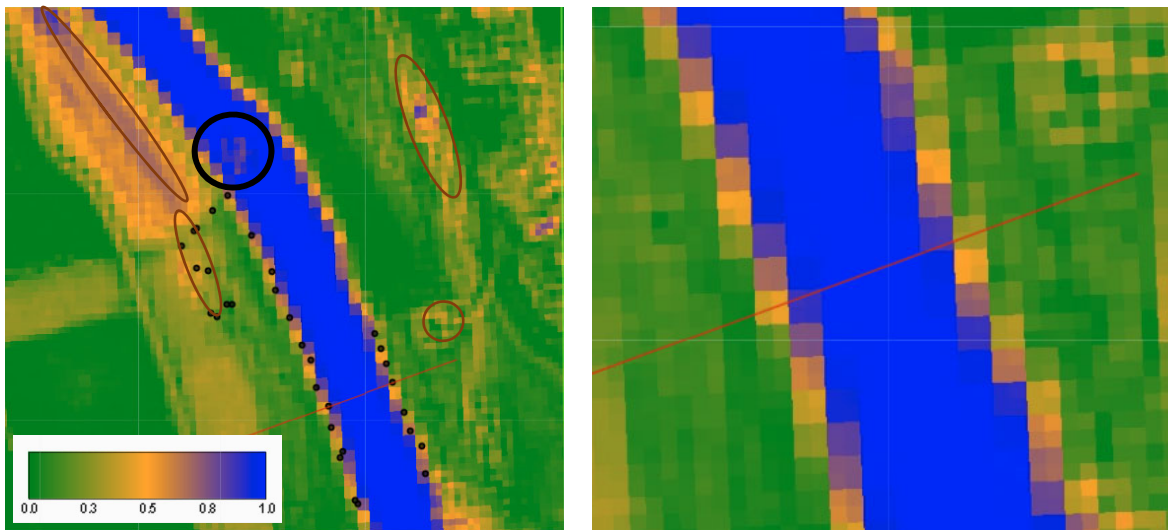


Figure 69 Probability band of the custom index: ND\_rd\_sw1, Left: overview, Right: close-up  
\*15-02-19

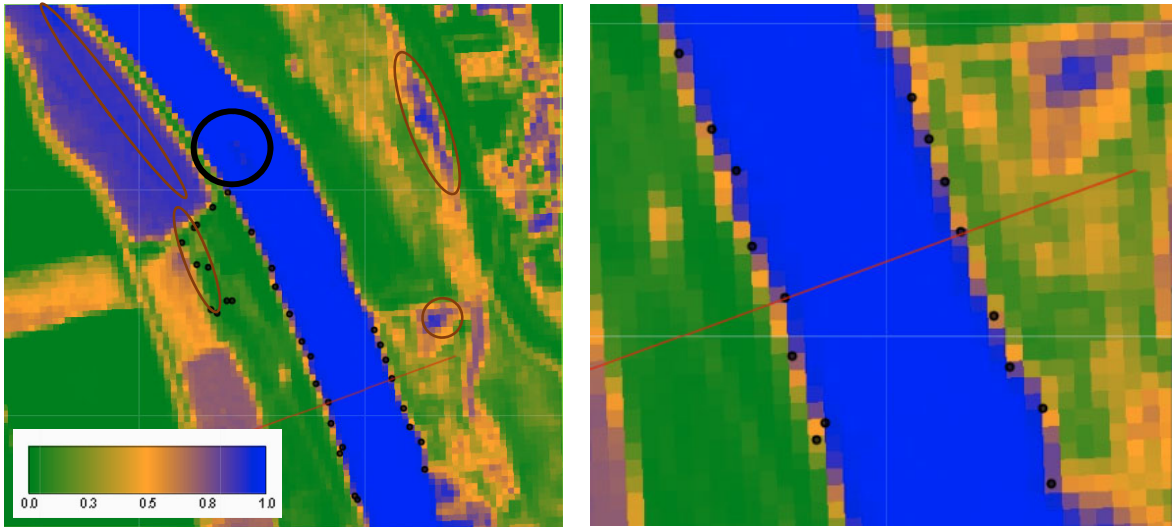


Figure 70 Probability band of the custom index: ND\_rd\_nr, Left: overview, Right: close-up \*15-02-19

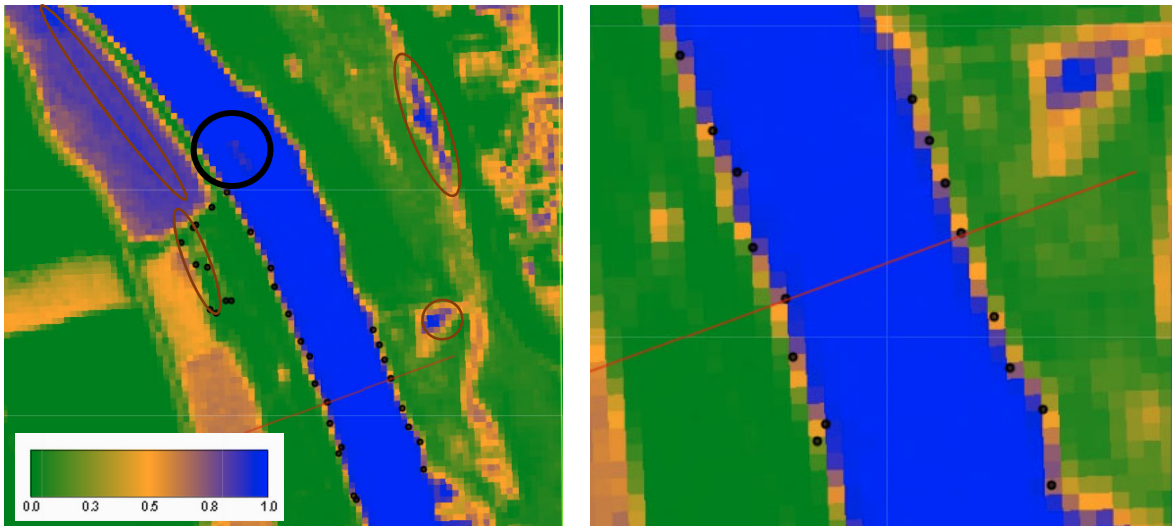
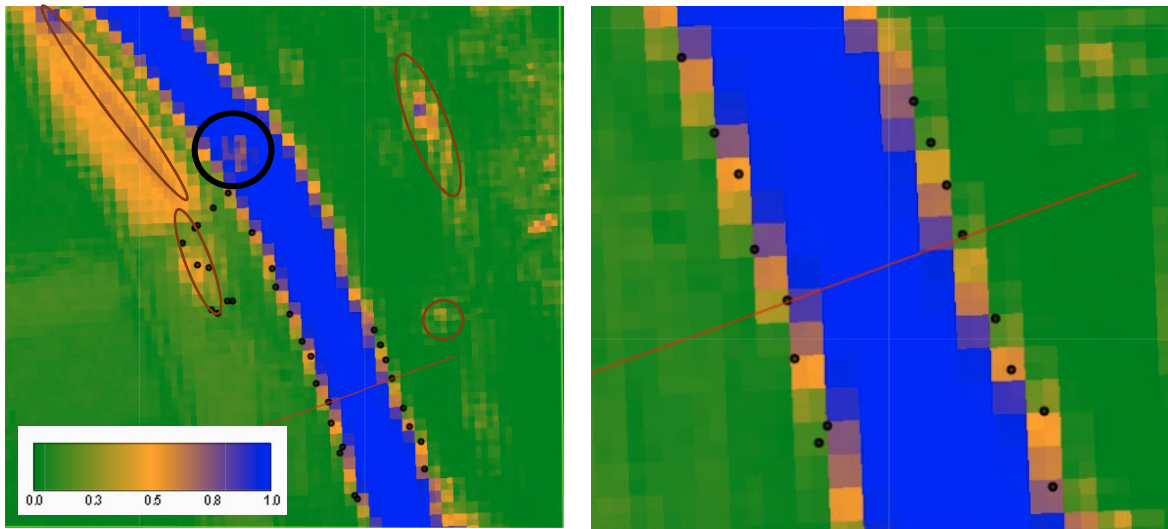
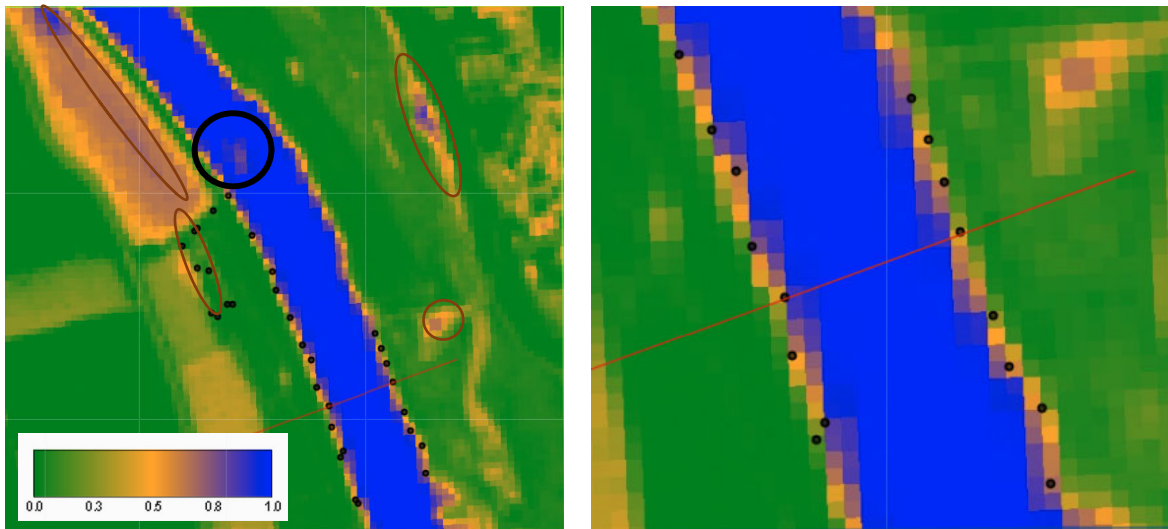


Figure 71 Probability band of the custom index: NDWI, Left: overview, Right: close-up \*15-02-19



**Figure 72** Probability band of the custom index: MNDWI, Left: overview, Right: close-up \*15-02-19



**Figure 73** Probability band of the custom index: MNDWI\_10, Left: overview, Right: close-up \*15-02-19

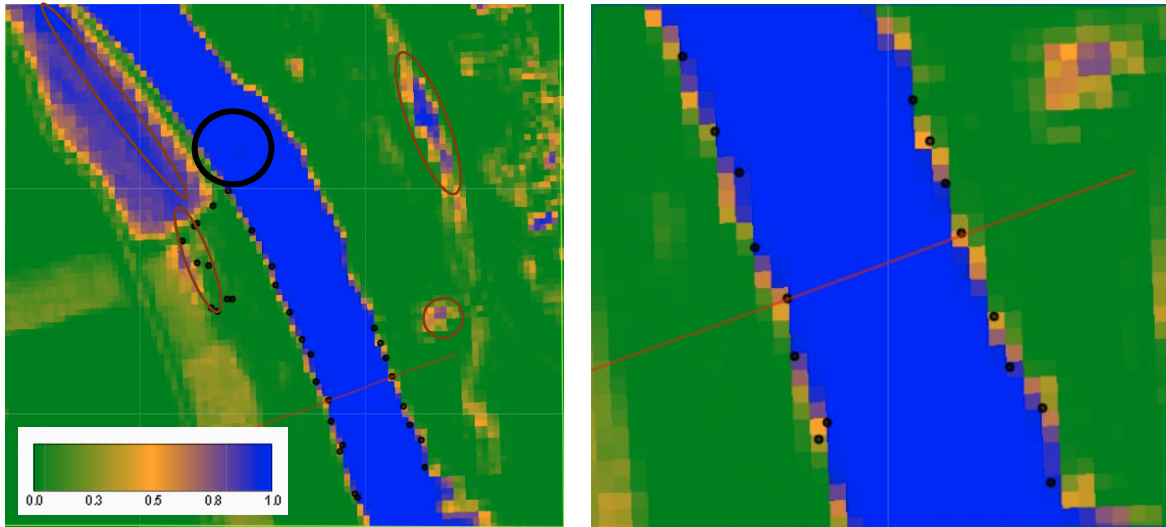


**Figure 74** Probability band of combined indices: Bayes 5-6, Left: overview, Right: close-up  
\*15-02-19

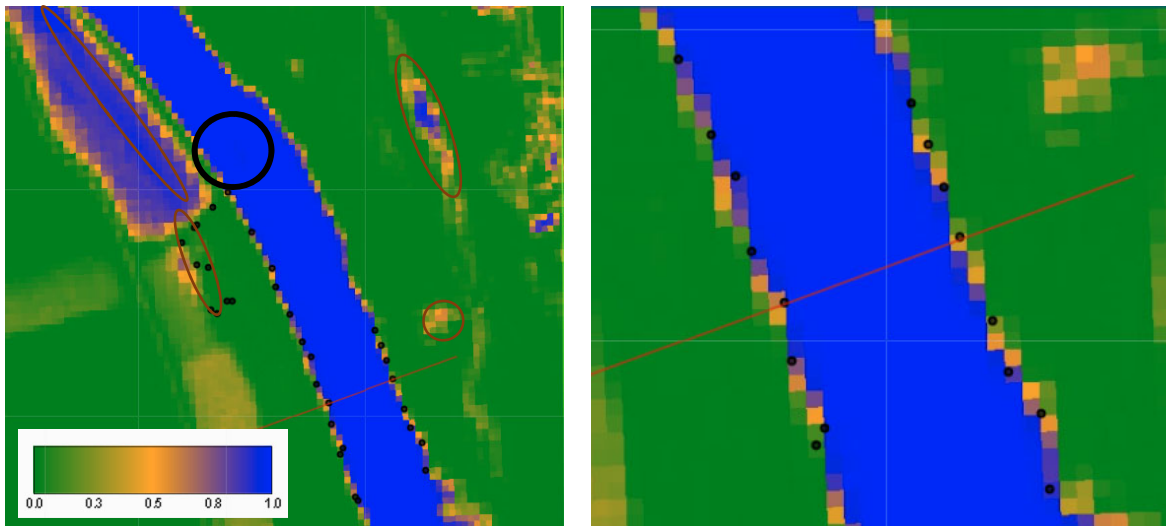


**Figure 75** Probability band of combined indices: Bayes 1-5, Left: overview, Right: close-up  
\*15-02-19

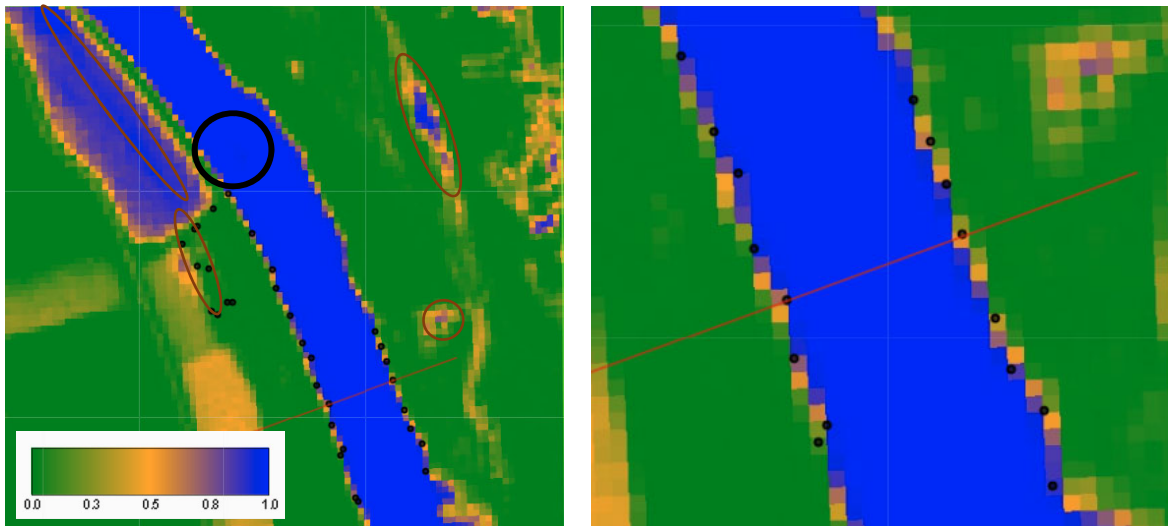


**Figure 76 Probability band of combined indices: Bayes 0-4, Left: overview, Right: close-up \*15-02-19**

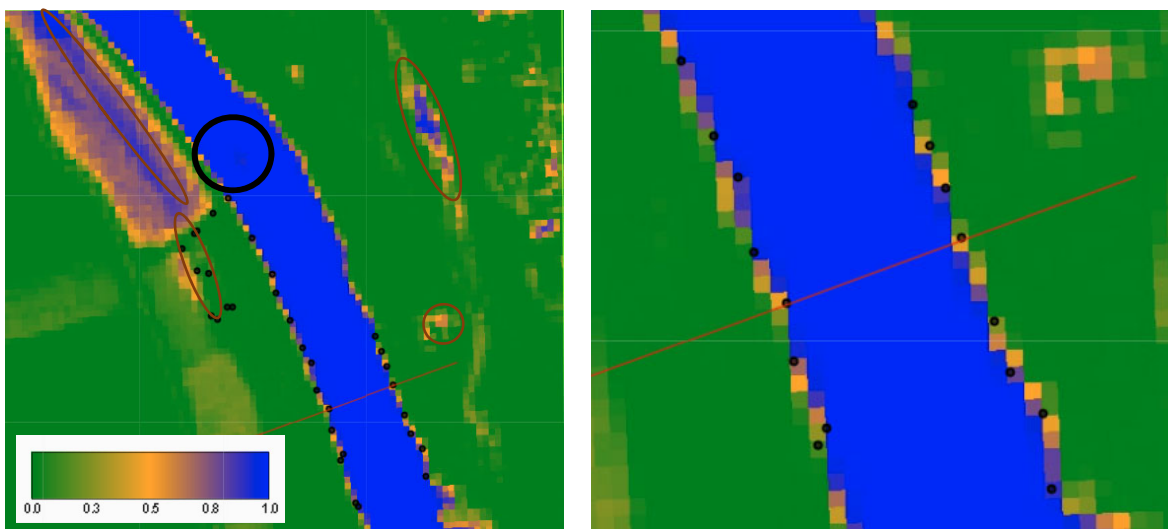


**Figure 77 Probability band of combined indices: Bayes 0-3, Left: overview, Right: close-up \*15-02-19**

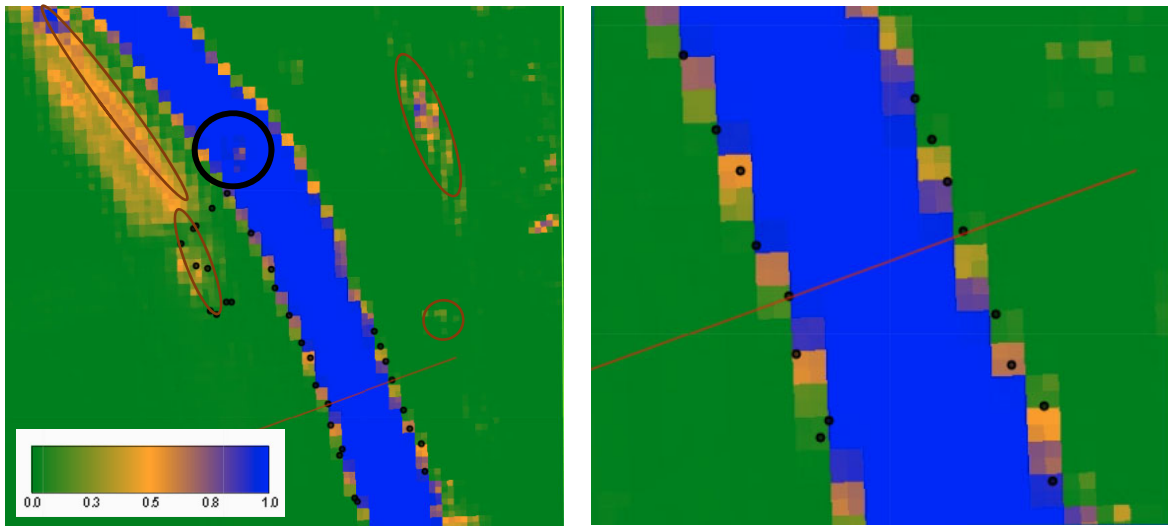


Figure 78 Probability band of combined indices: Bayes 1-3, Left: overview, Right: close-up \*15-02-19

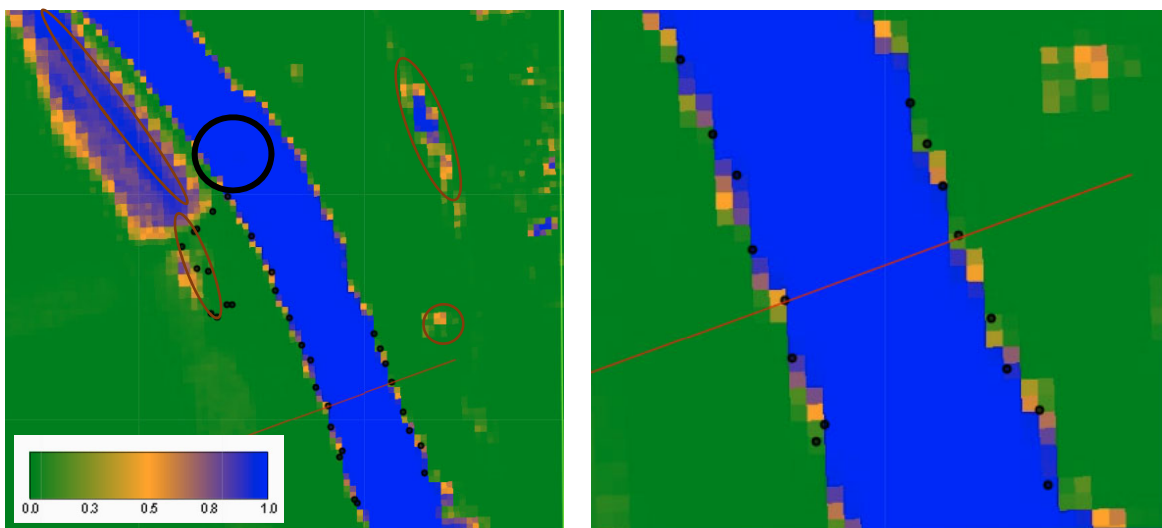


Figure 79 Probability band of combined indices: Bayes 1-5-6, Left: overview, Right: close-up \*15-02-19

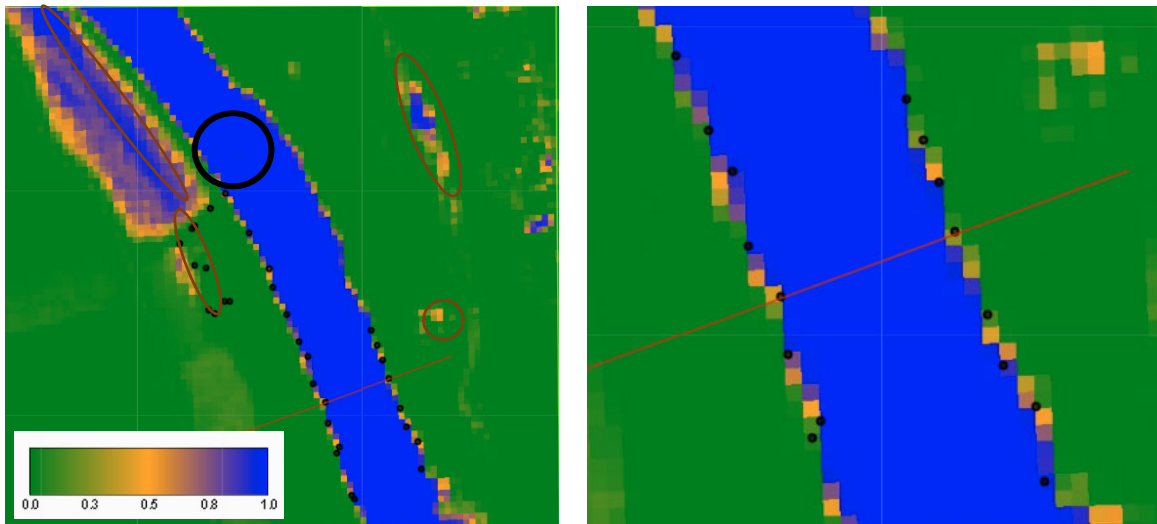


Figure 80 Probability band of combined indices: Bayes 0-3-4, Left: overview, Right: close-up  
\*15-02-19

## Water fraction relation images

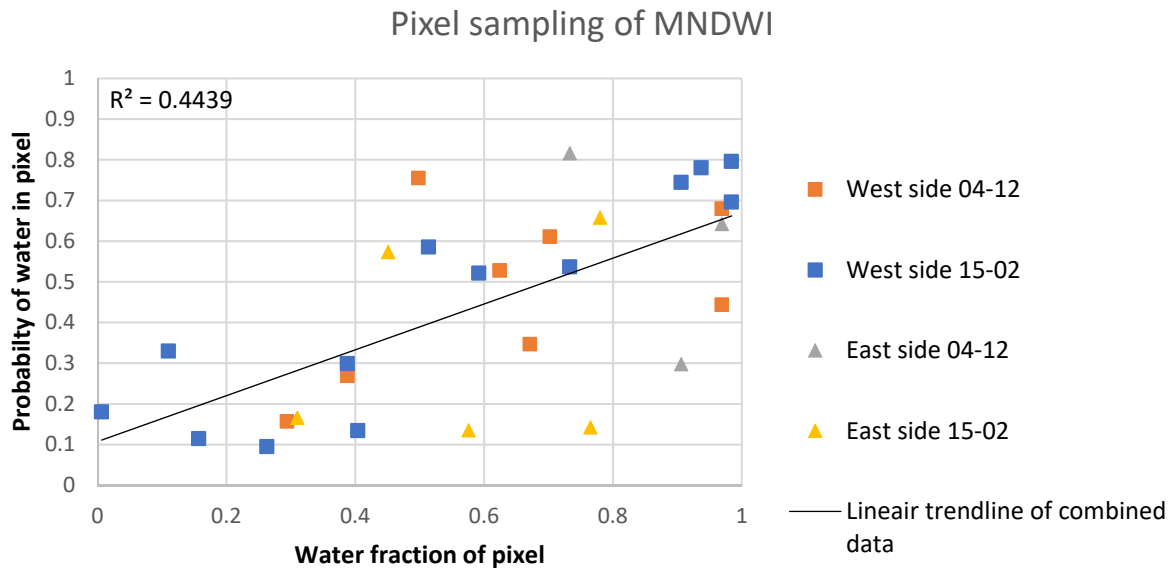


Figure 81 Pixel sampling of MNDWI

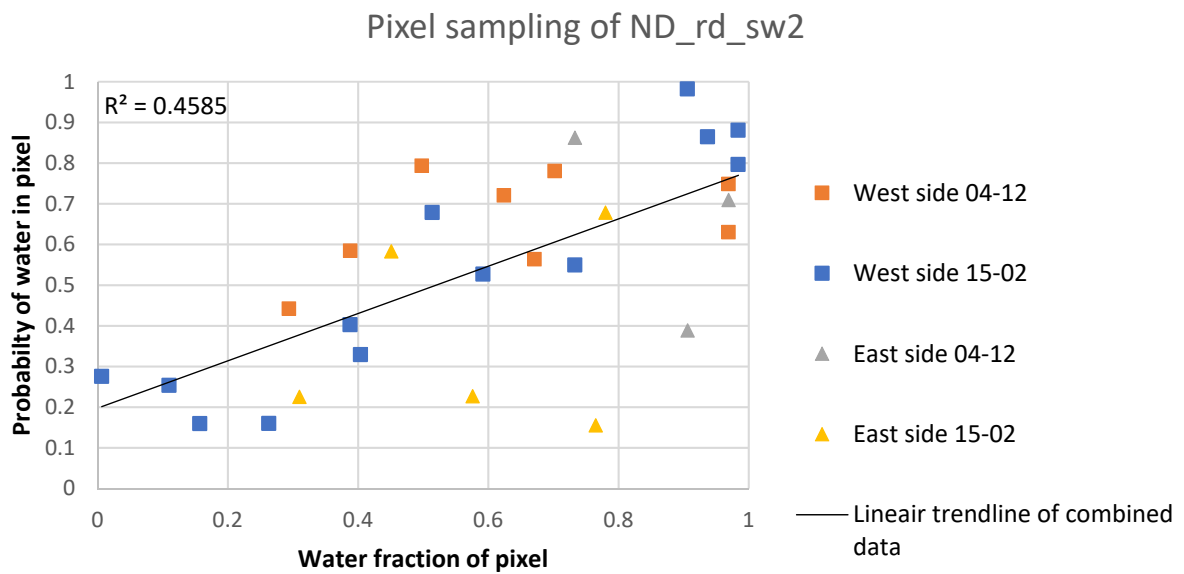


Figure 82 Pixel sampling of ND<sub>rd\_sw2</sub>, for the GNSS waterline points

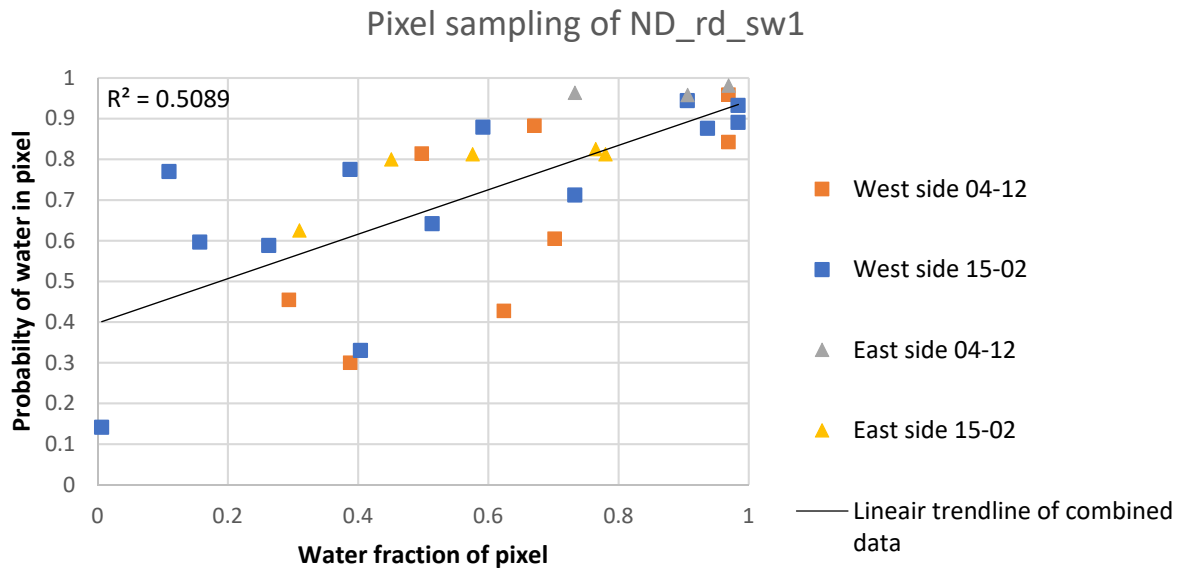


Figure 83 Pixel sampling of ND\_rd\_sw1

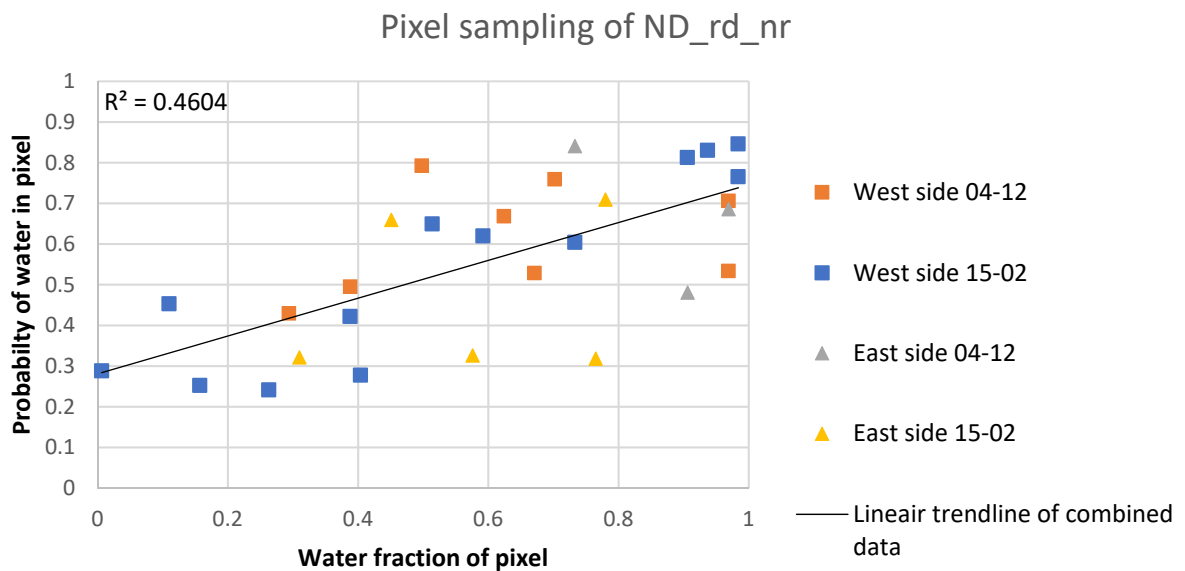


Figure 84 Pixel sampling of ND\_rd\_nr

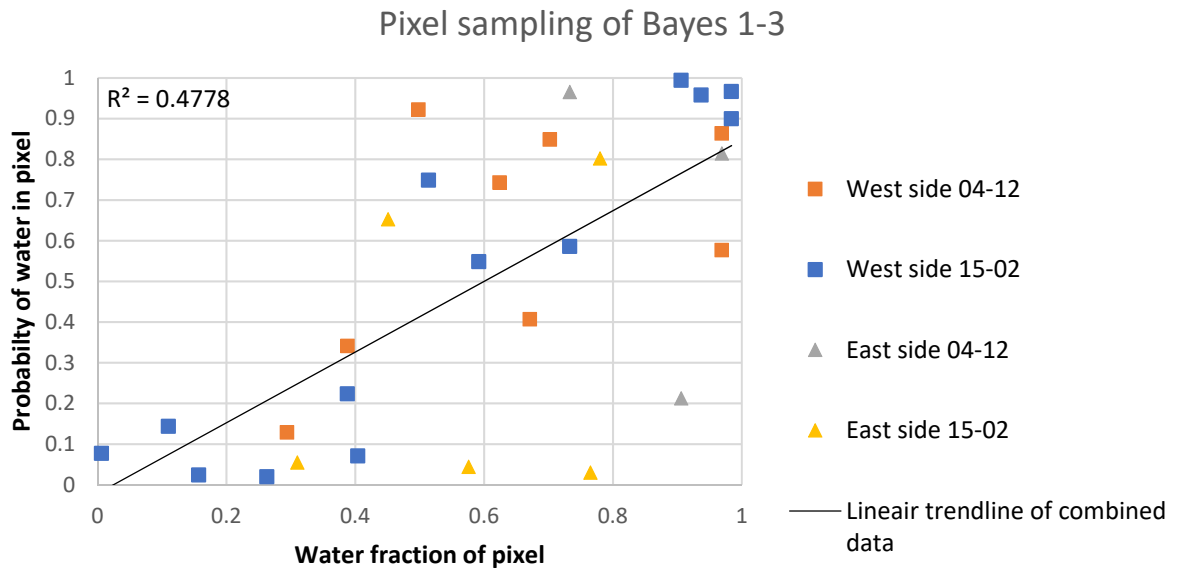


Figure 85 Pixel sampling of Bayes 1-3 combination

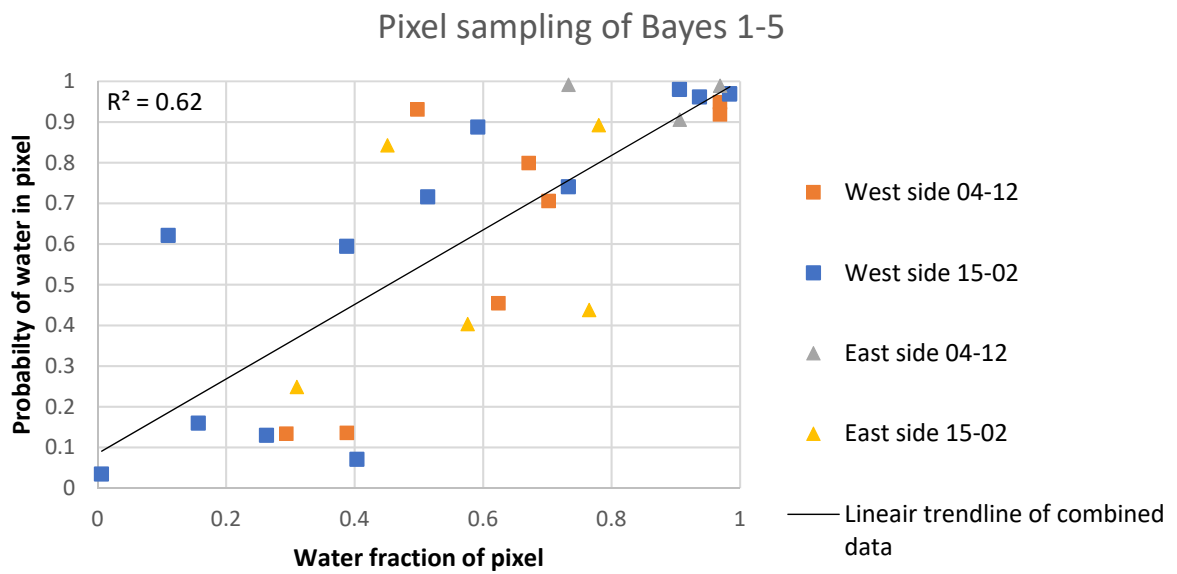


Figure 86 Pixel sampling of Bayes 1-5 combination

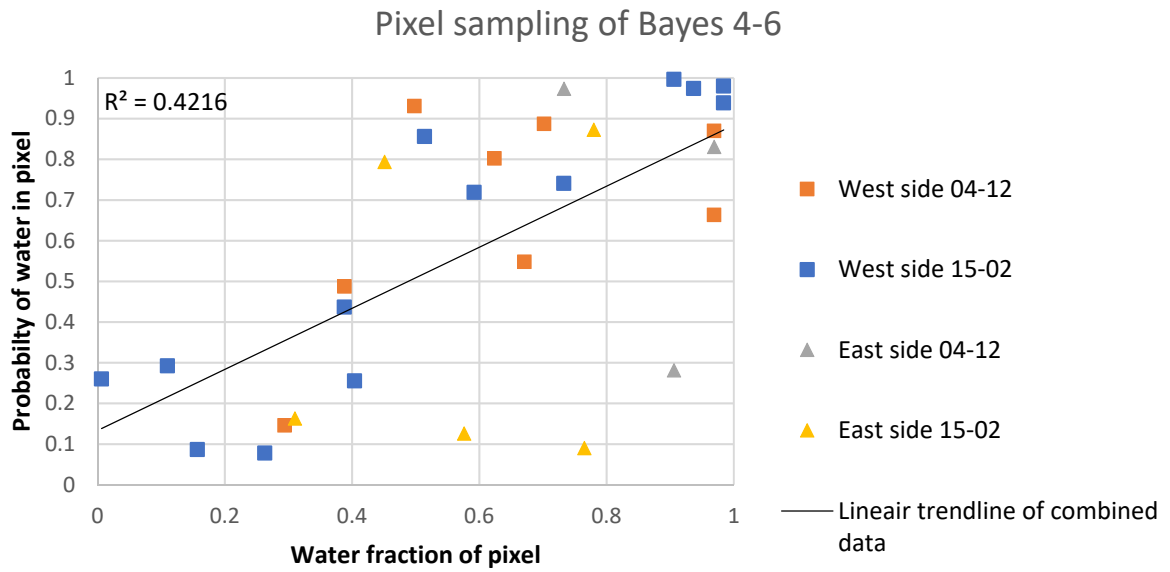


Figure 87 Pixel sampling of Bayes 4-6 combination

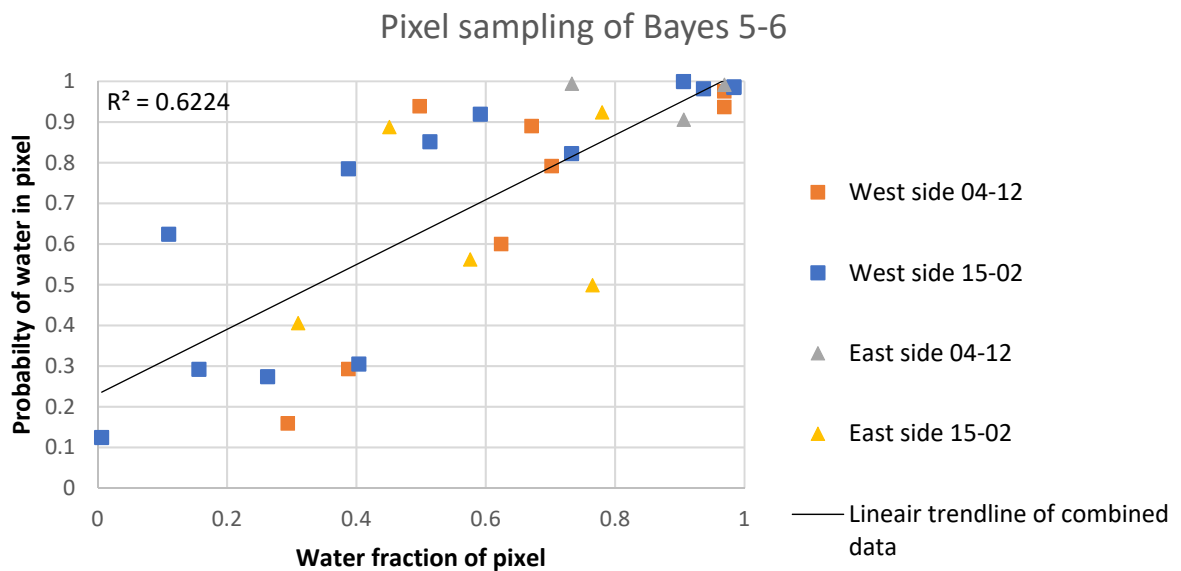


Figure 88 Pixel sampling of Bayes 5-6 combination

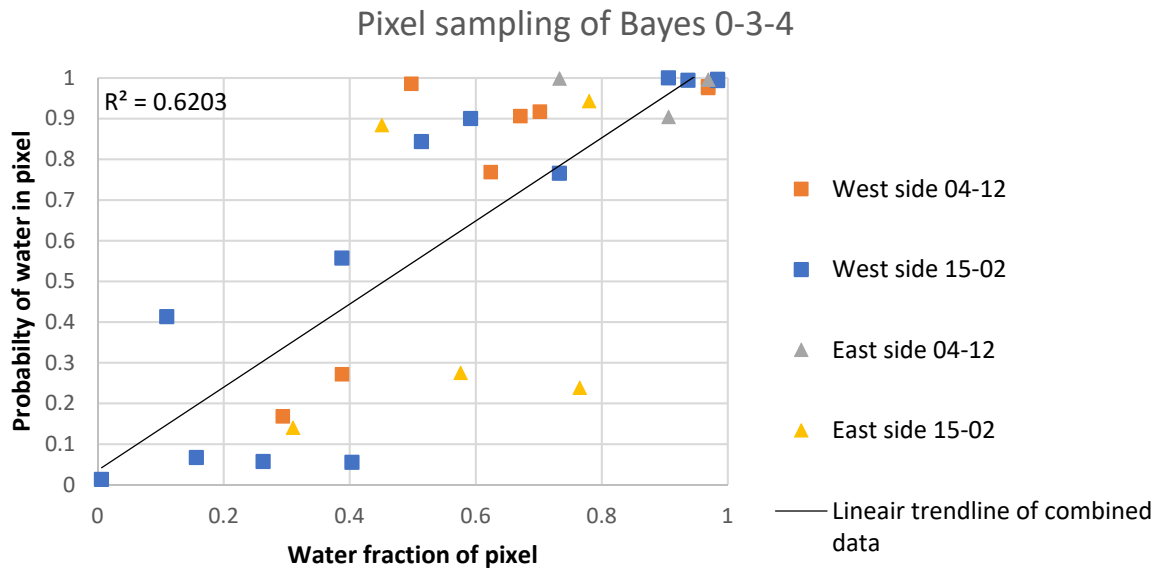


Figure 89 Pixel sampling of Bayes 0-3-4 combination

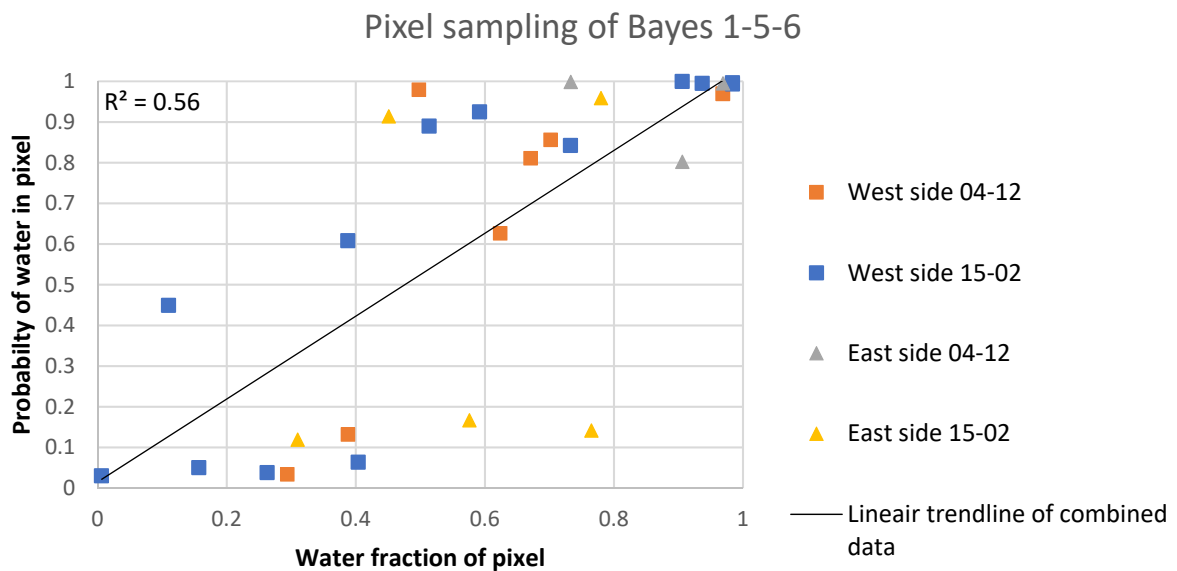
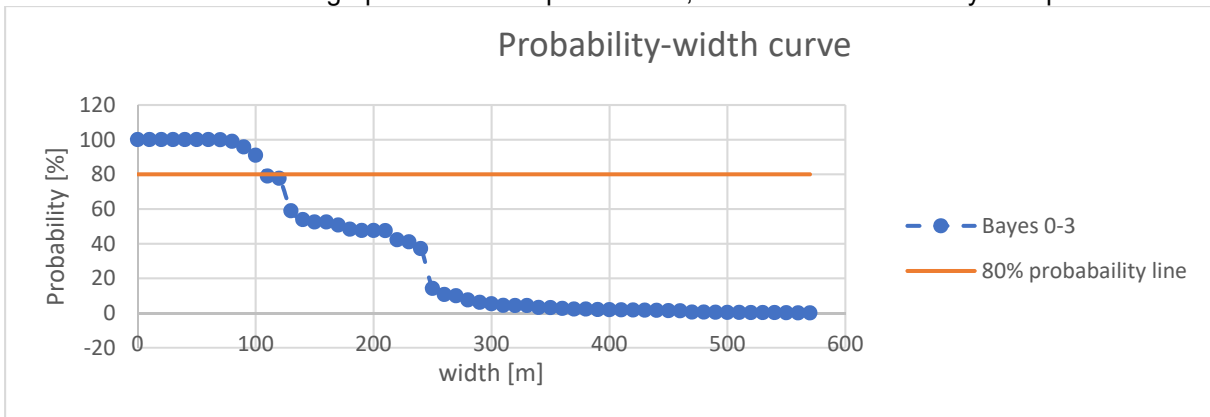


Figure 90 Pixel sampling of Bayes 1-5-6 combination

### Probability-width curve

Figure 91, below, shows how the probability against the river width looks like for the Bayes 0-3 probability band of the first fieldwork day. The orange line indicates an example threshold that can be set to the river width at 80% probability. In this case, the intersect of the two lines is located at 110 metre river-width. The dots in the graph indicate the pixel values, which are connected by a striped line.



**Figure 91 Probability vs river width for the Bayes 0-3 probability band**

## Workability of the used scripts

Below, a workflow can be found on the steps and the variable setting for the new sub-pixel based method. As mentioned in the Results and discussion section, for now, ground-truth data is needed to validate the water fraction relationships found in this thesis, for other periods in time and study locations. To construct the used ROC curves, the fieldwork on the waterline is also needed to obtain land and water polygons. Therefore, in this more in-depth workflow, fieldwork is included. In this step by step workflow, the comparisons with conventional methods are not included.

### Fieldwork:

#### 1) Fieldwork at Area Of Interest (AOI)

At the AOI, the waterline needs to be mapped during a cloud-free satellite overpass. It was shown that a GNSS device is capable of doing this. An equal amount of GNSS measurement points on both sides of the river, including the mapping of variations in a change of the river-width, by for example groins, are advised. If comparisons and relations with discharge want to be made, it is advised to also include discharge measurements with, for example, an ADCP.

### Python script connected to the Google Earth Engine server:

#### 2) Sample a 20 year of pixel data

The used python script, an altered version of the script of Genna Donchyts from Deltares, is connected with the Google Earth Engine server. The polygon coordinates of the AOI need to be inserted into the script. It is best for the AOI to contain both land and water equally to analyse results of classes with the same size. The period can be changed to a period of interest in the script to obtain historical data from. The settings are now set to filter out all pixels that have a cloud score above 0.2 and a snow score above 0.3, which can also be altered if needed. Each satellite band can be plotted as a histogram. The site-specific average land and water values need to be obtained from a few images for every band and added to the plot. This will show a visualization of the location of the classes in the band of interest. A manual filtering process can be performed to only include bands that show some discriminative behaviour between the land and water classes for the next step.

#### 3) Discriminating band combinations

In the same script of the previous step, the bands that show discriminating abilities need to be selected. Two of the selected bands at a time can then be plotted as scatterplot against each other. Kernel density functions are included that show coloured contour lines for different density pixel groups. The previous found average land and water values per band can be inserted in the same scatterplot as green and blue lines to show where the land and water class values are located in the plot. Keep in mind that bands that show a 1 to 1 relation between the bands in the scatterplot, are not suitable to be used as normalized differences indices, as is the case in Figure 38. The band combinations can be assessed and filtered on discriminating ability for further use.

### Google Earth Engine (GEE):

#### 4) Image enhancements

This research showed that pan-sharpening had a positive effect on the SWIR1 band for the normalized differences index  $MNDWI_{10}$ . If these two bands, green and SWIR1, are analysed to have discriminating behaviour at the AOI, it could be an option to perform the IHS pan-sharpening method on the SWIR1 band.

In the Google Earth Engine scripts, the band combinations of interest should be added. The 'bicubic' resampling is included in the script to be used for edge detection.

#### 5) Probability indices

For edge detection, it is needed to manually change the threshold value until a relatively smooth line is obtained as an edge around the river outline. This is needed to obtain an edge without a lot of spurious edge detections on the floodplains. There were small variations between the two days present to obtain the best setting. The threshold settings can be further analysed to make this an automated process.

The original resolution indices are then sampled over the detected edge and transformed into a Cumulative Density Function. This is included in the GEE script. The CDF of each index is used to transform the indices into probability indices.

#### 6) Combining probabilities

With the obtained discriminating probability indices, possible combinations of indices can be made. In this process, it is important to keep in mind to combine uncorrelated indices with each other. This means that indices that contain both, for example, the green band, cannot be mixed. The combination of indices is done via the Bayesian approach by updating probabilities.

#### 7) Obtaining ROC curves

For the construction of the ROC curves for the different probability indices and combined probability indices, the during fieldwork obtained land and water polygons are needed. The land and water polygons can be derived from the mapped waterline and should be included in the script for the ROC curves. The probability indices and combined indices should be added to perform the ROC analysis over. The ROC curves give the optimum thresholds for each index to be used for classification.

#### 8) Water fraction pixel analysis

The obtained waterline points by the GNSS need to be added to the 'water fraction' script. The GNSS points need to be connected by a polygon, therefore it is optimal when the GNSS points follow the change in the width of the river as correctly as possible. This script calculates the water percentage of each GNSS measurement point. For each probability index and index combination, the pixel values under the GNSS points are sampled. With the sampled index values and the water fraction of the pixels under the GNSS measurement points, a scatterplot can be made. In this scatterplot, the relation between index value and water fraction need to be analysed.

#### 9) River-width estimation

The river-width is obtained by classifying each index with the optimal threshold obtained by the ROC analysis. These thresholds need to be inserted into the 'River-width' GEE script. The indices that showed a water fraction relationship in the previous step can be used for sub-pixel analysis. The river-width GEE script measures the river-width over a drawn line, crossing the river, which measures per 0.5 metres for computational limitations in GEE. The adjacent pixels next to the waterbody need to be sampled and converted into an additional width by the obtained water fraction relationship.